Appendix A
3D Modeling to Assess the As-Built Mixing Zone and to Compare Residence Times on the Southern Shelf under As-Built vs. Extended Outfall Scenarios

A.1 Introduction

Professor Edwin (Todd) Cowen and Dr. Alexandra (Allie) King of the DeFrees Hydraulics Laboratory, Cornell University College of Engineering, completed numerical simulations of the water motion (hydrodynamics) of Cayuga Lake using the three-dimensional (3D) free surface hydrodynamic model Si3D (Rueda 2001; Smith 2006; Rueda and Cowen 2005; Rueda et al. 2008; Acosta et al. 2015). While the long, narrow, deep geometry of Cayuga Lake ensures that lake-wide processes are largely two-dimensional, and thus a 2D model is appropriate for lake-wide phenomena, the southern shelf is no longer than its width, resulting in high lateral gradients and three-dimensional flow and transport processes. Hence 3D modeling is required to capture and quantify the spatial-temporal evolution of the Lake Source Cooling (LSC) outfall plume, its hydrodynamic impact on the southern shelf, and in particular its impact on shelf residence times in response to various physical forcing scenarios. Model runs were selected to examine the thermal plume under various conditions of LSC facility performance, wind conditions, and tributary inflows. The model output enabled the research team to estimate the water residence time on the lake's southern shelf.

The 3D hydrodynamic model was set up, calibrated, and validated using site-specific data. These data include the detailed bathymetric surveys completed for the construction of the LSC intake and outfall pipes, the long-term water temperature record collected at the piling cluster, the long-term temperature record at the LSC intake, data from the point sources discharging to southern Cayuga Lake, and additional field observations including a gridding study conducted specifically for the purposes of model validation. The following sections describe the field measurements, model development and enhancements, model calibration, model validation, and results of simulations.

A.2 Field Measurements

Site-specific field data were used to specify the boundary conditions and initial conditions of the 3D model, and also for calibration and validation. In this section we document collection and analysis of this field data.

A.2.1 Bathymetry

Bathymetric measurements, used to develop the numerical grid for the 3D model, as described in Section **A.4.3.1**, were obtained from the following sources:

1. Cayuga and Seneca Lakes NOAA Canal System chart 14791 (paper, pre-1974)
2. Lake Source Cooling as-built survey (1996)
3. NYS Canal Corporation soundings (2006 & 2008)
4. Cornell soundings on shelf (Vandebroek, 2011)
5. Cornell shoreline survey (Vandebroek, 2011)
6. 2014 gridding study (described in present report, Section **A.2.8**)

The GPS coordinates of data from these sources are shown in Figure A-1.

Tributaries are included in the numerical grid up to the location of the first hydraulic jump upstream of the lake, identified in a field survey conducted by the Cayuga Lake Modeling Program (CLMP) team on June 10-11, 2012. Above this first hydraulic jump, flow is supercritical, meaning surface waves cannot propagate upstream. The coordinates of this location for each tributary are documented in Table A-1.

Table A-1. Locations of first hydraulic jump upstream of Cayuga Lake along each of the southern tributaries, marking the upper limit of where the tributary may be influenced by the lake surface seiche. Coordinates are NAD83, UTM Zone 18.

Tributary	x (m)	y (m)	Date	Notes
Fall Creek	0376765	4701268	June 11, 2012	In the woods along path that leads up to Ithaca Falls, past Route 13
Sixmile Creek	0376163	4699054	June 11, 2012	Near intersection of Fair St. and South St.
Cayuga Inlet Creek	0374798	4698340	June 10, 2012	At waterfall just beyond railroad crossing
Cascadilla Creek	0376487	4700600	June 10, 2012	Near intersection of Willow Ave. and Hancock St.

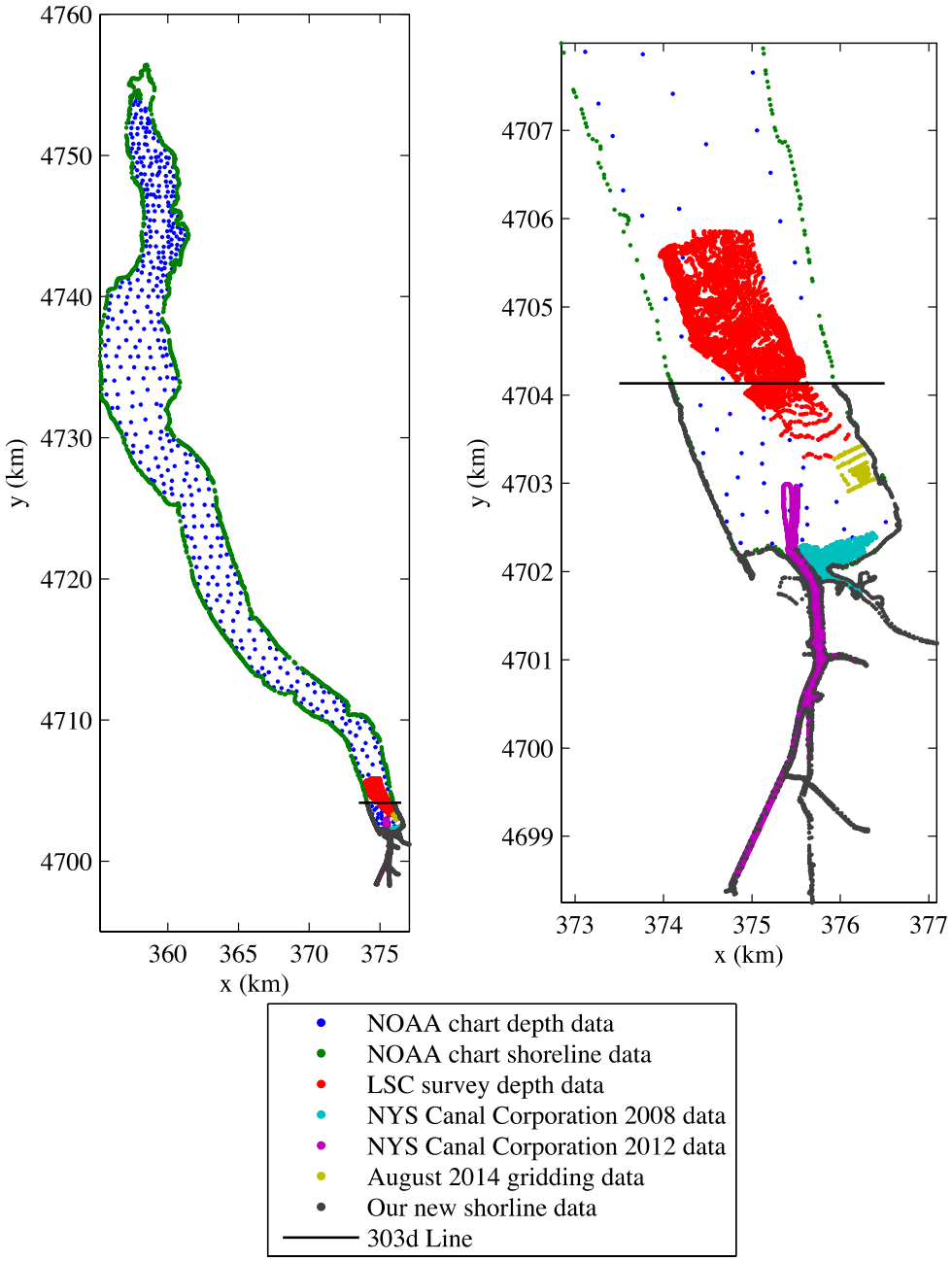

Figure A-1. Coordinates (NAD83, UTM Zone 18T) where depth and shoreline measurements are available.

A.2.2 Temperature Records

Thermistor chains were deployed by Cornell University for research purposes between 1998 and 2014. From year-to-year, deployment times and locations varied; thermistor chains were typically deployed in summer and fall in deep water with thermistors spaced several meters apart to resolve the thermocline, recording measurements every 1-2 minutes. In 2012, 2013, and 2014, thermistor chains were deployed

near the LSC intake in ~80m of water. The location of the LSC intake is shown in Figure A-2.

Continuous water temperature records are also available from single thermistors at the piling cluster and from the LSC intake water. The location of the piling cluster is also shown in Figure A-2. Intake water temperature is measured at the LSC Heat Exchange facility (HXF). Piling cluster measurements date back to 1998, and hourly intake temperature measurements began at the HXF in 2005.

In 2014, additional 15-min frequency temperature measurements are available from the PISCES, an autonomous sampler operated by Ithaca Area Wastewater Treatment Plant (IAWWTP) staff and located in the Cayuga Inlet at a depth of 1.5m. The location of the PISCES is also shown in Figure A-2.

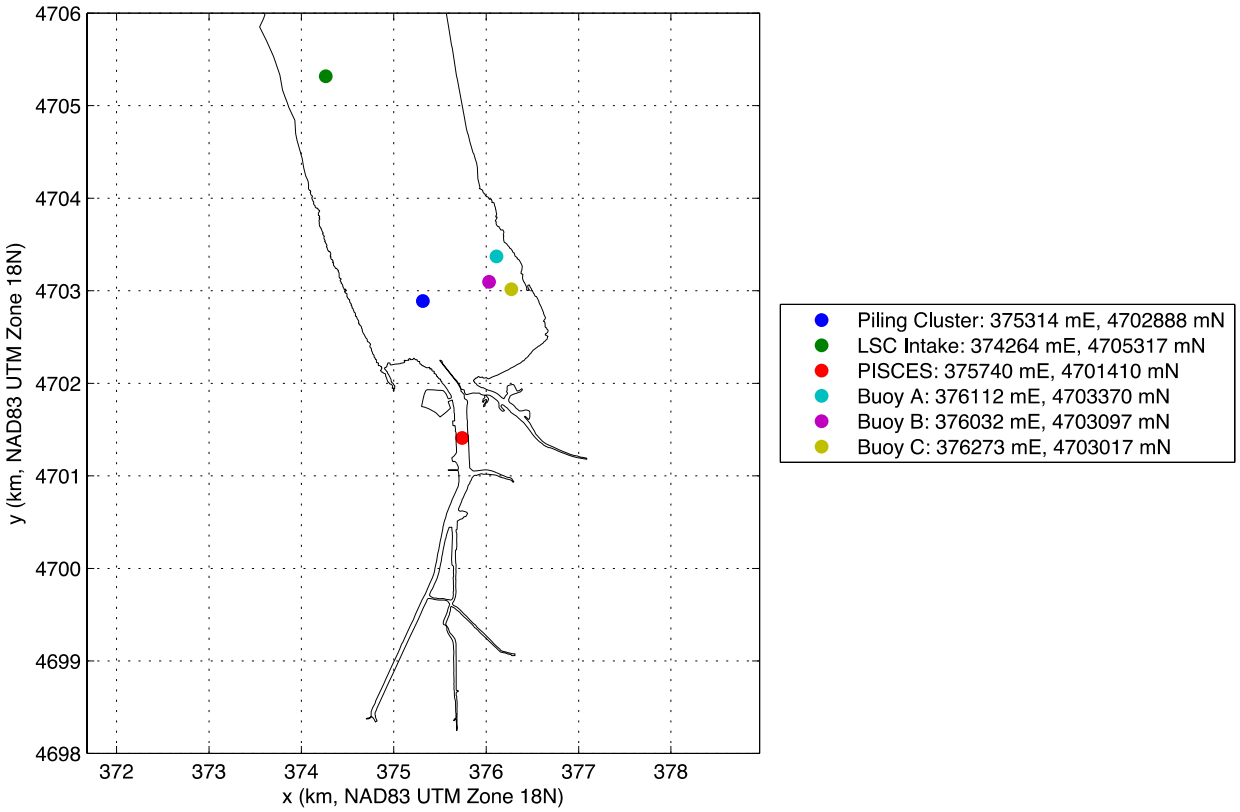

Figure A-2. Instrument locations.

Thermistors on a chain are subject to vertical motions when wind pulls the buoy at the top across the water surface. For the intake thermistor chain, we made corrections to depth using data from a pressure sensor at the top of the chain (see Schweitzer 2015 for details).

Thermocline depth at the location of the intake thermistor chain was computed using a temperature-gradient weighted depth average as follows:

$$z_T = \frac{\int_{-H}^{0} z \frac{dT}{dz} dz}{\int_{-H}^{0} \frac{dT}{dz} dz} \quad (1)$$

Here T is temperature, z is elevation ($z = 0$ at the water surface), and z_T is the thermocline elevation. We found this definition to be more robust than the more typical definition, which is the location of maximum temperature gradient. The more typical definition can erroneously identify diurnal near-surface temperature gradients as the seasonal thermocline.

Additional temperature measurements were collected near the LSC outfall during a detailed gridding study in 2014. These are described in Section **A.3.1**.

A.2.3 Meteorological Measurements

Meteorological measurements (wind velocity, air temperature, shortwave radiation, relative humidity, and air pressure) were made every 10 minutes at the piling cluster from October 2011 through 2014. Prior to October 2011, meteorological measurements are available from a land-based station operated by Cornell at Game Farm Road and from another station at the Ithaca Airport. Wind measurements differ somewhat between the piling cluster and Game Farm Road stations. Gelda et al. (2015) found that using on-lake meteorological measurements (from the piling cluster) to drive their two-dimensional Cayuga Lake simulations for 2012 and 2013 produced significantly better results than using Game Farm Road meteorological measurements. They developed a least square linear transform method to predict wind velocities at the piling cluster based on wind velocity measurements at the Game Farm Road station and found the transformed Game Farm Road wind velocities produced better model results than the untransformed velocities. Consequently, we use piling cluster meteorological measurements when available and transformed land-based measurements for periods prior to October 2011 and where piling cluster measurements are not available during short periods.

A.2.4 Extinction Coefficient

Light extinction coefficient ($\mathrm{K_d}$) was measured by Upstate Freshwater Institute (UFI) every two weeks from 1998-2006 and in 2013 at CLMP Site 3, and we use these measurements, which are representative of the lake basin, to compute surface boundary conditions for the 3D model in 2013. In 2012 and 2014, we do not have measurements of $\mathrm{K_d}$, but we do have Secchi depth (SD) measurements. SD was measured as part of the LSC monitoring program from 2007-2012, and those measurements are available at CLMP Site 3 (equivalent to LSC Site 8). 2014 SD measurements were made available by Bill Foster from the Cayuga Lake Floating Classroom. These measurements were collected several times per week throughout the summer along transects within the main body of the lake – from Bolton Point to Ithaca Yacht club, and from Myers Point to Taughannock Point. The measurements were collected by students and confirmed by Floating Classroom staff.

Where SD measurements are available but not $\mathrm{K_d}$, we use the following relationship to compute $\mathrm{K_d}$:

$$K_d = 0.84\ (SD)^{-1} + (0.16)\mathrm{m}^{-1} \quad (2)$$

This linear relationship is based on a regression by UFI for their biweekly CLMP Site 3 data (1998–2006 plus 2013). The relationship between $\mathrm{K_d}$ and $(\mathrm{SD})^{-1}$ is not particularly strong (R^2 = 0.57), which UFI notes is "supported by general optical theory and UFI's analysis of Cayuga Lake's in-situ optical properties", in that the ratio of absorption to scattering varies over time and between sampling sites within Cayuga Lake, $\mathrm{K_d}$ is influenced more by absorption than by scattering, and Secchi depth is influenced more by scattering than by absorption (personal communication with Susan O'Donnell).

A.2.5 Lake Water Level

Lake water level is measured by the USGS in Cayuga Inlet (Station 04233500) every 15 minutes. These data are used to define model boundary conditions, and reference thermistor depths to a fixed datum.

A.2.6 Tributary Flow Rates and Temperatures

Fall Creek, Sixmile Creek, Cayuga Inlet Creek, and Cascadilla Creek deliver nearly 40% of the inflow to Cayuga Lake and 100% of the tributary inflow to the southern shelf. The three largest of these tributaries are also the most monitored. Hence we include only these four tributaries as inputs to the 3D model. Tributary flow rates are measured every 15 minutes by the USGS at Fall Creek, Six Mile Creek, and Cayuga Inlet. Gage station numbers and watershed areas are summarized in Table A-2. Total watershed areas are from Haith et al. (2012). The area weighting method is used to convert measured flow rate to flow rate entering Cayuga Lake. For example, for Sixmile Creek:

(Sixmile Creek Inflow) = 134.11/101.010 x (Flow Measured by USGS at Sixmile Station)

Flow rate in Cascadilla Creek, which is not gaged, is estimated from Six Mile Creek flow rate measurements using the area weighting method, i.e.

(Cascadilla Creek Inflow) = 36.65/134.11 x (Sixmile Creek Inflow)

Boundary conditions for stream inputs include flow rate and stream temperature; some stream temperature measurements are available, and stream temperature is set to a 10-day moving average of air temperature where other measurements are not available. We found this to be a reasonable predictor of stream temperature.

Table A-2. Gage station numbers and watershed areas for southern shelf tributaries.

Tributary	USGS Gage Number	Watershed Area Above Gage km^2	Total Watershed Area, km^2	% Watershed Above Gage
Fall Cr.	04234000	326.339	330.86	98.6%
Sixmile Cr.	04233300	101.010	134.11	75.3%
Cayuga Inlet	04233255	224.552	240.81	93.2%
Cascadilla Cr.	N.A.	N.A.	36.65	N.A.

A.2.7 Point Sources

Three point sources discharge onto the southern shelf: the wastewater treatment plants operated by the City of Ithaca and the Village of Cayuga Heights (IAWWTP and CHWWTP, respectively), and the Lake Source Cooling outfall. The GPS coordinates of these point sources are given in Table A-3. The theoretical location of an extended LSC outfall is also included in this table.

Table A-3. Coordinates of the point sources discharging onto the southern shelf. Coordinates are NAD83 UTM Zone 18.

	x (m)	y (m)
IAWWTP	375622	4702469
CHWWTP	376340	4702920
LSC (as built)	376256	4703137
LSC (extended)	375046	4704333

Geometry of the as-built LSC diffuser is described in detail in Section **A.3.1**.

The IAWWTP diffuser characteristics were determined from as-built documents archived at the plant. The outfall pipe is buried underground and runs into the lake from the south at an angle 30.6^{o} west of north. The final 240ft of the pipe has 25 6in-ID diffuser ports spaced 10ft apart, although the final 5 ports are closed, so effectively the diffuser is 190ft long with 20 6in ID ports. The ports discharge very close to the bed, perpendicularly to the pipe, and horizontally, alternating direction of discharge along the pipe. Assuming an area ratio of 0.61 for the vena contracta, the total port area is 0.2225m^{2}. Coordinates in Table A-1 refer to the northernmost tip of the diffuser.

We do not know all the details of the CHWWTP diffuser geometry, but Brent Cross, the plant operator, sent the following information via email: 18-in diameter PE pipe, 1500 linear ft. running WNW from the east shore, with 22 holes (3.5 inches) located over the last 150 ft. of the pipe, the end may be capped. We do not know what direction the holes point, but since the CHWWTP discharge is small, it should not significantly affect flow on the shelf. It was assumed for the modeling exercise that the holes are oriented upward. The location of the CHWWTP diffuser was determined approximately by visual inspection, as the coordinates given in the SPDES reports are imprecise.

Temperature and flow rate of the LSC effluent has been measured hourly at the LSC Heat Exchange Facility since 2005. Daily average flow rate and temperature records are available from the Ithaca Area Wastewater Treatment Plant (IAWWTP) from 1995 to present. Monthly average flow rates and temperatures are publically available in the SPDES reports from the CHWWTP.

A.2.8 Summer 2014 Gridding Study

A detailed survey of temperatures in the vicinity of the LSC outfall was conducted August 15-16, 2014 to provide a calibration data set for the 3D model. On August 5, 2014, a thermistor chain was deployed near the LSC intake and the thermistors were programmed to record water temperature every 2 minutes. The piling cluster meteorological station and thermistor were already deployed and remained in service for the remainder of 2014. Additionally, on the morning of August 15, thermistors were deployed on moored buoys (labeled Buoy A, Buoy B, and Buoy C), 0.5m below the surface, at locations south, north, and west of the LSC outfall, as shown in Figure A-3. These thermistors recorded through August 19. On August 15 and 16, detailed temperature profiles were collected using a Seabird CTD profiler and a SCAMP microstructure profiler. The Seabird profiler samples at 4Hz and was lowered manually from the water surface to the bed at a rate of approximately 20cm/s. The SCAMP is weighted to sink at approximately 10cm/s and samples at 100Hz, recording from the water surface to the bed. The result was a detailed temperature profile over all z at each (x,y) coordinate shown in Figure A-3 and Figure A-4. The temperature profiles were averaged and interpolated onto the 3D model grid for comparison. The temperature profiles are shown in Figure A-5 and Figure A-6. Temperatures from the moored thermistors are plotted in Figure A-7.

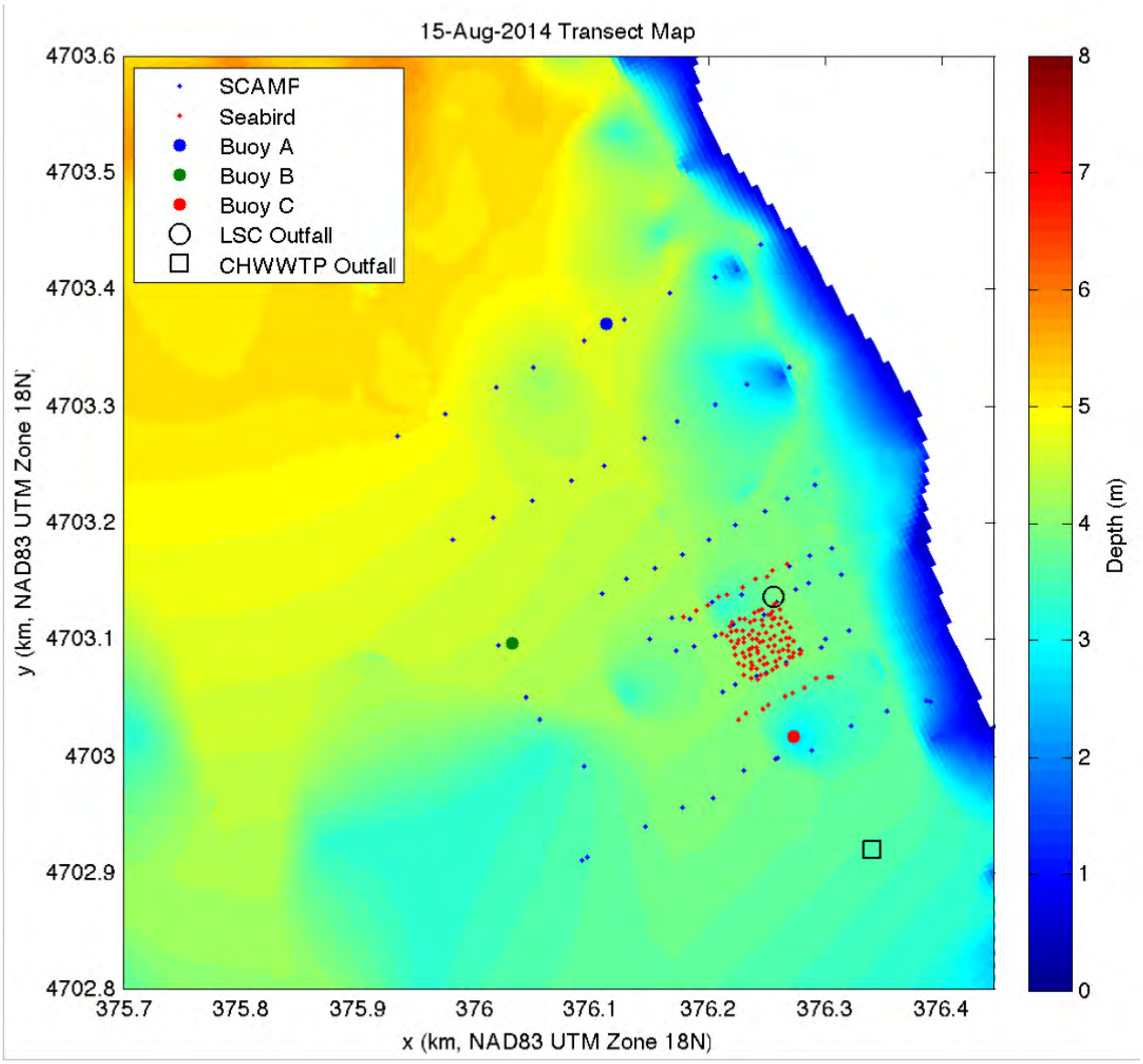

Figure A-3. Locations of the SCAMP and Seabird transects on August 15, during the 2014 gridding study. Also shown are the locations of the LSC and CHWWTP outfalls, and the locations of the moored thermisters.

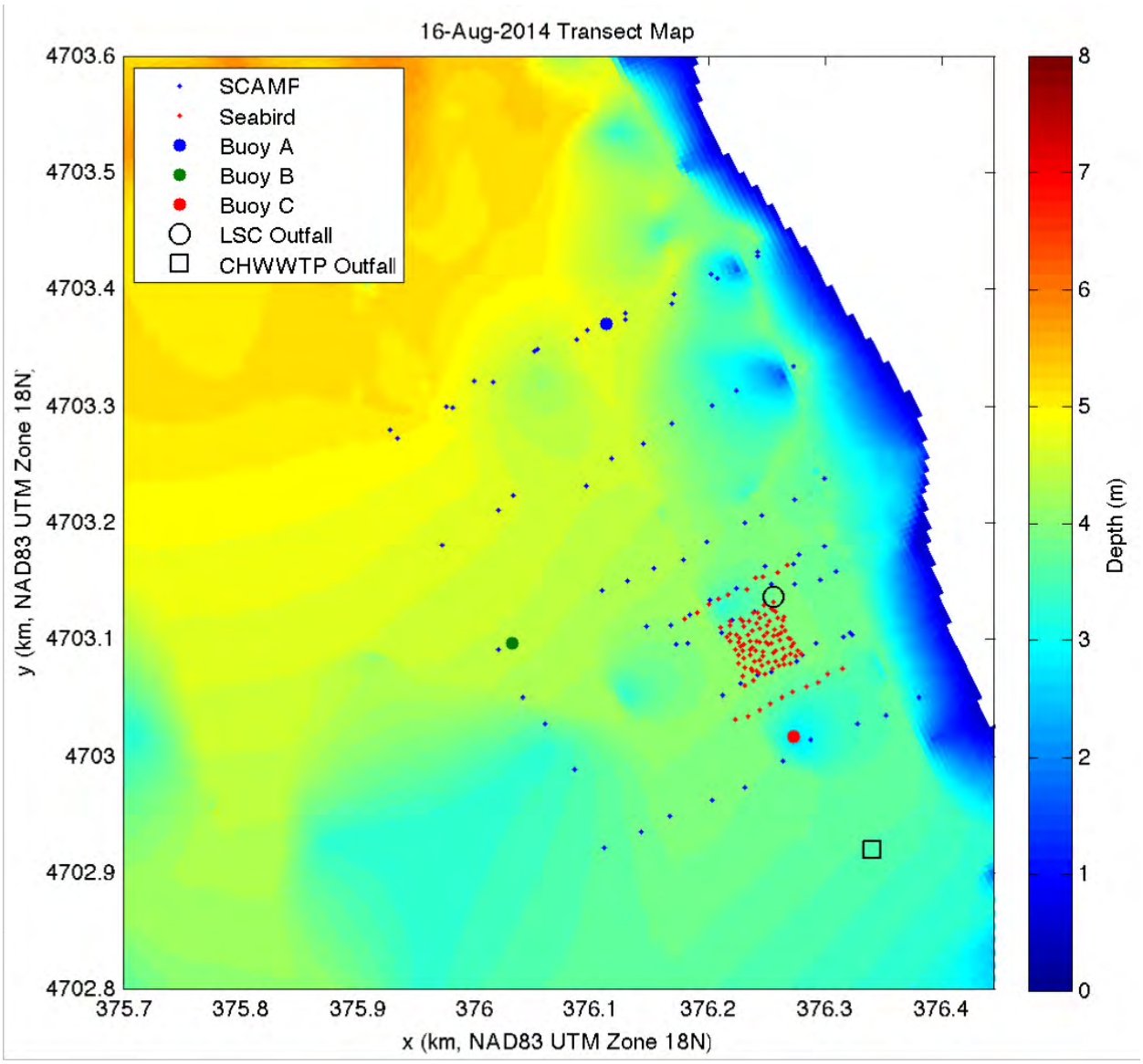

Figure A-4. Locations of the SCAMP and Seabird transects on August 16, during the 2014 gridding study. Also shown are the locations of the LSC and CHWWTP outfalls, and the locations of the moored thermisters.

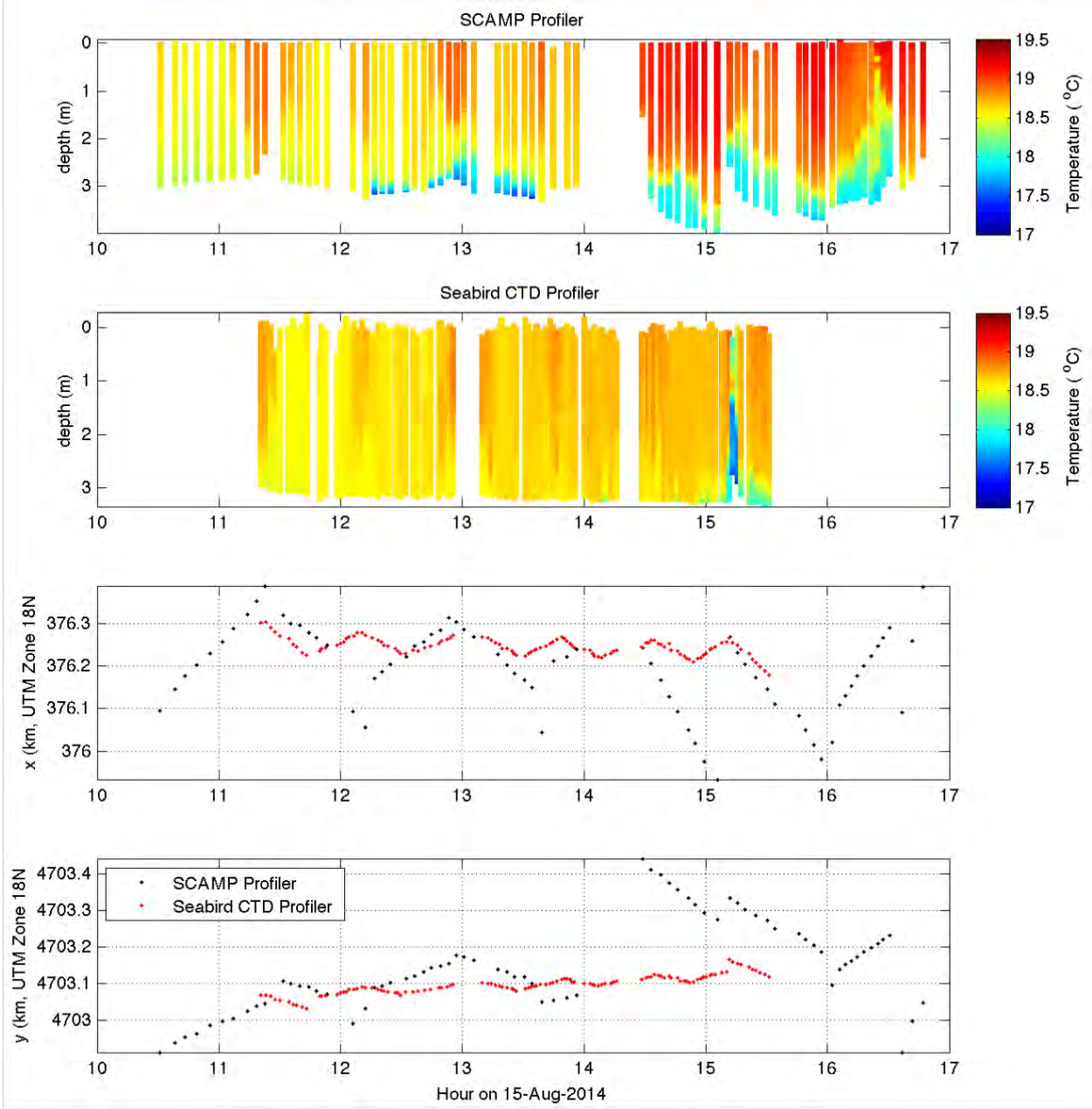

Figure A-5. Temperature profiles measured by the SCAMP and Seabird during the August 15, 2014 gridding study are plotted in the top two panels. The coordinates of each profile are shown in the lower two panels – each set of (x,y) coordinates corresponds to the temperature profile directly above. These coordinates are shown in Figure A-3.

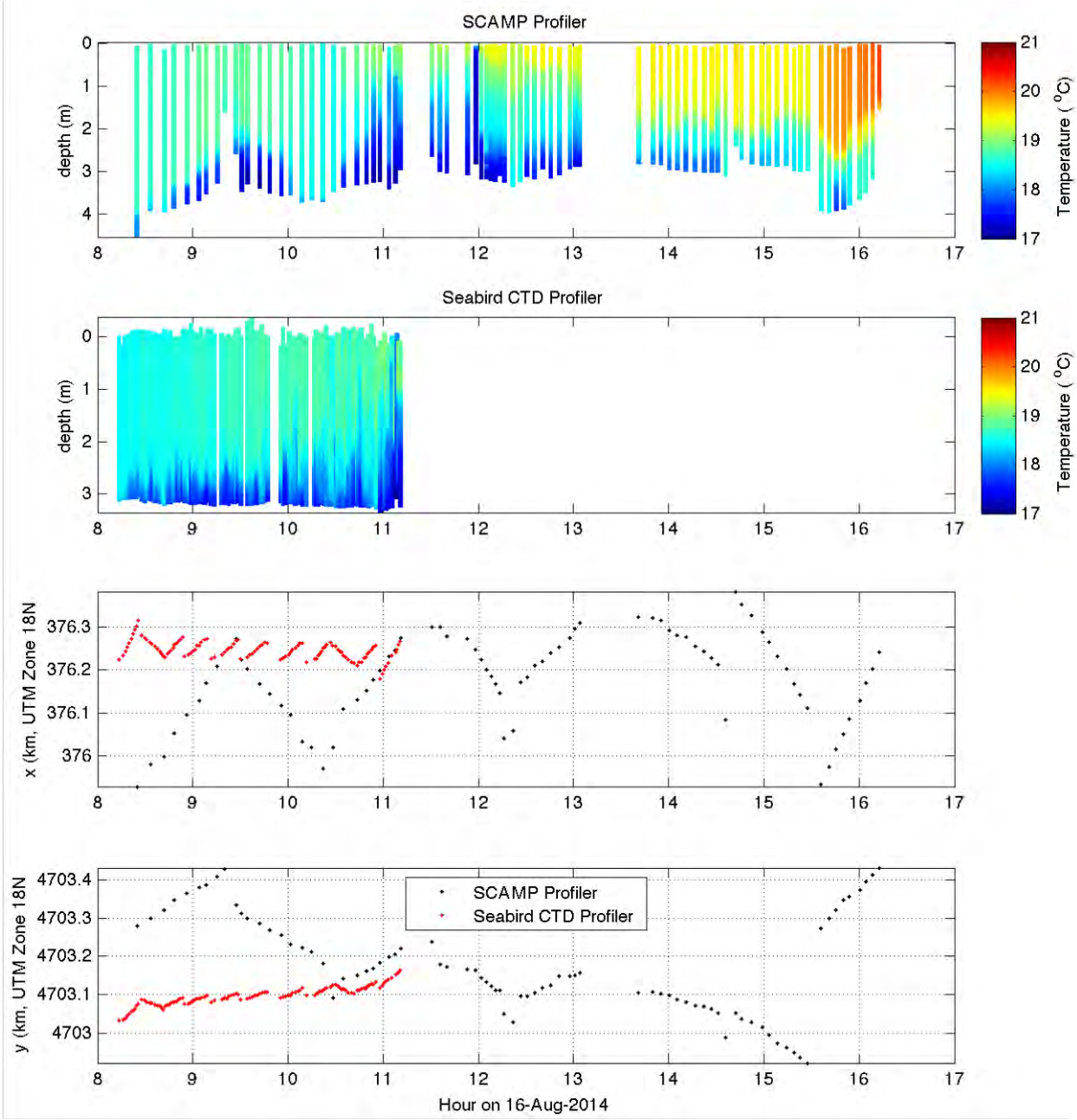

Figure A-6. Temperature profiles measured by the SCAMP and Seabird during the August 16, 2014 gridding study are plotted in the top two panels. The coordinates of each profile are shown in the lower two panels – each set of (x,y) coordinates corresponds to the temperature profile directly above. These coordinates are shown in Figure A-4.

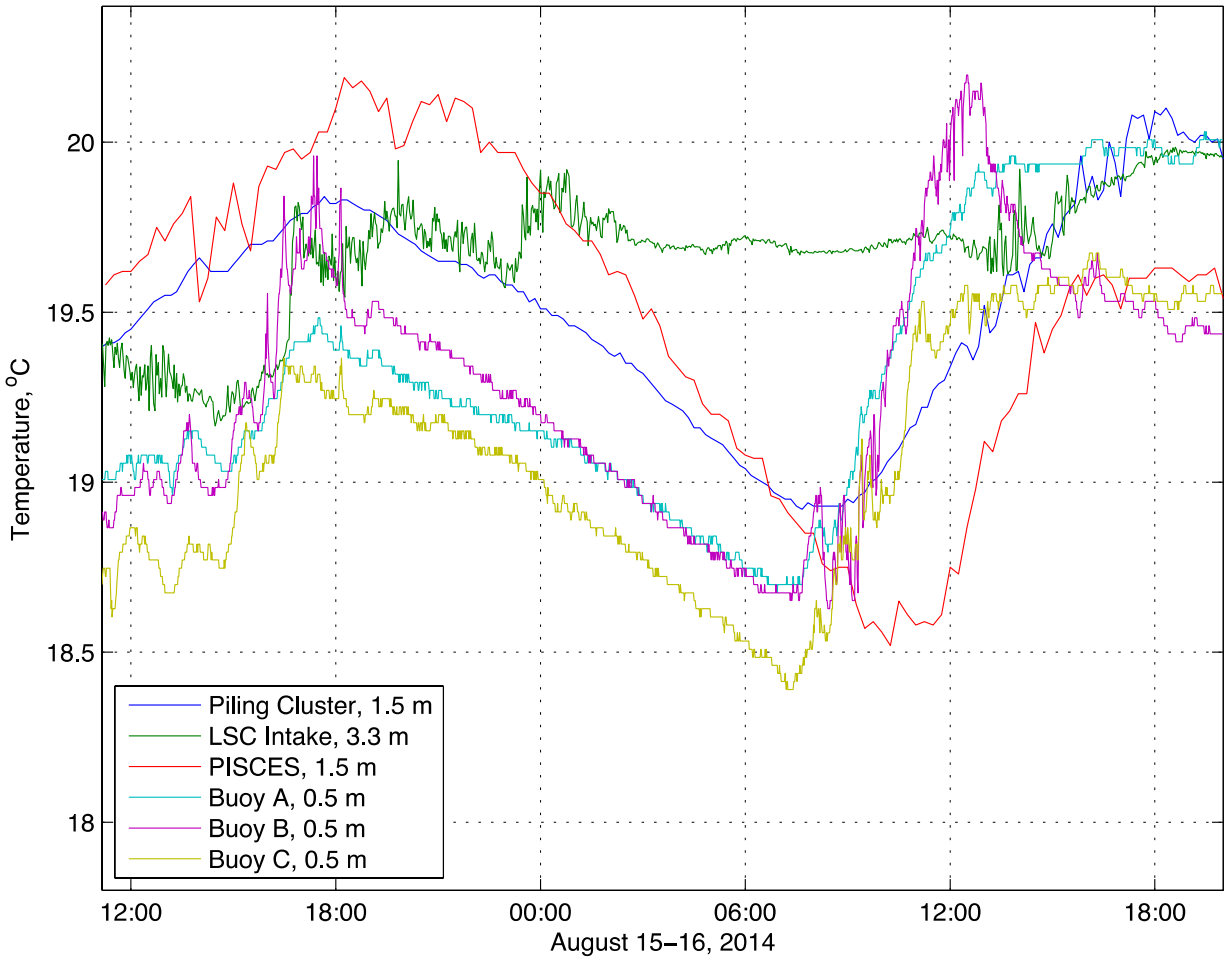

Figure A-7. Temperatures measured at the moored thermistors during the 2014 gridding study. Only the temperature from the top-most thermistor on the LSC intake string is plotted here.

A.3 Classification and Description of the LSC Outfall Plume

CORMIX is a USEPA-supported mixing zone model and decision support system for environmental impact assessment of regulatory mixing zones resulting from continuous point source discharges. CORMIX II was developed specifically for assessing multiport diffusers and classifies multiport diffuser plumes using a decision tree documented in Akar and Jirka (1991). The flow class depends on the geometry of the diffuser, the effluent flow rate, the effluent density, and characteristics of the receiving water at the diffuser site. In this section we demonstrate that over 99% of the time, the LSC diffuser plume belongs to flow class MNU7 or MU2, and we present the equations governing dilution, centerline velocity, and plume width for these classes of flow. We also present a version of the intermediate-field equations for these quantities that takes friction into account, which is not included in CORMIX II, but is more accurate, and is the set of equations we use to model the LSC outfall within our 3D model.

A.3.1 Classification of the LSC Outfall Plume Using CORMIX II

The as-built LSC outfall pipe extends into Cayuga Lake from the heat exchange facility on the east shore, at an angle 26° south of west (see Figure A-8). The diffuser consists of 38 nozzles spanning the final length L_D=22.8m of the outfall pipe. Diffuser ports are perpendicular to the pipe, pointing 26° west of north (fairly parallel to but slightly away from the east shore and towards the north end of the lake). The center of the diffuser section is located at UTM Zone 18T coordinate (376256mE, 4703137mN) at a depth of H=3.9m (at mean summer lake level, which is 116.6m above NGVD 1929). Diffuser nozzles are located h_0=0.3m above the bed and discharge at an angle θ=20.0° above horizontal. Each nozzle consists of a 6-in standard Inserta® tee. With a 0.61 area ratio for the vena contracta (appropriate at the high Reynolds numbers typical of the diffuser), total port area is A_0=0.423m^2. Temperature and volumetric flow rate of the discharge have been measured hourly at the LSC HXF from January 2005 to present. The ambient water temperature on the shelf has been measured at the piling cluster between 1998 and present. Time series of effluent flow rate (Q_0) and temperature (T_0) are plotted along with temperature of the ambient shelf water (T_a) in Figure A-9. The receiving water is shallow and within the epilimnion (except briefly during upwelling events, which cause significant vertical mixing), so stratification is negligible.

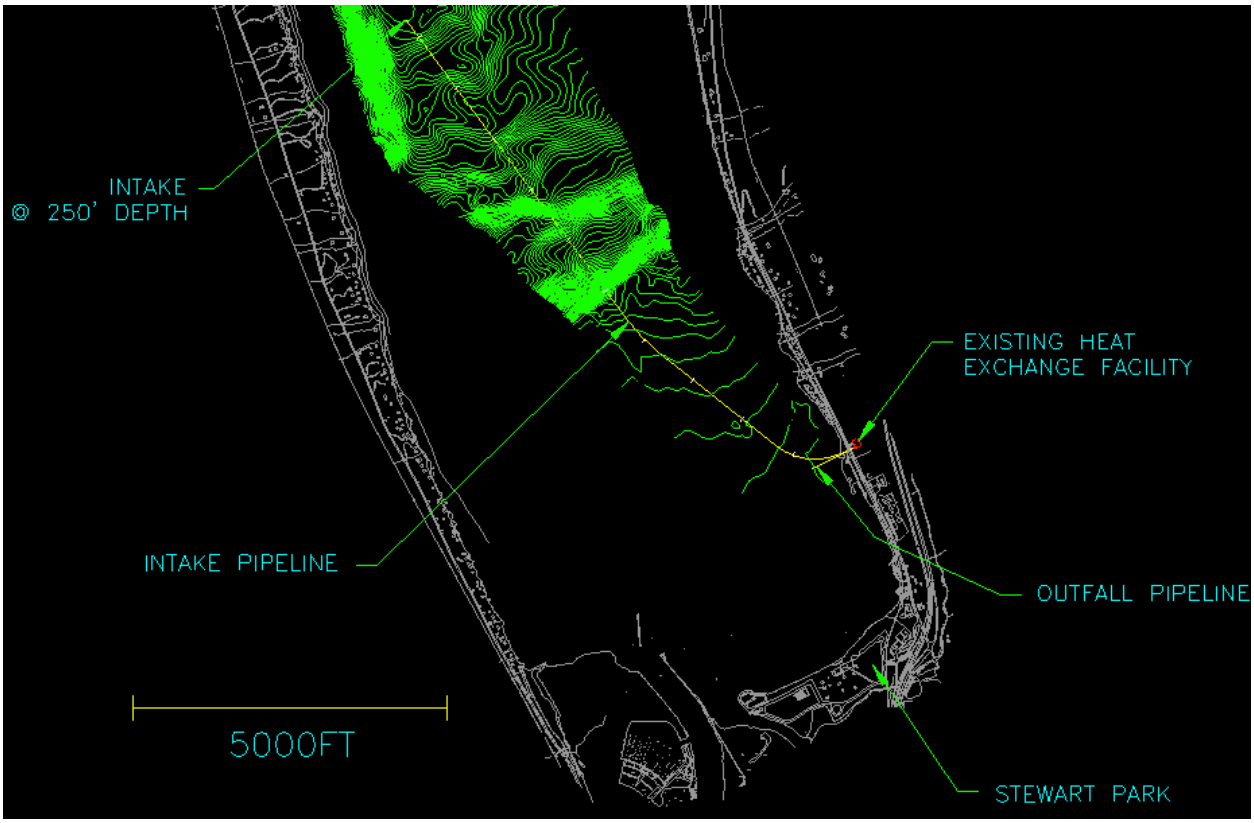

Figure A-8. Map of LSC outfall and Intake pipelines. This is an excerpt from the as-built drawings. Green lines represent depth contours from the as-built survey.

The CORMIX II flow classification system for discharge into unstratified ambient water is based on the following two-dimensional parameters: flow rate per unit length $q_0=Q_0/L_D$, momentum flux $m_0=q_0u_0$, and

buoyancy flux $j_0=q_0g_0'$ where $u_0=Q_0/A_0$ is the port velocity and $g_0'=g(\rho_0-\rho_a)/\rho_a$ is the reduced gravity based on density of the effluent (ρ_0) and ambient (ρ_a) (Akar and Jirka 1991). Time histories of these three quantities for the LSC outfall are plotted in Figure A-10. The LSC outfall plume is strongly negatively buoyant most of the year and weakly positively buoyant during short periods in winter. CORMIX II determines plume stability using the parameter c_7 for negatively buoyant plumes and c_4 for positively buoyant plumes:

$$c_7 = \frac{m_0}{|j_0|^{2/3}H}(1+cos^2\theta)^2 + \frac{u_a^2}{|j_0|^{2/3}} \tag{3}$$

$$c_4 = \frac{m_0}{j_0^{2/3}H}(1+cos^2\theta)^2 + \frac{u_a^2}{j_0^{2/3}} - 0.1\frac{u_a^2 h_0}{m_0} \tag{4}$$

where u_a is the ambient water velocity. We do not know precisely the ambient water velocity at the LSC discharge site, but it is reasonable to assume it is in the range of 1mm/s to 10cm/s.

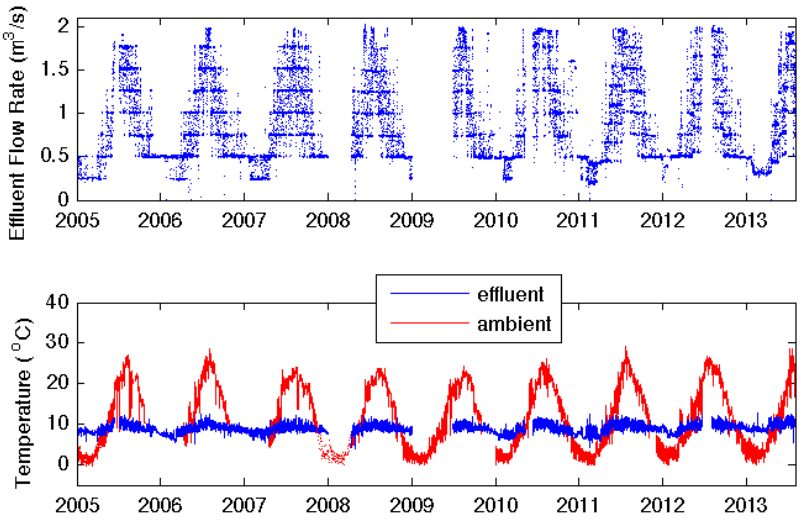

Figure A-9. Time histories of flow rate and temperature of LSC effluent (measured hourly at the heat exchange facility) and ambient temperature of Cayuga Lake (measured at the piling cluster).

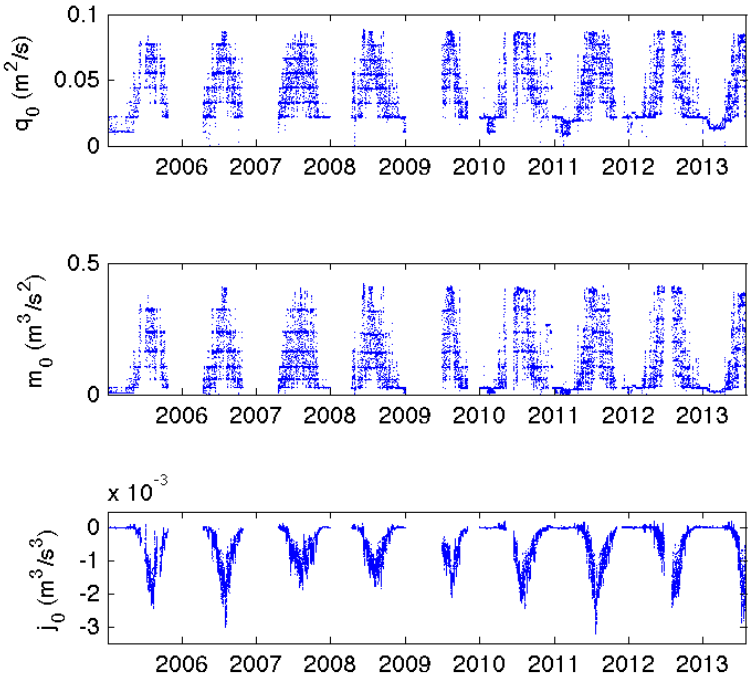

Figure A-10. Time histories of flow rate, momentum flux, and buoyancy flux (all quantities expressed per unit diffuser length) for as-built LSC outfall.

When the stability parameter (c_7 or c_4) is smaller than 0.54, the plume is unstable in the near field, meaning its momentum is strong compared it its buoyancy, mixing the effluent uniformly over the depth of the water column. The time history of the stability parameter (c_7 when the plume is negatively buoyant and c_4 when it is positively buoyant) based on time histories of q_0, m_0, and j_a (plotted in Figure A-10) is plotted in Figure A-11 for ambient velocities between 0 and 1m/s. Even with zero ambient velocity, the plume is unstable greater than 99.97% of the time. Since the diffuser ports are perpendicular to the diffuser pipe, and point unidirectionally along the shore, the plume falls into CORMIX II flow class MNU7 when it is negatively buoyant and flow class MU2 when it is positively buoyant.

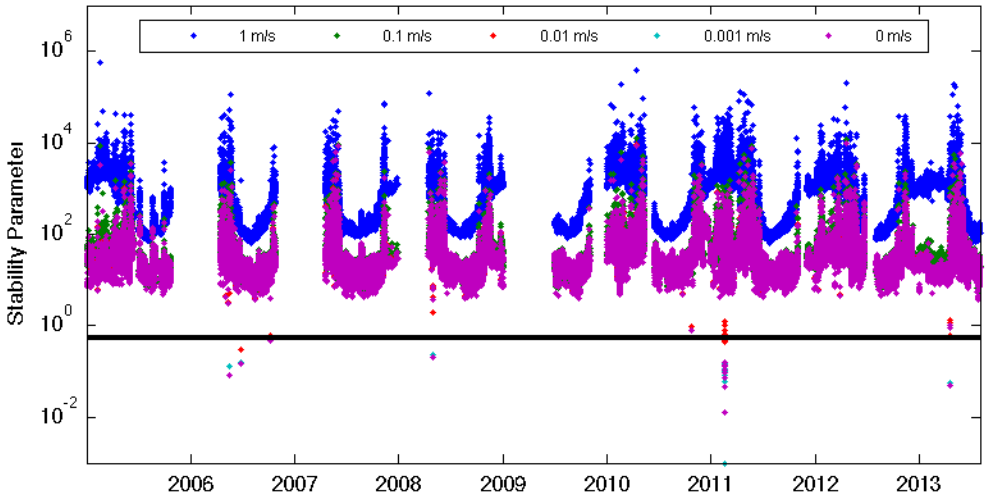

Figure A-11. Time histories of plume stability parameter (equal to c_7 when $j_0<0$ and c_4 when $j_0>0$) for as-built LSC outfall for five different ambient water velocities (indicated in legend). Plume is stable when stability parameter drops below 0.54, which is plotted as a black line.

Flow classes MNU7 and MU2 are identical in the near field and the intermediate field (both defined below), except that if the plume stratifies in the intermediate field, it ends up below the ambient water if it is negatively buoyant (MNU7) and above the ambient water if it is positively buoyant (MU2). In Figure A-12, we show a sketch of the plume for flow class MNU7. CORMIX II software provides the following description of the MNU7 flow class:

> "A unidirectional multiport diffuser with perpendicular alignment is discharging into an ambient flow. Frequently, this is called a 'co-flowing diffuser'. The discharge configuration is hydrodynamically 'unstable', that is the discharge strength (measured by its momentum flux) is very strong in relation to the layer depth and in relation to the stabilizing effect of the discharge buoyancy (measured by its buoyancy flux). Rapid vertical mixing takes place over the full layer depth.
>
> The following flow zones exist:
>
> 1) Acceleration zone for unidirectional coflowing diffuser: The net horizontal momentum flux provided by the diffuser jets leads to a whole scale acceleration of the ambient water, which flows across the diffuser line leading to rapid entrainment and mixing in this zone. The diffuser plume is mixed over the full layer depth, and contracts laterally in the direction of the flow (acceleration process). The length of this zone is about one half the diffuser length.
>
> 2) Diffuser-induced plume in co-flow: The diffuser-induced momentum flux is still controlling the flow. However, lateral entrainment and diffusion lead to spreading of the diffuser plume and additional mixing. The plume moves predominantly in the direction of the ambient flow. At the beginning, the plume is vertically mixed over the full layer depth. At some distance,

stratification may take place depending on the strength and direction of the plume buoyancy."

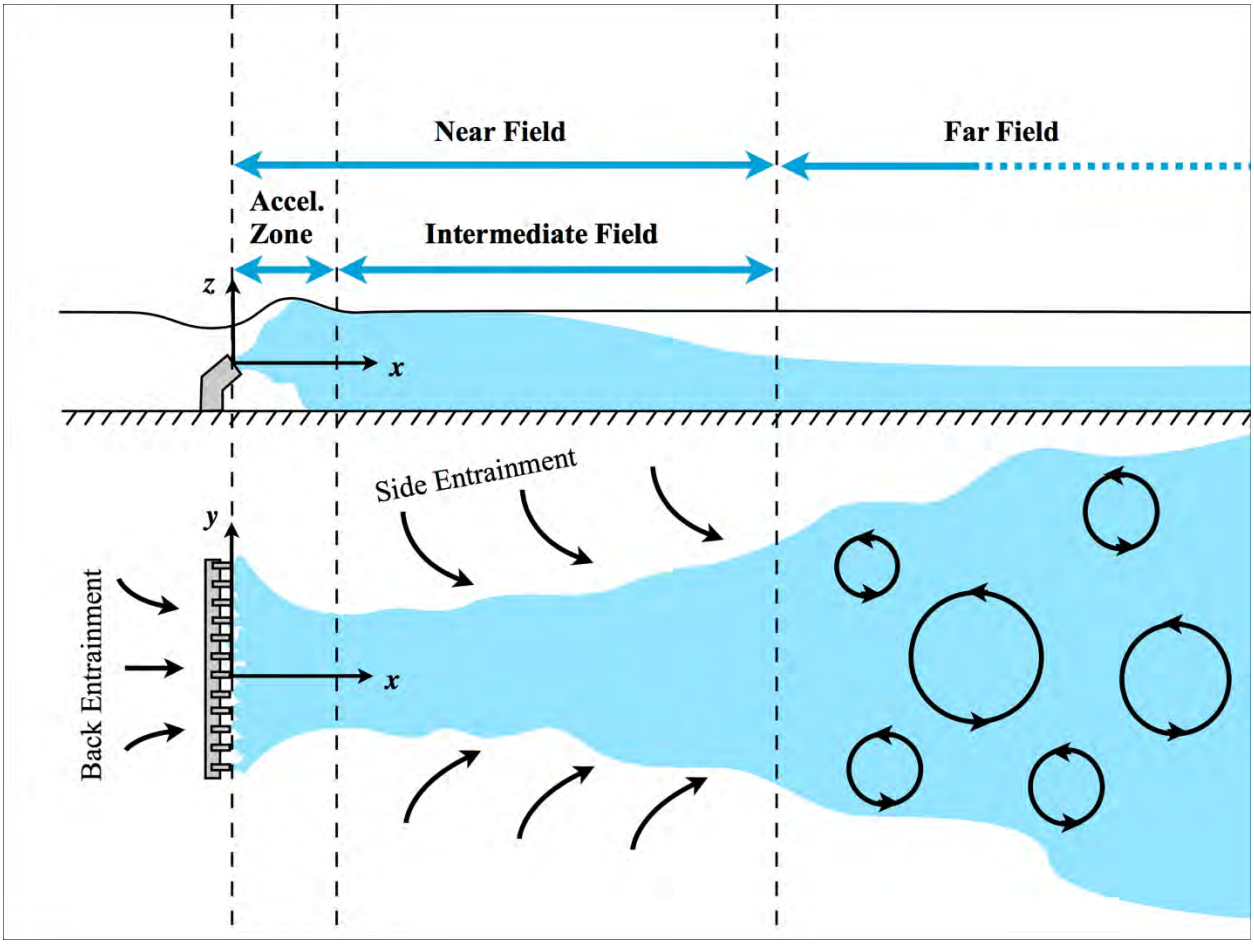

Figure A-12. Side view and plan view sketches of the near field (consisting of the acceleration zone and the intermediate field) and the far field for hydrodynamically unstable plume discharged from a unidirectional multiport diffuser.

These zones comprise the near field and are illustrated in Figure A-12. The first is called the "acceleration zone" and the second is called the "intermediate field". Akar and Jirka (1991) document the empirical formulas used by CORMIX II for dilution and plume half-width, and we review these formulas for the acceleration zone and the intermediate field below, neglecting ambient velocity because it is very small (maximum anticipated 0.1m/s) compared to the diffuser jet velocity (~3.5m/s). But first we must define some quantities Akar and Jirka (1991) use to describe the plume characteristics.

A.3.2 General Definitions Pertaining to Description of Plumes

Within the CORMIX II model, the plume may either take a top-hat shape or a Gaussian shape. For the Gaussian shape, the x-velocity component, the temperature, and the passive tracer concentration are given by:

$$u = u_c \exp\left[-\left(\frac{y}{b_h}\right)^2\right], \tag{5}$$

$$T = (T_c - T_a)\exp\left[-\left(\frac{y}{\lambda b_h}\right)^2\right] + T_a \text{ , and} \tag{6}$$

$$C = (T_c - C_a)\exp\left[-\left(\frac{y}{\lambda b_h}\right)^2\right] + C_a \text{ ,} \tag{7}$$

respectively, where the subscript "c" denotes centerline (the value at $y = 0$), the subscript "a" denotes ambient (the value far from the plume), b_h is the half-width of the velocity profile, and λb_h is the half-width of the temperature and concentration profiles, where λ is an order-one empirical constant. For the top-hat shape, the velocity, temperature, and passive tracer concentration profiles are given by:

$$u = \begin{cases} u_c, & |y| < b_h \\ 0, & |y| \geq b_h \end{cases}, \tag{8}$$

$$T = \begin{cases} T_c + T_a, & |y| < b_h \\ T, & |y| \geq b_h \end{cases}, \text{ and} \tag{9}$$

$$C = \begin{cases} C_c + C_a, & |y| < b_h \\ C_a, & |y| \geq b_h \end{cases}. \tag{10}$$

Note that in the top-hat profile, the half-width for velocity is the same as the half-width for temperature and concentration.

The width of the plume in the vertical direction is denoted b_v, and CORMIX II always assumes a top-hat shape in the vertical plume profile. When the plume is fully mixed over the water depth, $b_v = H$.

The plume flow rate, Q, is the integral across x and y of the plume x-velocity component. Assuming the plume is negatively buoyant (which is true for the LSC outfall in summer):

$$Q = \int_0^{b_h} \int_{-\infty}^{\infty} u \; dy \; dz \,. \tag{11}$$

Dilution, denoted by S within the CORMIX II documentation, is proportional to plume flow rate and inversely proportional to plume temperature and concentration. There are two precise definitions of dilution, and the CORMIX II documentation is not always clear which is used. Bulk dilution is defined as:

$$\bar{S} = \frac{Q}{Q_0} \tag{12}$$

where Q_0 is the initial discharge. Centerline dilution is defined as:

$$S_c = \frac{T_0 - T_a}{T_c - T_a} = \frac{C_0 - C_a}{C_c - C_a}. \quad (13)$$

The relationship between $\bar{S}$ and S_c depends on the shape of the plume velocity profile. For a top-hat shape, $\bar{S} = S_c$, and for a Gaussian shape:

$$\bar{S} = S_c \frac{\sqrt{1+\lambda}}{\lambda}. \quad (14)$$

A.3.3 Equations Describing the LSC Outfall Plume within CORMIX II

Now that we have defined profile shapes and dilution rates, we may describe the plume characteristics for flow class MNU7 according to CORMIX II. Recall there are two regions: the acceleration zone, and the intermediate field. Within the acceleration zone, the plume is fully mixed over depth, i.e., $b_v = H$, and there is no side entrainment. Within the intermediate field, there is significant side entrainment, and while at first the plume remains fully mixed over depth, it may re-stratify some distance downstream.

Acceleration Zone

The acceleration zone spans x=0 to x=L_D/2. The plume contracts by a factor of two within the acceleration zone, starting with half-width b_h=L_D/2 at x=0 and ending with half-width b_h=L_D/4 at x=L_D/2. Dilution is constant within the acceleration zone and given by:

$$\bar{S} = \sqrt{\frac{m_0 H}{2q_0}}. \quad (15)$$

The flow rate induced behind the diffuser, called “back entrainment” is equal to:

$$Q_m = Q_0(\bar{S} - 1). \quad (16)$$

For the LSC discharge, Q_m is often $\sim 10Q_0$, meaning the flow induced by the outfall is an order of magnitude larger than the flow from the outfall itself.

The half-width of the diffuser within the acceleration zone is approximated by:

$$b_h = \tfrac{1}{2}L_D\left\{\tfrac{1}{2} + \tfrac{1}{2}\exp\left(-3\tfrac{2x}{L_D}\left[1 + \left(\tfrac{2x}{L_D}\right)^3\right]\right)\right\}. \quad (17)$$

The plume approximates a top-hat profile within the acceleration zone. Thus, the centerline velocity is equal to the velocity across the entire profile and is equal to:

$$u_c = \frac{Q}{b_h H}. \tag{18}$$

Intermediate Field

The intermediate field begins at y=L_D/2. In this region, side entrainment is significant, so the flow rate grows downstream. Dilution grows with the square root of distance as follows:

$$S = S_{50}\sqrt{\frac{m_0 H \cos\theta_0\,(x - x_V)}{q_0^2 L_D}} \tag{19}$$

and the plume half-width grows linearly as:

$$b_h = B_{50}(x - x_V) \tag{20}$$

where the virtual origin is located at:

$$x_V = \frac{L_D}{2}\left(1 - \frac{1}{S_{50}^2}\right) \tag{21}$$

and S_{50}=0.58 and B_{50}=0.21 are empirical constants. The plume is assumed to take a Gaussian shape in the intermediate field. Akar and Jirka (1991) do not specify whether the formula given for S within the intermediate field is meant to describe the bulk dilution or the centerline dilution.

Some distance downstream, either within the intermediate field or the far field, the plume may stratify. If the plume stratifies within the intermediate field, CORMIX II assumes the dilution continues to evolve according to Equation (19), but the half-width evolves differently, as follows:

$$b_h = BB_{50}\,\frac{j_o^{1/3} H^{1/2}}{m_0^{1/2} L_D^{1/6}}\left[(x - x_v)^{7/4} - (x_t - x_v)^{7/4}\right] + b_{ht} \tag{22}$$

where $BB_{50} = 0.25$ is an empirical constant, $x = x_t$ is the location of transition from unstratified to stratified flow, and $b_{ht} = b_h(x_t)$. The plume height in the stratified region of the intermediate field evolves according to:

$$b_v = \frac{S_t b_{ht} H}{b_h S}. \tag{23}$$

The location of transition from unstratified intermediate field to stratified intermediate field is determined by the Froude number. The flow stratifies once the centerline Froude number $Fr_c = 2.5$, where centerline Froude number is defined as:

$$Fr_c = \frac{u_c}{\sqrt{g_c' H}} \tag{24}$$

and centerline reduced gravity, g_c', is given by:

$$g_c' = \frac{g_0'}{S_c}. \tag{25}$$

A.3.4 Equations Describing Plumes of Type MNU7 with Bed Friction

The CORMIX II solutions for plume evolution in the intermediate field do not take bed friction into account, and we found in our simulations that bed friction was significant. Akar and Jirka (1991) reference Lee and Jirka (1980), an article that describes the intermediate field of plume type MNU7 when bed friction is significant. The results of Lee & Jirka (1980) apply to the region of the plume that is fully mixed over depth, but we may assume that the dilution rate also applies to the stratified portion of the intermediate field.

Lee and Jirka (1980) divide the intermediate field into two regions:

(1) the zone of flow establishment (ZOFE), where the velocity profile transitions from the top-hat shape of the acceleration zone to the Gaussian shape farther downstream, and
(2) the zone of established flow (ZOEF), where the velocity profile is Gaussian.

Within the ZOFE, the velocity profile takes the following form:

$$u = \begin{cases} u_c \exp\left[-\left(\dfrac{|y| - \delta(x)}{b_h}\right)^2\right], & |y| > \delta(x) \\ u_c \qquad\qquad\qquad\qquad\quad , & |y| \le \delta(x). \end{cases} \tag{26}$$

Lee and Jirka derive the form of $u_c(x)$, $b_h(x)$, and $\delta(x)$ in these two zones, allowing for different entrainment coefficients α_1 and α_2 in the ZOFE and ZOEF, respectively. They define a dimensionless quantity to characterize the influence of friction: the far-field parameter

$$\phi = \frac{C_D L_D}{2H} \tag{27}$$

where C_D is the drag coefficient at the bed, L_D is the length of the diffuser, and H is the water depth. The following downstream coordinate, velocity, and half-width mark the end of the ZOFE and the beginning of the ZOEF:

$$x_I = \frac{L_D}{2\phi}\left[\ln u_0 - \ln\left(1 - \frac{(\sqrt{2}-1)\phi}{2\alpha_1}\right)\right] \tag{28}$$

$$u_I = \sqrt{\frac{2m_0}{H}}\left(1 - \frac{(\sqrt{2}-1)\phi}{2\alpha_1}\right) \tag{29}$$

$$b_I = \frac{L_D}{2}\sqrt{\frac{2}{\pi}}\left(1 - \frac{(\sqrt{2}-1)\phi}{2\alpha_1}\right)^{-1} \tag{30}$$

where we have substituted the dimensionless function $u_0(\phi)$ for an integral in Lee & Jirka (1980). The approximation $u_0(\phi) \approx 1.000 + 0.1890\phi + 0.0492\phi^2 + 0.0171\phi^3$ is correct to within 0.0001 on the interval ϕ = 0 to 1 (for the LSC diffuser, $\phi \sim 0.01$, with the precise value depending on the bottom drag coefficient).

Within the ZOFE, Lee and Jirka find that the plume evolves as follows:

$$u_c(x) = \sqrt{\frac{2m_0}{H}}u_0 e^{-\frac{2\phi x}{L_D}} \tag{31}$$

$$b_h(x) = \frac{\alpha_1 L_D}{(\sqrt{2}-1)\phi u_0} e^{\frac{2\phi x}{L_D}}\left(1 - u_0 e^{-\frac{2\phi x}{L_D}}\right) \tag{32}$$

$$\delta(x) = \frac{L_D}{4u_0} e^{\frac{2\phi x}{L_D}}\left[1 - \frac{2\alpha_1}{(\sqrt{2}-1)\,\phi}\left(1 - u_0 e^{-\frac{2\phi x}{L_D}}\right)\right], \tag{33}$$

and within the ZOEF, Lee and Jirka find that the plume evolves as follows:

$$u_c(x) = u_I e^{-\frac{2\phi}{L_D}(x - x_I)}\left[1 + \frac{8\alpha_2}{\sqrt{\pi}b_I}(x - x_I)\right]^{-1/2} \tag{34}$$

$$b_h(x) = b_I e^{\frac{2\phi}{L_D}(x - x_I)}\left[1 + \frac{8\alpha_2}{\sqrt{\pi}b_I}(x - x_I)\right] \tag{35}$$

$$u_c(x) = \sqrt{\frac{2m_0}{H}}u_0 e^{-\frac{2\phi x}{L_D}} \tag{36}$$

Note that within the ZOEF, the bulk dilution is given by:

$$\bar{S} = \frac{\sqrt{\pi}u_c b_h H}{Q_0} \tag{37}$$

and the centerline dilution by:

$$S_c = \frac{\lambda}{\sqrt{1+\lambda}} \frac{\sqrt{\pi} u_c b_h H}{Q_0}. \tag{38}$$

There are no empirical results available describing evolution of u_c and b_h for the stratified region of the intermediate field in the presence of strong bed friction. For purposes of comparison to our model results, we assume that $\bar{S}$ and S_c continue to evolve as they did for the ZOEF, and for lack of a better recourse, assume that the transition point still occurs when $Fr_c = 2.5$ and that b_h evolves according to (22).

A.4 Three-Dimensional Modeling

A.4.1 Introduction

Numerical simulations were conducted with the 3-D free surface hydrodynamic model, Si3D (Rueda 2001; Smith 2006, Rueda and Cowen 2005, Rueda et al. 2008; Acosta et al. 2015). Si3D is based on the continuity equation for incompressible fluids, the Reynolds-averaged form of the Navier-Stokes equations for momentum, the transport equation for temperature, and an equation of state relating temperature to fluid density. The governing hydrodynamic equations are solved in layer-averaged form using a semi-implicit, three-level, leapfrog- trapezoidal finite difference scheme on a staggered Cartesian grid; only the vertical diffusive components of transport are treated implicitly. The scalar transport equation is solved using a two-level semi-implicit scheme; the advective scalar fluxes are estimated using flux-limiter methods. Vertical turbulent mixing is represented in the 3-D model following the level 2.5 Mellor-Yamada hierarchy of turbulence closure models (Kantha and Clayson 1994). Horizontal diffusive fluxes of momentum and scalars are parameterized using a constant eddy viscosity and a constant eddy diffusivity, respectively. The numerical grid, boundary conditions, and initial conditions are described below.

A.4.2 Addition of Point Source Model to Si3D

A.4.2.1 Modification of Governing Equations to Accommodate Point Sources

The governing equations within Si3D, before discretization, are presented below. Point sources are incorporated through the source strength term σ, the source velocity (u_0,v_0), the source temperature T_0, and the source passive tracer concentration C_0 following Singleton et al. (2010). Note that these investigators did not include the source strength in the integrated continuity equation because it is negligible for bubble plumes; we do include this component in our analysis.

Continuity equation (conservation of mass):

$$\frac{\partial u}{\partial x}+\frac{\partial v}{\partial y}+\frac{\partial w}{\partial z}=\sigma \tag{39}$$

where t is time, (x,y,z) are the two horizontal coordinates and the vertical coordinate, respectively, and (u,v,w) are the corresponding components of water velocity. Incorporating the kinematic boundary condition for the water surface elevation into the continuity equation and integrating over the water depth.

$$\frac{\partial \zeta}{\partial t}+\frac{\partial}{\partial x}\left[\int_{-H}^{\zeta} u dz\right]+\frac{\partial}{\partial y}\left[\int_{-H}^{\zeta} v dz\right]=\int_{-H}^{\zeta}\sigma dz \tag{40}$$

where the vertical coordinate, z, is zero at a reference elevation near the water surface, ζ is elevation of the water surface above that reference, and the bed is located at z = –H.

Conservation of momentum (x-component):

$$\begin{aligned}\frac{\partial u}{\partial t}+u\frac{\partial u}{\partial x}+v\frac{\partial u}{\partial y}+w\frac{\partial u}{\partial z}-fv \\ =-\left(g\frac{\partial \zeta}{\partial x}+g\frac{1}{\rho_0}\int_z^{\zeta}\frac{\partial \rho}{\partial x}d\xi\right)+\frac{\partial}{\partial x}\left(A_H\frac{\partial u}{\partial x}\right)+\frac{\partial}{\partial y}\left(A_H\frac{\partial u}{\partial y}\right)+\frac{\partial}{\partial z}\left(A_V\frac{\partial u}{\partial z}\right) \\ +\sigma(u-u_0)\end{aligned} \tag{41}$$

Conservation of momentum (y-component):

$$\begin{aligned}\frac{\partial v}{\partial t}+u\frac{\partial v}{\partial x}+v\frac{\partial v}{\partial y}+w\frac{\partial v}{\partial z}+fu \\ =-\left(g\frac{\partial \zeta}{\partial y}+g\frac{1}{\rho_0}\int_z^{\zeta}\frac{\partial \rho}{\partial y}d\xi\right)+\frac{\partial}{\partial x}\left(A_H\frac{\partial v}{\partial x}\right)+\frac{\partial}{\partial y}\left(A_H\frac{\partial v}{\partial y}\right)+\frac{\partial}{\partial z}\left(A_V\frac{\partial v}{\partial z}\right) \\ +\sigma(v-v_0)\end{aligned} \tag{42}$$

where f is the Coriolis parameter, g is the acceleration of gravity, ρ is the water density, ρ_0 is the reference water density, and A_H and A_V are the horizontal and vertical turbulent eddy viscosities, respectively. A_V is calculated using a standard second order turbulence closure model (based on the

Mellor-Yamada 2.5 level scheme — Kantha and Clayson, 1994), and A_H is set to a constant which may be calibrated. We incorporate our intermediate-field plume mixing model through A_H.

Transport equation for temperature:

$$\frac{\partial T}{\partial t} + u\frac{\partial T}{\partial x} + v\frac{\partial T}{\partial y} + w\frac{\partial T}{\partial z} = \frac{\partial}{\partial x}\left(D_H\frac{\partial T}{\partial x}\right) + \frac{\partial}{\partial y}\left(D_H\frac{\partial T}{\partial y}\right) + \frac{\partial}{\partial z}\left(D_V\frac{\partial T}{\partial z}\right) + \frac{1}{\rho_0 c_p}\frac{\partial I}{\partial z} + \sigma(T - T_0) \quad (43)$$

Where T is temperature, D_H and D_V are horizontal and vertical eddy diffusivities, respectively, c_p is the specific heat of water, and I is downward solar irradiance. D_H and D_V are proportional to A_H and A_V, respectively, and we assume a proportionality constant ("turbulent Schmidt number") of 1, i.e. A_H=D_H.

Transport equation for each passive tracer:

$$\frac{\partial C}{\partial t} + u\frac{\partial C}{\partial x} + v\frac{\partial C}{\partial y} + w\frac{\partial C}{\partial z} = \frac{\partial}{\partial x}\left(D_H\frac{\partial C}{\partial x}\right) + \frac{\partial}{\partial y}\left(D_H\frac{\partial C}{\partial y}\right) + \frac{\partial}{\partial z}\left(D_V\frac{\partial C}{\partial z}\right) + \sigma(C - C_0) \quad (44)$$

where C is tracer concentration.

Within each computational cell receiving a portion of the effluent from LSC, IAWWTF, or CHWWTF, σ is set to the volumetric flow rate discharged into that cell divided by the cell volume, and u_0, v_0, T_0, and C_0 are specified based on the diffuser and effluent properties. Within the cell containing the LSC intake, σ is set to negative one times the intake volumetric flow rate divided by the volume of the cell, u_0 and v_0 are specified based on the intake geometry and the flow rate, and T_0 and C_0 are set to the ambient values (i.e., there is no sink in the equations for T or C).

A.4.2.2 Modification of Horizontal Viscosity and Diffusivity to Obtain Correct Intermediate Field Behavior of the LSC Outfall Plume

We may enforce the plume evolution predicted by Lee and Jirka (1980), as described in Section **A.3.4**, within our 3D model by adjusting the horizontal eddy viscosity and diffusivity in the vicinity of the LSC outfall. We determine the required value of eddy viscosity by solving the boundary layer equations for conservation of mass and momentum, assuming uniform flow in z. Assuming the plume is fully mixed over depth, and that velocity is uniform in the vertical direction, the equation for conservation of mass, downstream of the source, is

$$\frac{\partial u}{\partial x} + \frac{\partial v}{\partial y} = 0 \tag{45}$$

and the equation for conservation of momentum, downstream of the source, simplifies to

$$u\frac{\partial u}{\partial x} + v\frac{\partial u}{\partial y} = \frac{\partial}{\partial y}\left(A_H \frac{\partial u}{\partial y}\right) - \frac{C_D}{H}u^2 \tag{46}$$

where v is the y-component of velocity, and A_H is the horizontal eddy viscosity. We may solve for the value of $A_H(x, y)$ required to obtain the plume behavior predicted by Lee and Jirka (1980). Before solving for A_H using the momentum conservation equation, we must evaluate the y-component of velocity using the mass conservation equation. These solutions for v are also useful for comparing the results of the 3D model to Lee and Jirka's predictions.

Within the ZOFE, past the acceleration zone ($\frac{1}{2}L_D \le x \le x_I$) and outside the potential core ($|y| > \delta(x)$), we find

$$v = \begin{cases} \operatorname{sign}(y)\left\{ \begin{array}{r} -\dfrac{d(u_c\delta)}{dx} + \dfrac{u_c}{b_h}\dfrac{db_h}{dx}(|y|-\delta)\exp\left[-\left(\dfrac{|y|-\delta}{b_h}\right)^2\right] \\ -\dfrac{\sqrt{\pi}}{2}\dfrac{d(u_c b_h)}{dx}\operatorname{erf}\left(\dfrac{|y|-\delta}{b_h}\right) \end{array} \right\}, & |y| > \delta(x) \\ -y\dfrac{du_c}{dx}, & |y| \le \delta(x) \end{cases} \tag{47}$$

and within the ZOEF we find

$$v(x,y) = \frac{u_c}{b_h}\frac{db_h}{dx} y \exp\left(-\frac{y^2}{b_h^2}\right) - \frac{\sqrt{\pi}}{2}\frac{d(u_c b_h)}{dx}\operatorname{erf}\left(\frac{y}{b_h}\right). \tag{48}$$

Plugging into the momentum conservation equation, we arrive at the following equation for horizontal eddy viscosity within the ZOFE, past the acceleration zone ($\frac{1}{2}L_D \le x \le x_I$) and outside the potential core ($|y| > \delta(x)$):

$$A_H(x,y) = \frac{1}{\sqrt{2}\left(\sqrt{2}-1\right)}\,\alpha_1 u_c(x) b_h(x)\left(\frac{b_h(x)}{|y|-\delta(x)}\right)\left\{\operatorname{erf}\left(\frac{|y|-\delta(x)}{b_h(x)}\right) + \frac{1}{\sqrt{2}}\left[e^{\left(\frac{|y|-\delta(x)}{b_h(x)}\right)^2}\operatorname{erfc}\left(\frac{|y|-\delta(x)}{b_h(x)}\right) - 1\right]\right\} \tag{49}$$

and the following equation within the ZOEF

$$A_H(x,y) = \frac{1}{2}\alpha_2 u_c(x) b_h(x)\left(\frac{b_h(x)}{y}\right)\operatorname{erf}\left(\frac{y}{b_h(x)}\right) \tag{50}$$

Downstream of the LSC outfall point source within Si3D, we set the horizontal eddy viscosity and the horizontal eddy diffusivity equal to the values derived in this section, using the values of u_c, b_h, and δ derived by Lee and Jirka (1980), the goal being to obtain the plume behavior predicted by Lee and Jirka in the unstratified intermediate field. The back-entrainment and behavior within the acceleration zone should be determined by the momentum equations already solved by Si3D. And we do not explicitly add the behavior of the stratified intermediate field. We use a turbulent Schmidt number of one, i.e. turbulent eddy viscosity and turbulent eddy diffusivity are equal, and for simplicity we assume $\alpha_1 = \alpha_2$ and $\lambda = 1$.

A.4.2.3 Testing of Point Source Model

Before applying the point source model to Cayuga Lake, we test that it obtains the correct analytical solutions within a simple rectangular basin of uniform depth. We use parameters typical of the LSC outfall:

Q_0 = 1.5m^3/s
v_0 = 3.5478m/s (since A_0=0.4228m^2)
L_D = 23m
H = 3.0m
C_D = 0.002

We used an ambient temperature of T_a=20°C, and we tested both a neutrally buoyant discharge (T_0=20°C) and a typical summer discharge buoyancy (T_0=11°C)

Note since the flow is to the north, to compare to the equations developed by Lee and Jirka (1980) and in Section **A.4.2.2** , we must exchange x and y, and u and v.

We tested a range of domain sizes, settling on L_x=5750m as a compromise between minimization of boundary effects and simulation time, where L_x is the total length of the domain in the x and y directions, and the point source is located in the middle of the domain. The outfall discharges in the horizontal plane (the actual outfall discharges at a 20^o angle above horizontal, but $\cos(20^o)$=0.93, this it is close enough).

We tested grid cell sizes, Δx=Δy between 5m and 125m, finding that a resolution of 25m was required to resolve the intermediate field and obtain the correct back entrainment to a satisfactory degree. And we tested grid cell depths Δz of 0.1m to 3.0m, finding that 0.1m was required to obtain steady state solutions for the negatively buoyant plume.

Here we present the results of the point source model testing with L_x=5750m, Δx=Δy=25m, and Δz =0.1m

(1) for the neutrally buoyant discharge, and
(2) for the negatively buoyant discharge.

For the neutrally buoyant discharge we compare to Lee & Jirka (1980) solutions, and for the negatively buoyant discharge we compare to Lee & Jirka (1980) in the near field and the unstratified portion of the intermediate field; in the stratified portion of the intermediate field, we use the Lee & Jirka solutions for dilution, and the CORMIX II solutions for plume half-width; we use the Lee & Jirka solutions to compute the transition point from the unstratified to stratified portion of the intermediate field (where Fr_c=2.5).

Neutrally Buoyant Point Source

In Figure A-13, Figure A-14, and Figure A-15, we compare the Si3D predictions for a neutrally buoyant point source to the Lee & Jirka (1980) solutions. We find good agreement, except near the boundaries, where we expect some effects due to the non-infinite domain (the Lee & Jirka solutions assume an infinite domain). The prediction of the back entrainment is particularly good (see flow rate at y=0 in Figure A-14), which is important because back entrainment likely has a large influence on circulation on the southern shelf of Cayuga Lake.

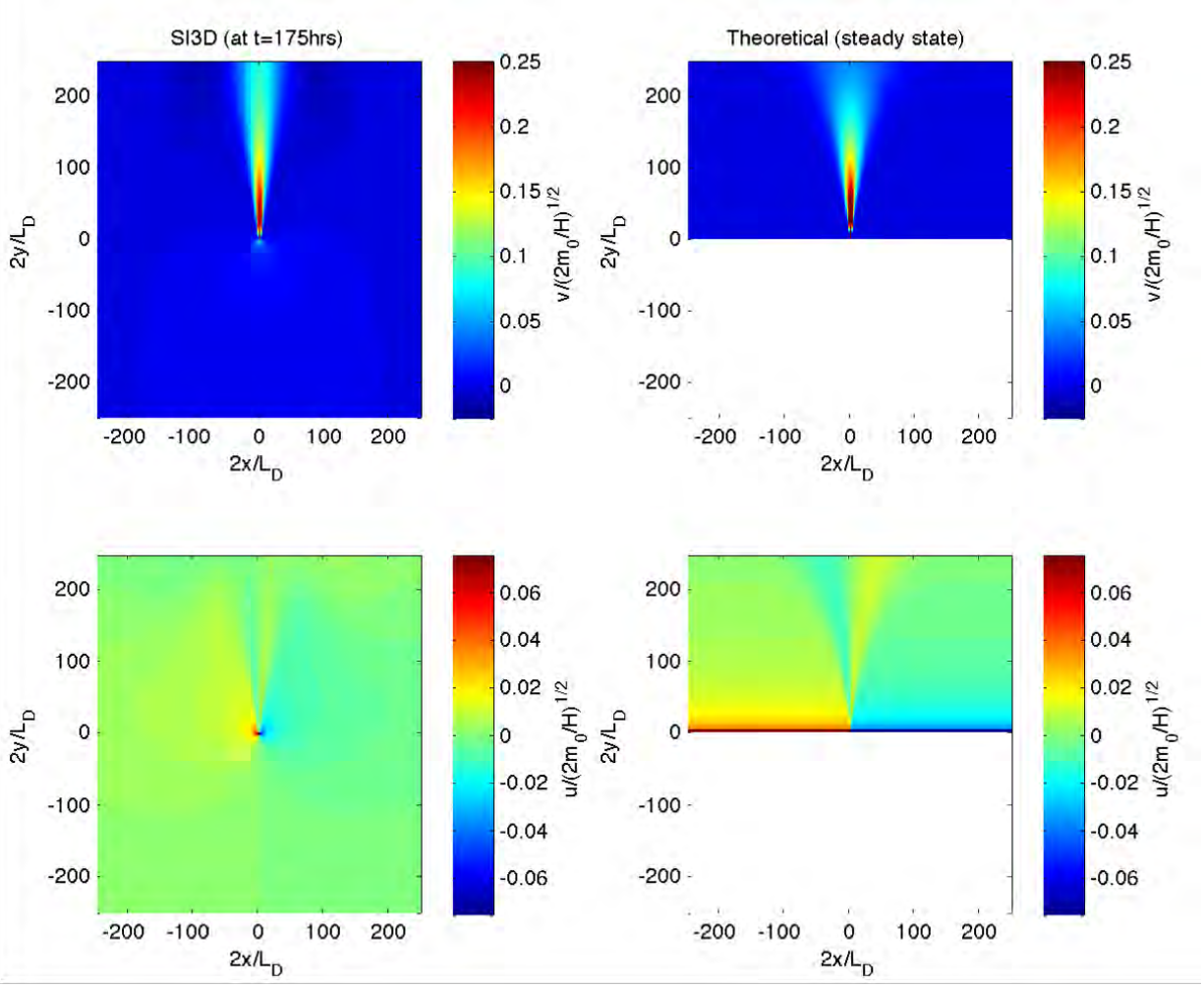

Figure A-13. Comparison of Si3D to Lee & Jirka (1980) (theoretical) solutions for u and v for a neutrally buoyant discharge at steady state. Note the theoretical solution is not defined for y<0. These Si3D velocities are depth-averaged.

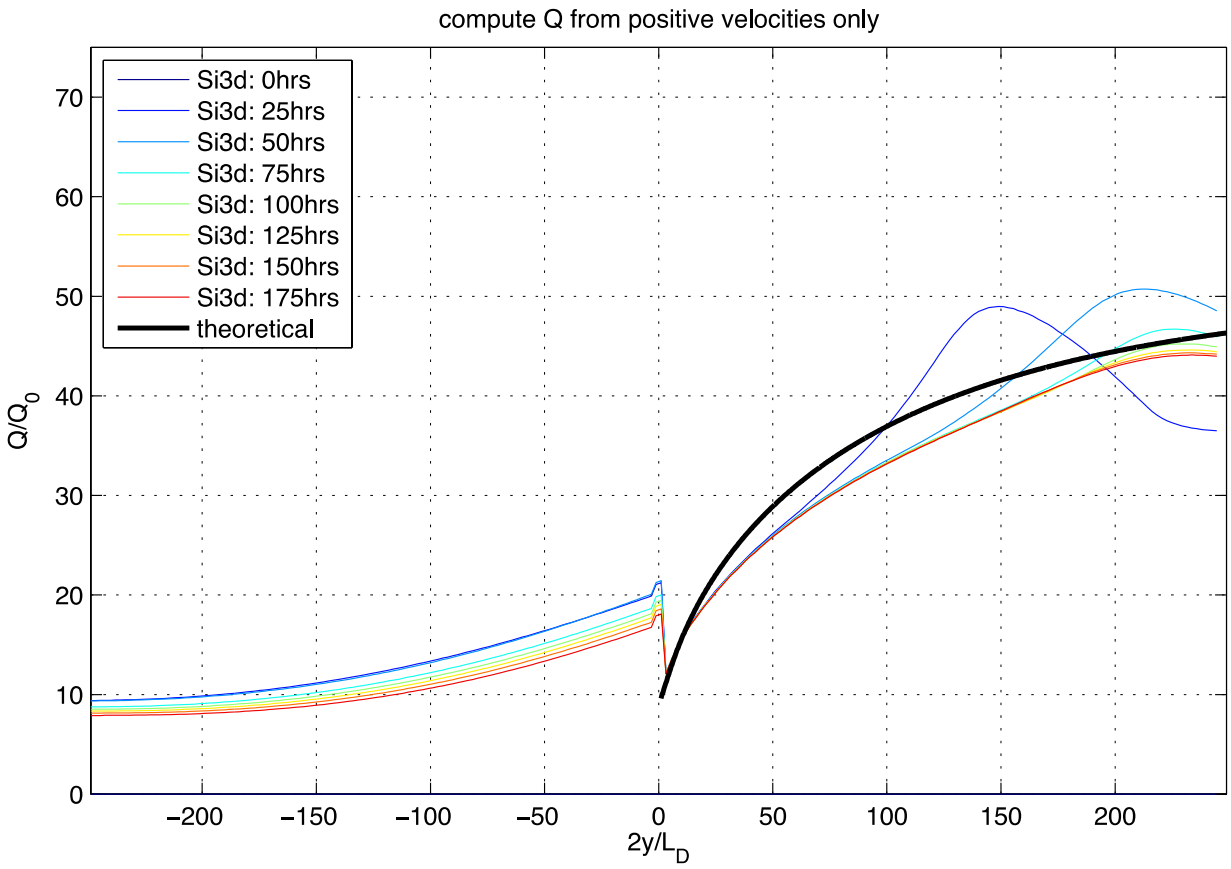

Figure A-14. Comparison of Si3D to Lee & Jirka (1980) (theoretical) solution for bulk dilution for a neutrally buoyant discharge. Note the theoretical solution is not defined for y<0. The flow rate within Si3D at location y is evaluated by integrating all positive v across x and z. Solutions are shown at different times to illustrate the approach to steady state.

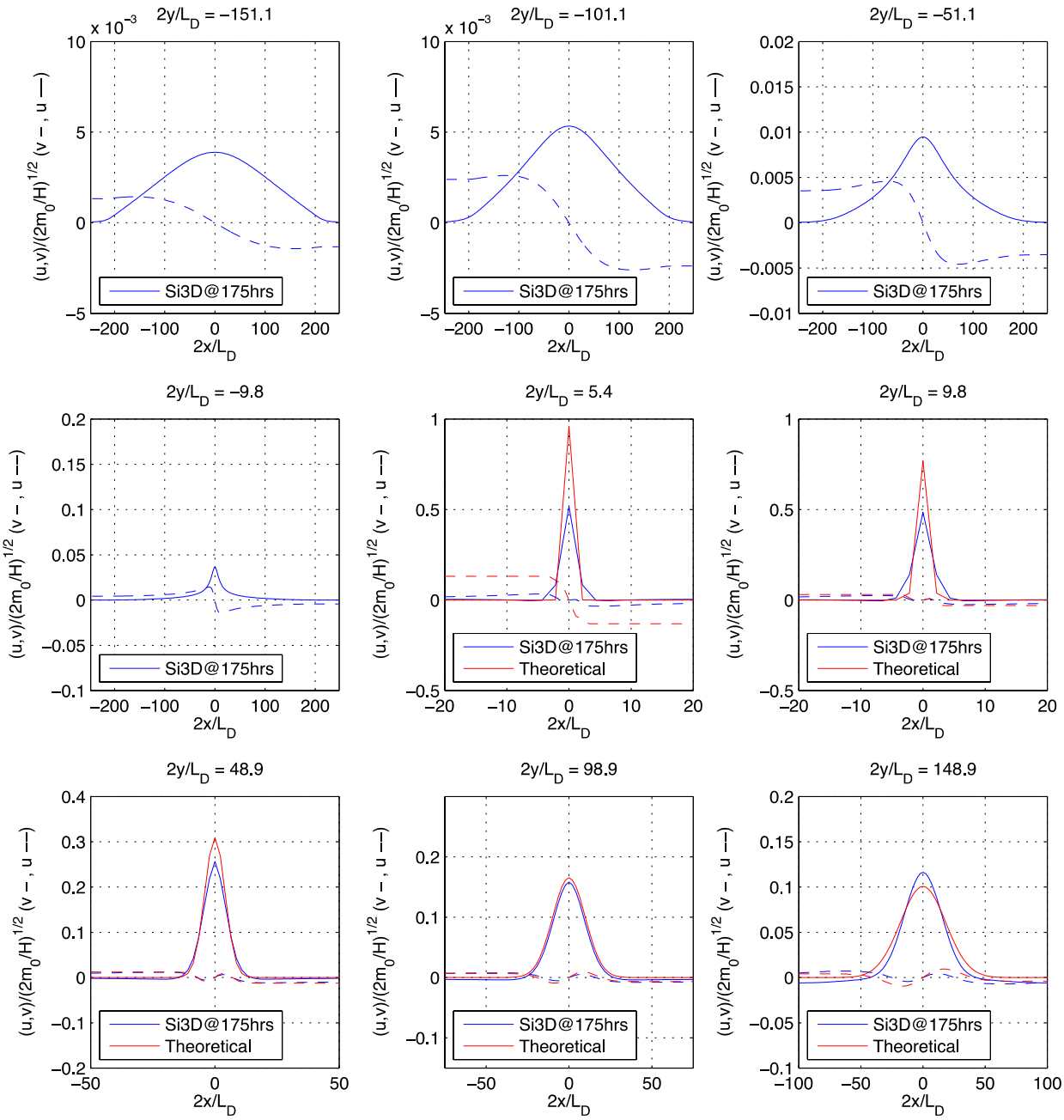

Figure A-15. Comparison of Si3D to Lee & Jirka (1980) (theoretical) solutions for u and v for a neutrally buoyant discharge at steady state. Note the theoretical solution is not defined for y<0. These Si3D velocities are depth-averaged. Note that v is represented by solid lines and u by dashed lines.

Negatively Buoyant Point Source

In Figure A-16, Figure A-17, Figure A-19, and Figure A-19, we compare the Si3D predictions for a negatively buoyant point source to the Lee & Jirka (1980) solutions in the unstratified intermediate field, and to the combined Lee & Jirka and CORMIX II solutions in the stratified intermediate field. Examining Figure A-19, we see that predictions of back entrainment (Q at y=0) by the model are excellent, and that also the entrainment rate (and thus the dilution rate) in the first portion of the intermediate field is a

good match to the theoretical solutions. The Si3D solutions deviate significantly from the CORMIX II solutions, however, once stratification becomes important. We see that while CORMIX II predicts the continued slow development of a Gaussian plume, with subtle effects of buoyancy, we see the sudden radial spreading of the plume within Si3D once buoyancy becomes significant, and we see the bifurcation of the line of maximum temperature to either side of x=0. Since there are few empirical results to serve as a basis for the CORMIX II solutions in the stratified intermediate field, and since Si3D solves a realistic set of equations to account for the effects of buoyancy, we are inclined to trust the Si3D solutions over the CORMIX II solutions. Note that since spreading is largely radial, the solution is not sensitive to the value of A_h in this region, and is instead dominated by other terms in the governing equations which do not need to be altered artificially as we have altered A_h within the unstratified intermediate field.

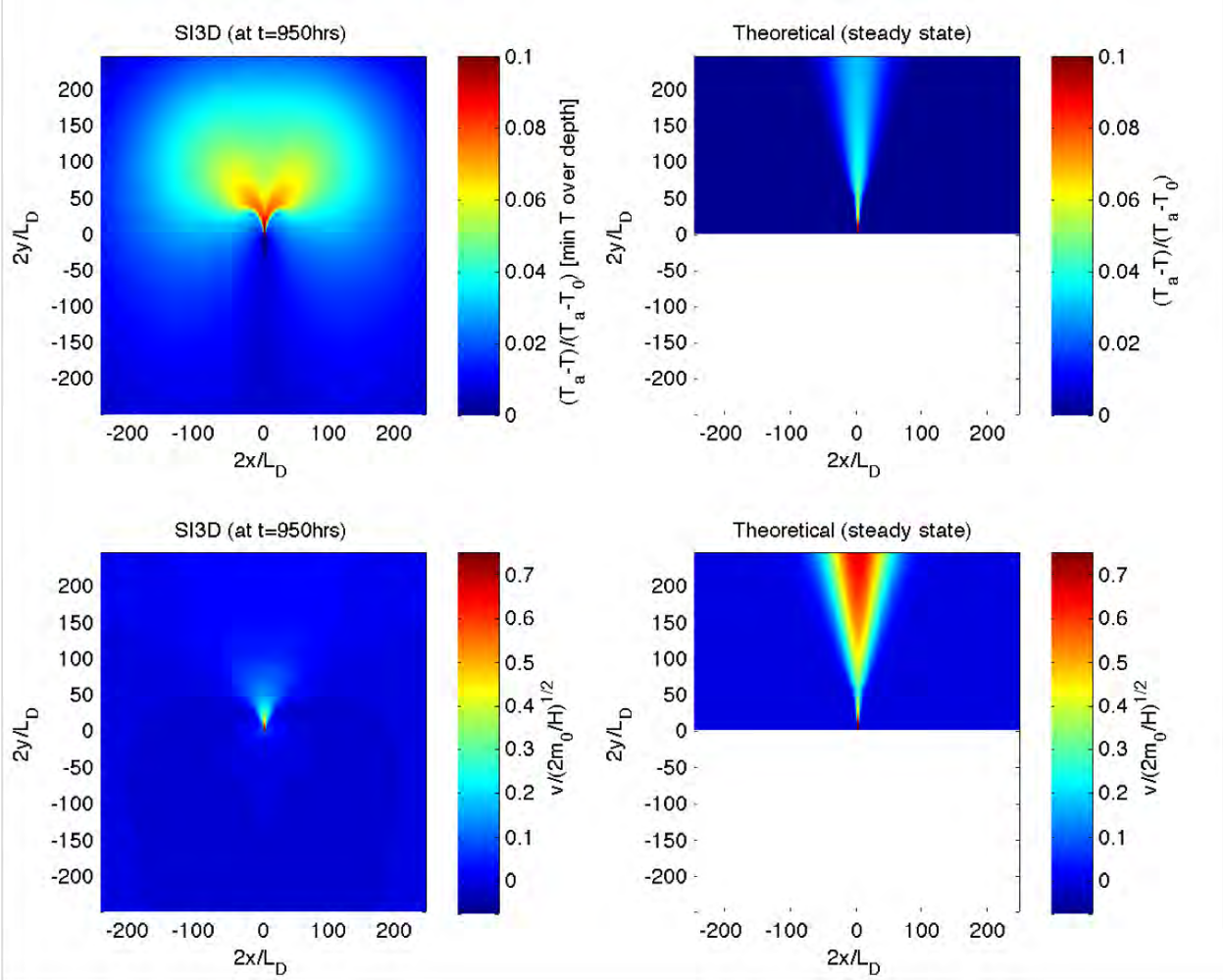

Figure A-16. Comparison of Si3D to Lee & Jirka (1980) (theoretical) solutions for u and v for a negatively buoyant discharge at steady state. Note the theoretical solution is not defined for y<0. These Si3D velocities are maximum values over the depth, and the Si3D temperatures are minimum values over the depth.

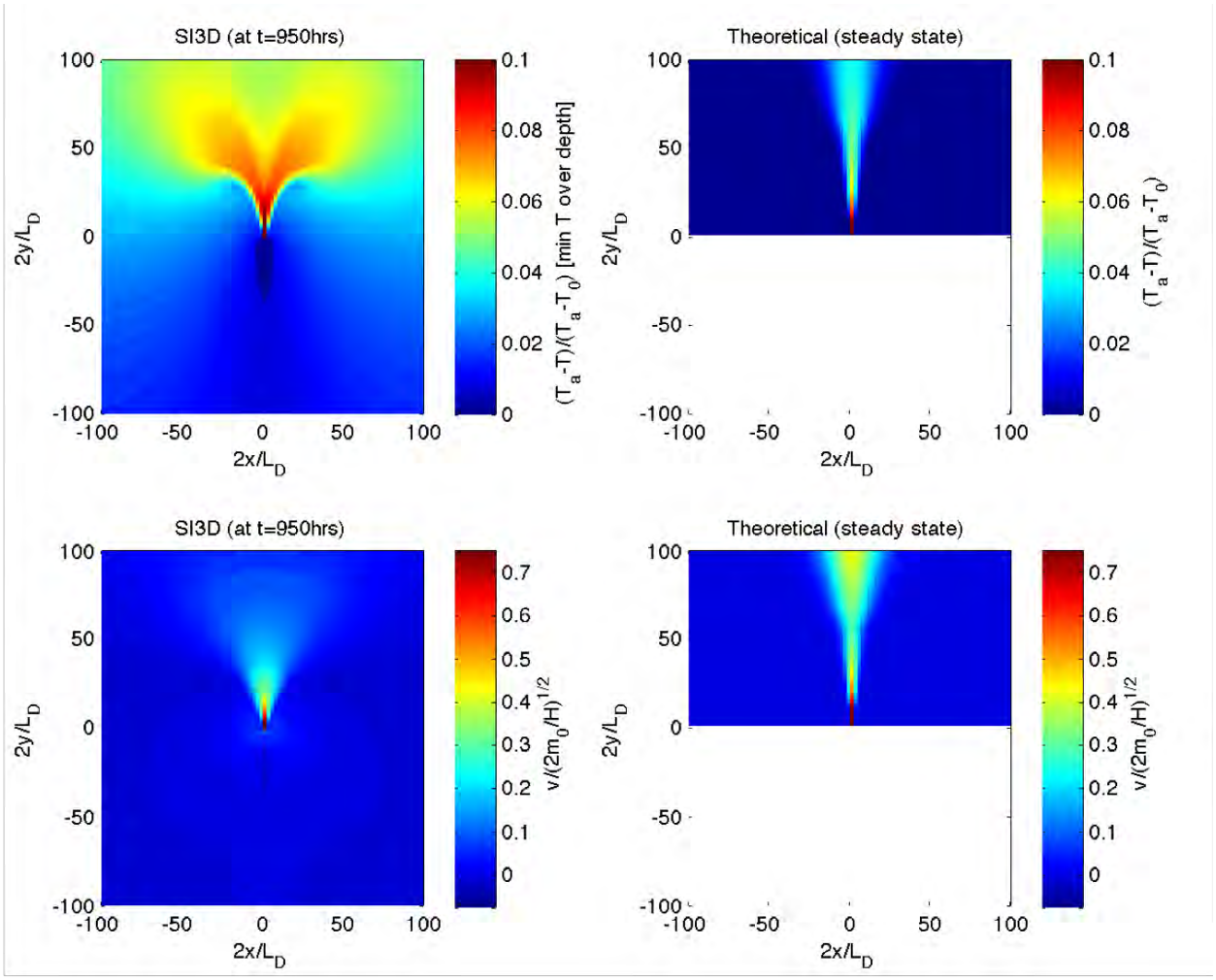

Figure A-17. Same as Figure A-16 but zoomed in.

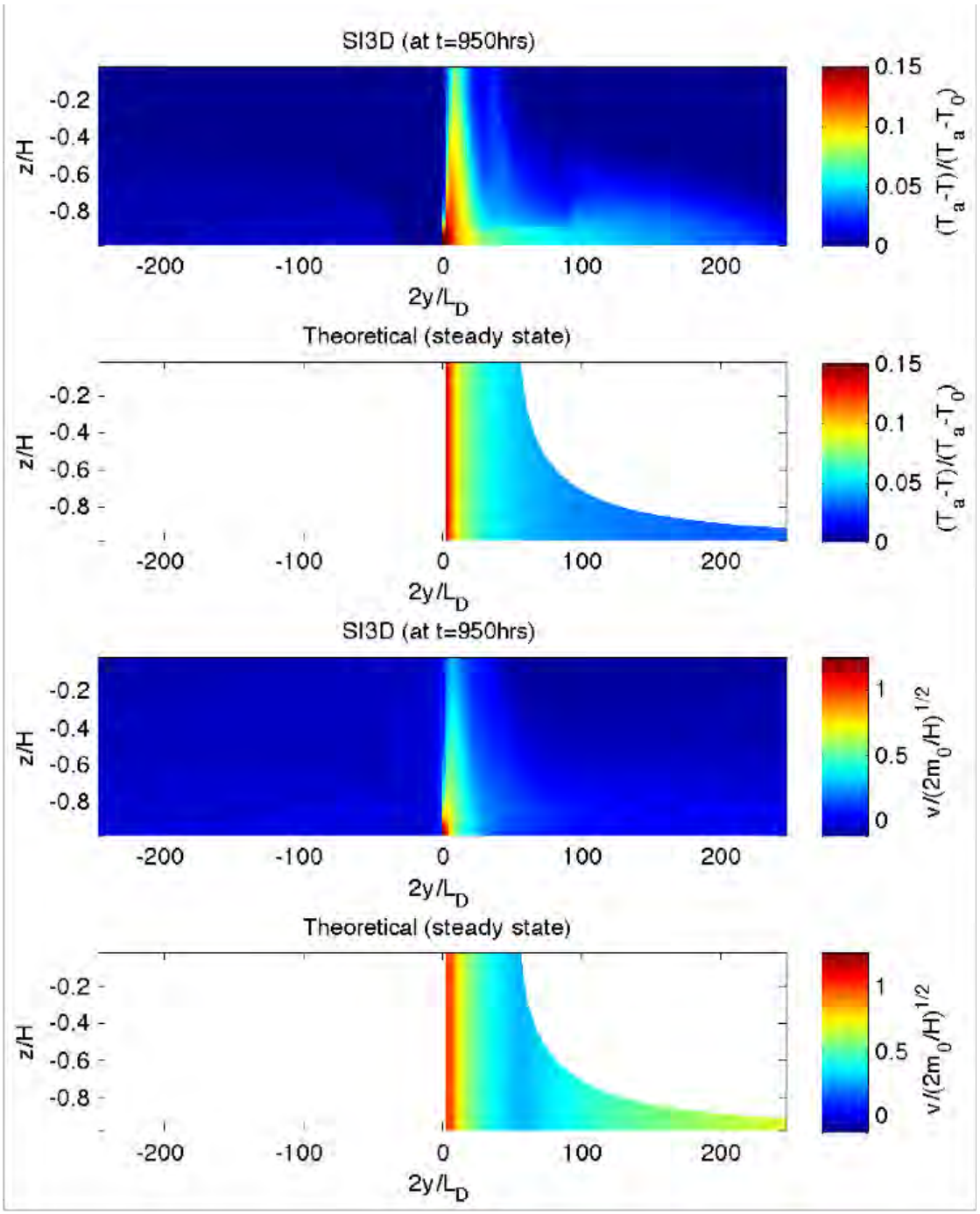

Figure A-18. Comparison of Si3D to Lee & Jirka (1980) (theoretical) solutions for v at x=0 for a negatively buoyant discharge at steady state. Note the theoretical solution is not defined for y<0.

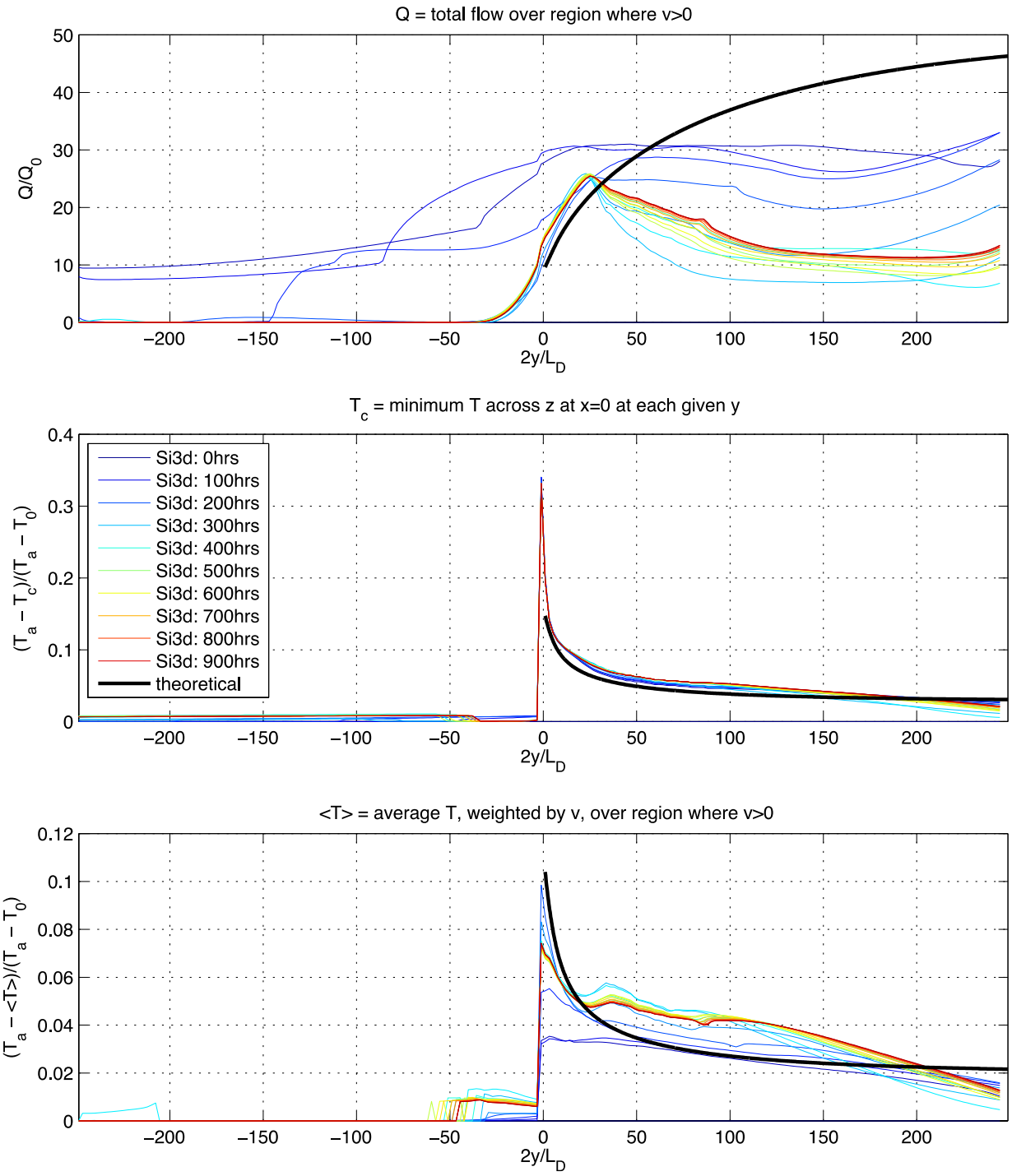

Figure A-19. Comparison of Si3D to Lee & Jirka (1980) (theoretical) solution for two definitions of bulk dilution (top and bottom panels) and one definition of centerline dilution (center panel) for a negatively buoyant discharge. Note the theoretical solution is not defined for y<0. The flow rate within Si3D at location y is evaluated by integrating all positive v across x and z. T_c is the temperature at x=0, and <T> is the integral across x and y of all temperatures located where v>0. Solutions are shown at different times to illustrate the approach to steady state.

In summary, we have developed and tested a point source model within Si3D that provides excellent predictions of back-entrainment induced by the LSC outfall, and by modifying horizontal eddy viscosity and diffusivity in the vicinity of the outfall, we are able to accurately reproduce theoretical solutions for side-entrainment in the unstratified intermediate field. For negatively buoyant plumes, our solutions within the stratified intermediate field differ significantly from the empirical solutions embedded within CORMIX II, but since the empirical solutions within CORMIX II are based on very little data, we better trust our model solutions in this region. The most important effect of the LSC outfall on the shelf, by far, is back entrainment, as this is the quantity that sets up a large-scale recirculation zone which is the only process flushing the shelf in the absence of tributary flow and winds. Hence we are satisfied with our point source model. The final step in development of the point source model is calibration using field data from Cayuga Lake, which is described in Section **A.4.4**

A.4.3 Boundary Conditions and Initial Conditions

In this section we describe development of the initial conditions and boundary conditions used to drive the Si3D simulations of Cayuga Lake.

A.4.3.1 Numerical Grid

The numerical grid defines the locations where velocities, temperatures, and tracer concentrations are evaluated by the numerical model. Si3D employs a staggered Cartesian grid, meaning the cells are rectangular prisms, fluxes are computed at cell faces, and scalar quantities are evaluated at the center of each cell.

To resolve the lateral mixing, back entrainment, and resulting circulation on the shelf caused by the LSC outfall as well as the tributary inflows, we determined (as described in Section **Downstream of** the LSC outfall point source within Si3D, we set the horizontal eddy viscosity and the horizontal eddy diffusivity equal to the values derived in this section, using the values of u_c, b_h, and δ derived by Lee and Jirka (1980), the goal being to obtain the plume behavior predicted by Lee and Jirka in the unstratified intermediate field. The back-entrainment and behavior within the acceleration zone should be determined by the momentum equations already solved by Si3D. And we do not explicitly add the behavior of the stratified intermediate field. We use a turbulent Schmidt number of one, i.e. turbulent eddy viscosity and turbulent eddy diffusivity are equal, and for simplicity we assume $\alpha_1 = \alpha_2$ and $\lambda = 1$.

A.4.2.) that a resolution of 25m x 25m is required in the horizontal plane, and a resolution of 0.1m is required in the vertical direction. This fine resolution is not computationally feasible for the entire lake, and so we use a nested gridding scheme. The entire lake is modeled using a 125m x 125m grid, and the shallow southern shelf is modeled in greater detail using a 25m x 25m grid. The 125m x 125m grid is called the “outer”, “coarse”, “low resolution” or “LR” grid, and the 25m x 25m grid is called the “inner”, “fine”, “high resolution”, or “HR” grid. The LR simulations are run first, and then the HR simulations are run using the LR results as input: the boundary conditions at the open boundary located along the north

end of the HR grid are specified using the predictions of the LR simulations at the location of that boundary. Details of the numerical implementation are documented in Acosta et al. (2015).

To develop the LR and HR grids, we began with bathymetric measurements described in Section **A.2.1**. We rotated the (x,y) coordinates of the bathymetric data 26^{o} clockwise within the horizontal plane so the LSC discharge is directed to the "north" within the numerical model, aligning with the grid cell boundaries – this minimizes numerical diffusion error. The tributaries were straightened and in some cases flipped from east to west, also to minimize numerical diffusion, however, we took care within the HR mesh to preserve the tributary angle at the mouth in order to correctly predict the angle of entry of stream inflows to the shelf.

After the rotations and other mappings described above, depth measurements were interpolated onto the horizontal coordinates of the LR and HR grid cell centers using the natural neighbor method (e.g., Vandebroek, 2011). The depths at the north end of the HR mesh were altered to match the LR mesh depths, with a linear transition over 375m.

We locate the upper boundary of the topmost layer of cells at an elevation 106.6m above the NGVD 1929 datum, a typical summer water surface elevation. Cell depth is uniform in the horizontal plane and the same for both grids. The top cell is 0.5m deep, to accommodate basin-scale surface waves, and cells are 0.1m deep between the top cell and 3.0m depth, to resolve the LSC outfall plume. Below 3.0m, the cell depths gradually increase towards a depth of 6.3m at the bottom. The depth to the top of each layer of cells (referenced to the top of the top-most cell) is plotted in Figure A-20.

The LR grid is shown in Figure A-21; and the HR grid is shown in Figure A-22 along with a schematic of how the two size grids are nested within the 3D model.

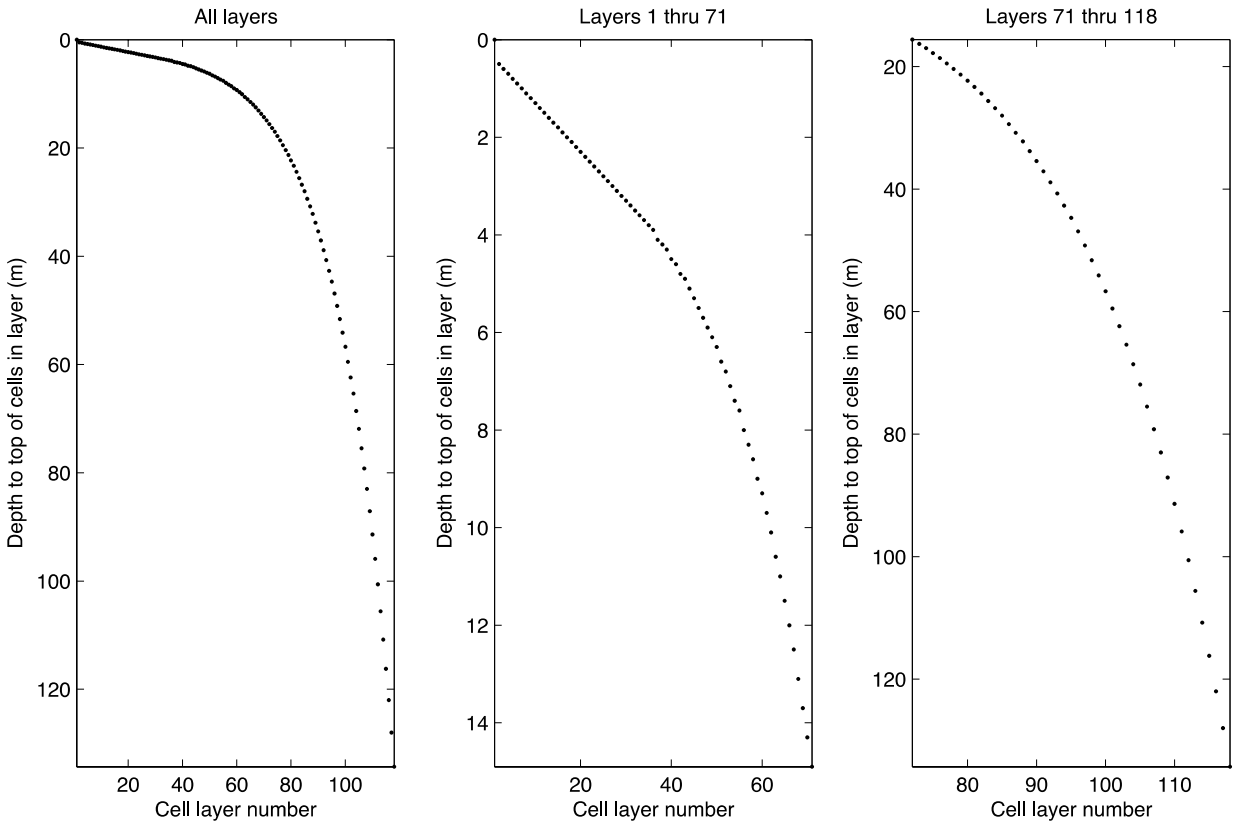

Figure A-20. Depth to the top of each layer of cells within the numerical grid. All layers are shown in the first panel. The second and third panels zoom in on the top 71 layers and the bottom 48 layers, respectively.

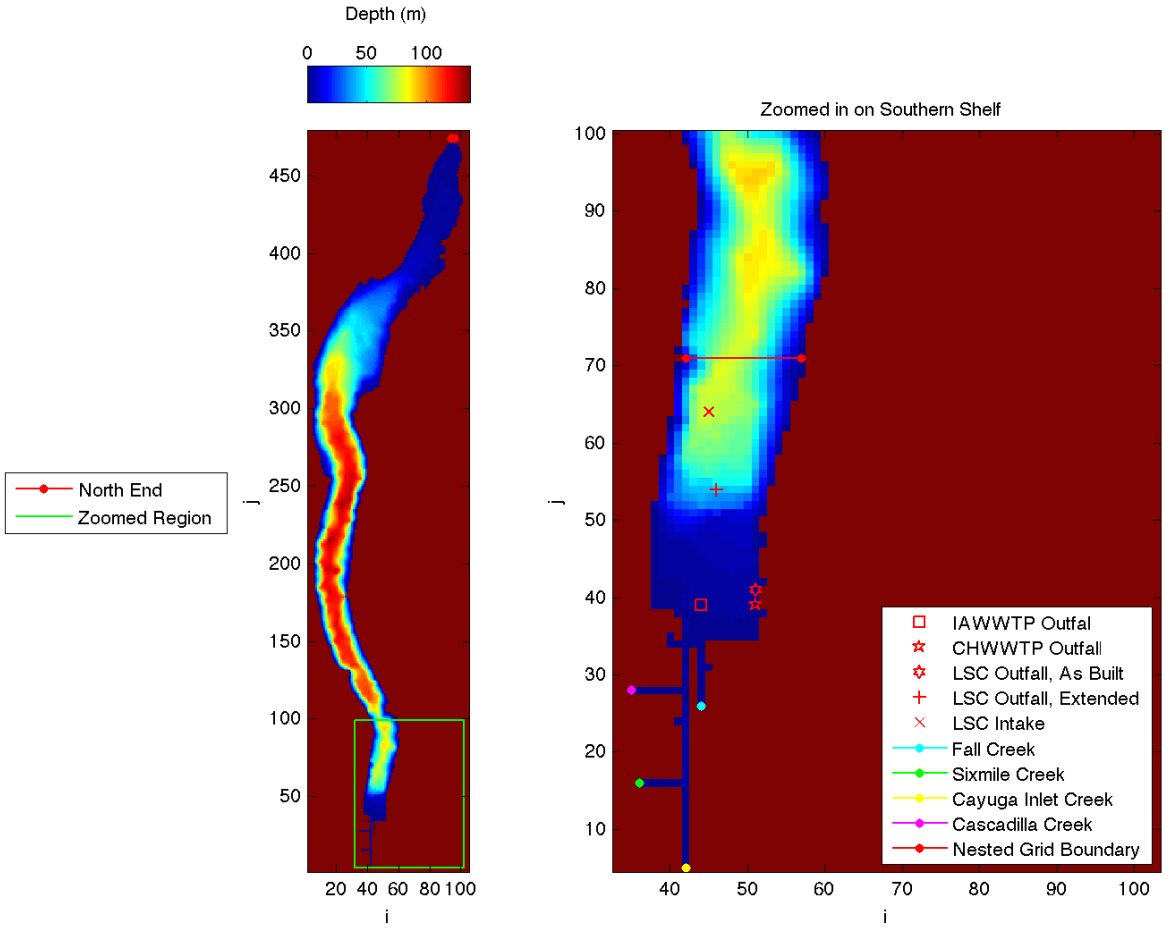

Figure A-21. LR (125m x 125m) grid. On the left is the entire grid, and on the right is a close-up of the southern portion. The indices i and j correspond to grid cell number, and color corresponds to depth. Also shown are the locations of the point source inputs, the locations of the four inflow boundaries at the tributaries, the location of the one water surface elevation boundary at the north end of the lake, and the location of the nested grid boundary, at which the LR simulation generates boundary conditions for the HR simulation.

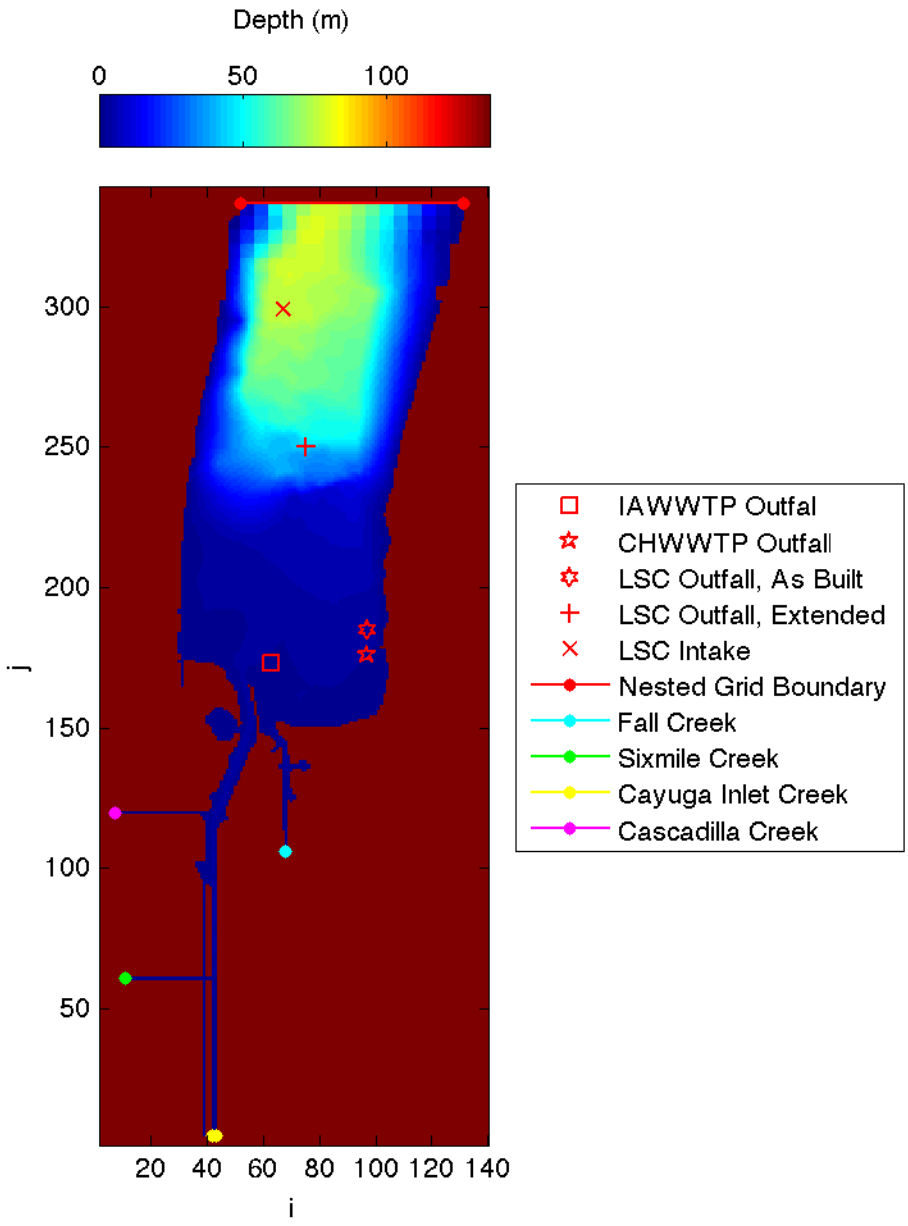

Figure A-22. HR (25m x 25m) grid. The indices i and j correspond to grid cell number, and color corresponds to depth. Also shown are the locations of the point source inputs, the locations of the four inflow boundaries at the tributaries, and the location of the nested grid boundary, at which the LR simulation generates boundary conditions for the HR simulation.

A.4.3.2 Free Surface Boundary Conditions

Our starting point is meteorological station measurements (including wind velocity, air temperature, shortwave radiation, relative humidity, and air pressure), near-surface water temperatures measured at the piling cluster, and light extinction coefficients measured by UFI or estimated from Secchi depth

measurements. The surface boundary conditions required by Si3D include the following: the light attenuation coefficient (K_d), the penetrative component of the heat flux, with the albedo already taken into account ($H_{sw,as}$), the atmospheric pressure (P_a), the relative humidity (RH), percent cloud cover (CC), the wind drag coefficient based on wind speed at 10m above the water surface (C_{10}), and the wind velocity components at 10m above the water surface (U_{10},V_{10}). Since the piling cluster anemometer is located 8m above the water surface, we correct wind speeds to 10m using a 1/7th power-law formula

$$U_{10} = \left(\frac{10}{8}\right)^{1/7} U$$
$$V_{10} = \left(\frac{10}{8}\right)^{1/7} V \qquad (51)$$

where U and V are the wind velocity components measured at the piling cluster. These components are also rotated 26^{o} counterclockwise to align with the numerical grid. Wind drag coefficient is estimated using the method of Amorocho and DeVries (1980). Components of the heat flux are estimated using methods found in Chapra (2008). Cloud cover is estimated from the difference between measured shortwave radiation and expected shortwave radiation for a clear day given the location of Cayuga Lake and time of year.

A.4.3.3 Inflow and Water Surface Boundary Conditions

Water level measured in the Cayuga Inlet by the USGS as described in Section **A.2.5** is filtered using a 6-hour rolling average, and then specified as the northern boundary condition for the LR simulations. Even during persistent strong wind events, the difference in the 6-hour average water surface elevation between Cayuga Inlet and the northernmost end of the lake rarely exceeds 10cm, so the water surface elevation measured at Cayuga Inlet is a reasonable representation of water surface elevation across the entire lake. Specifying the water surface elevation as a model boundary condition ensures the correct mass balance over longer time-scale variations in water surface elevation that are controlled at the lake outlet at the north end.

At the tributaries (Fall Creek, Sixmile Creek, Cayuga Inlet Creek, and Cascadilla Creek), we specify inflow open boundary conditions, providing flow rate and water temperature data from sources described in Section **A.2.6**.

A.4.3.4 Nested Grid Boundary Condition

Within the LR simulation, we output fluxes at the nested grid open boundary (refer to Figure A-21) to provide open boundary conditions within the HR simulation. Recall that the location of the nested grid boundary within the HR simulation is shown in Figure A-22.

A.4.3.5 Initial Conditions

Si3D is initialized with zero velocity everywhere and temperature specified as a function of depth alone. We used the temperature profiles measured by the thermistor chains near the LSC intake to generate initial conditions for Si3D. It requires some care to obtain a temperature profile that is representative of the entire lake from a vertical profile measured at a single spatial location subject to internal wave

activity (i.e., the thermistor chain location). The internal wave period depends on stratification conditions and is typically around 2.5 days in mid-summer. To obtain a lake-wide temperature profile from the thermistor string data, we first averaged the profile over a short time scale (1 hour) to smooth oscillations due to small waves and turbulence. Then we locate the thermocline, defined in Equation (1), as a function of time. We re-center the profile at the thermocline and then take a time-average of temperature at each height (relative to the thermocline) over five days to average over the internal waves. We also take a 5-day time-average of thermocline depth and add the averaged thermocline depth back to the depth axis. Finally, we obtain the initial condition for lake temperature from the averaged time history of the temperature profile at the appropriate time. This method allows us to average over internal waves while maintaining the correct temperature gradient at the thermocline.

A.4.4 Calibration of Point Source Model Using 2014 Gridding Data

To calibrate the point source model, we simulated the lake using 2014 drivers, and using different calibration coefficients, and compared Si3D predictions to measurements collected during the 2014 gridding study to optimize the calibration coefficients. Model initial conditions and boundary conditions for the calibration simulation are the same as for the 2014 validation study, and can be found in **A.4.5.1**. Calibration coefficients include the bottom drag coefficient, C_D, the background horizontal eddy viscosity/diffusivity, A_{H0}, and the entrainment coefficient for the intermediate field, $\alpha_1 = \alpha_2$. We ran simulations using the 26 sets of these calibrations shown in Table A-4. We found that Run 6 (highlighted) produced the smallest root mean square error (RMSE) averaged quadratically over all of the SCAMP and Seabird profiles (as displayed in Figure A-23), and so we use the run 6 values of the calibration coefficients for the validation and residence time studies described in the following sections.

Table A-4. Calibration coefficients tested against 2014 gridding study simulation.

Run Number	C_D	$A_{H,0}$	α_1, α_2
1	0.001	0.01	0.008
2	0.001	0.01	0.08
3	0.001	0.01	0.8
4	0.001	0.1	0.008
5	0.001	0.1	0.8
6	0.001	1.0	0.008
7	0.001	1.0	0.08
8	0.001	1.0	0.8
9	0.002	0.01	0.008
10	0.002	0.01	0.08
11	0.002	0.01	0.8
12	0.002	0.1	0.008
13	0.002	0.1	0.08
14	0.002	0.1	0.8
15	0.002	1.0	0.008
16	0.002	1.0	0.08
17	0.002	1.0	0.8
18	0.003	0.01	0.008

19	0.003	0.01	0.08
20	0.003	0.01	0.8
21	0.003	0.1	0.008
22	0.003	0.1	0.08
23	0.003	0.1	0.8
24	0.003	1.0	0.008
25	0.003	1.0	0.08
26	0.003	1.0	0.8

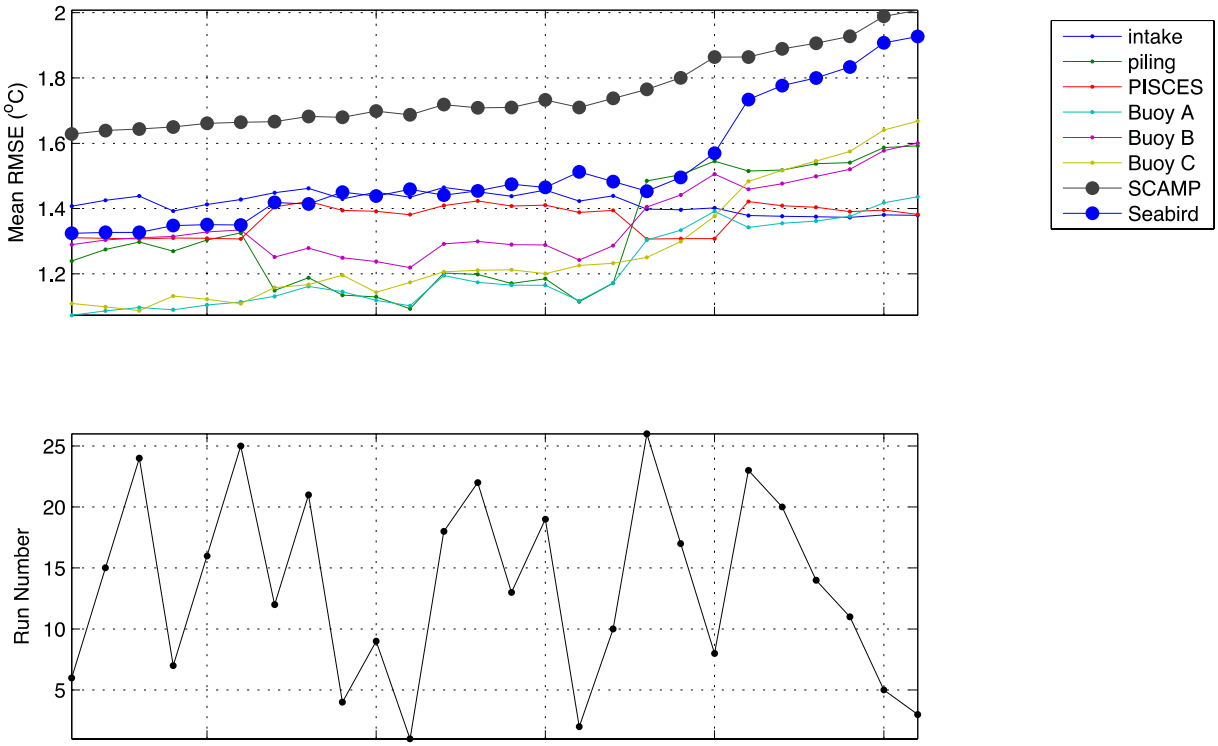

Figure A-23. Here for each calibration run tabulated in Table A-4, we plot the total RMSE over the duration of the gridding study (August 15, 6:00 through August 16, 18:00) for the moored thermistors (the LSC intake – this RMSE is a depth average, the piling cluster, the PISCES, Buoy A, Buoy B, and Buoy C), and also for the SCAMP and Seabird profiles. For the transects we take the average RMSE over depth for each transect, and then across all transects. All averages of RMSE are quadratic (i.e. the square root of the sum of the mean square errors). We sort the runs from lowest to highest Seabird/SCAMP profile RMSE, i.e., the quadratic average of the SCAMP RMSE and the Seabird RMSE. The lower panel shows the run numbers in order from smallest profile RMSE to largest profile RMSE, and the RMSE's in the top panel correspond to the runs in the lower panel. Run 6 has the smallest RMSE based on the SCAMP/Seabird profiles.

A.4.5 Validation of 3D Model Based on 2012, 2013, 2014 Data

To validate the calibrated model, we ran 37-day long simulations driven by field measurements in 2012, 2013, and 2014. The simulations were given 7 days to ramp up. We compared measured to modeled temperatures in the final 30 days of the simulations for the thermistors at the intake and piling cluster.

A.4.5.1 Model Inputs for the Validation Studies

Model initial conditions and boundary conditions for the validation studies were obtained as described in Section

A.4.3 . Initial conditions for the 2012, 2013, and 2014 validation studies are shown in Figure A-24, Figure A-25, Figure A-26, and Figure A-27.

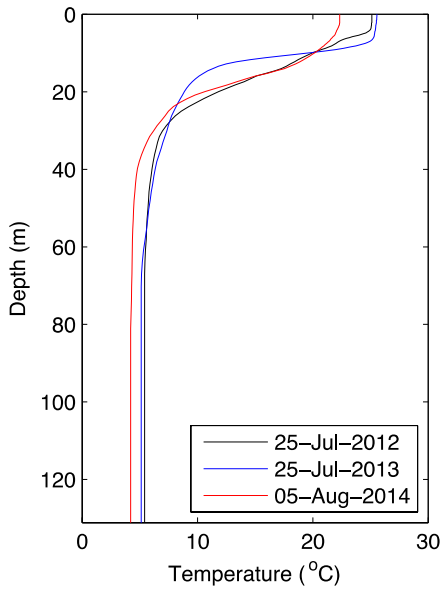

Figure A-24. Initial conditions for validation studies. The 2013 profile is used to initialize the residence time simulations as well.

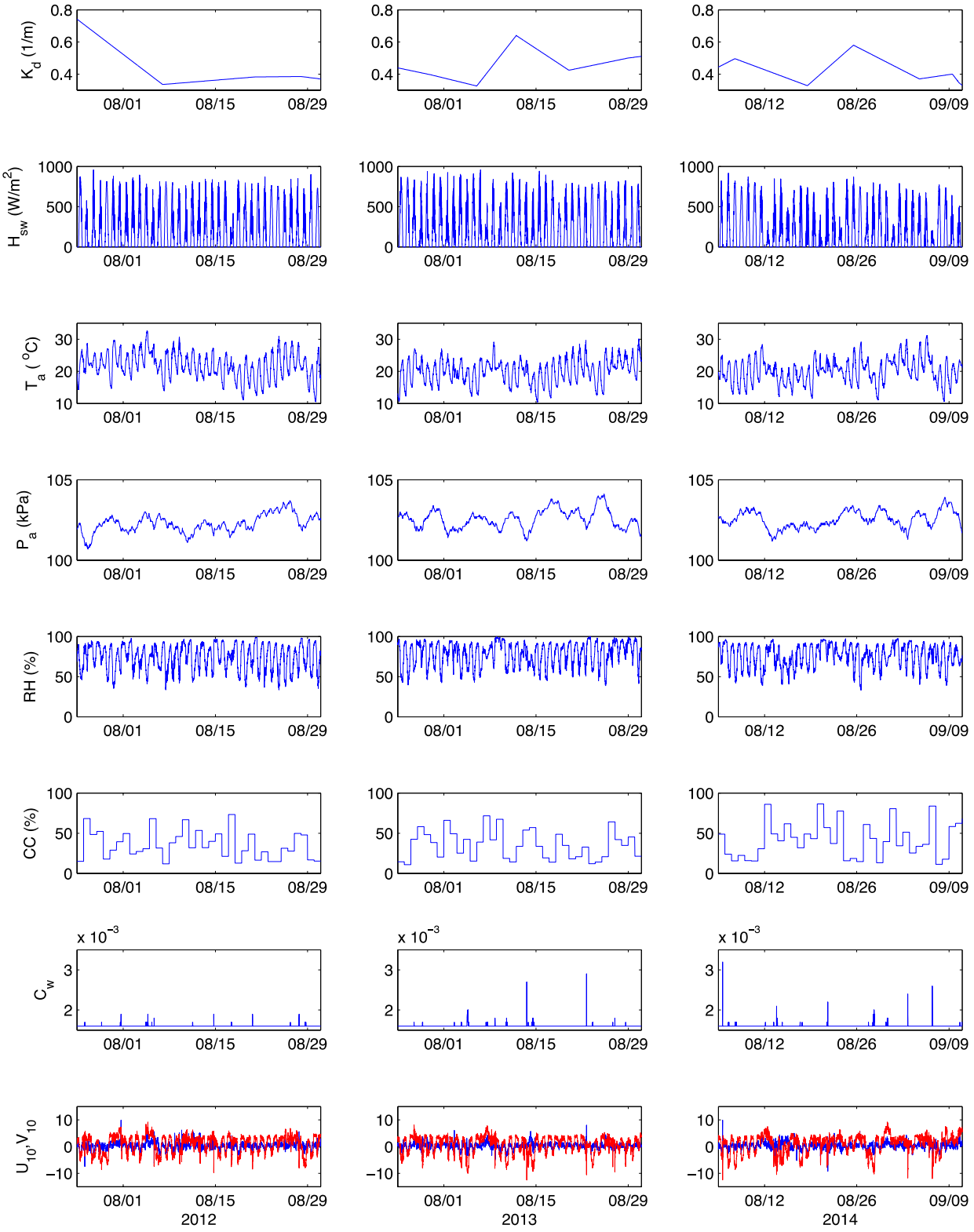

Figure A-25. Surface boundary conditions for validation studies.

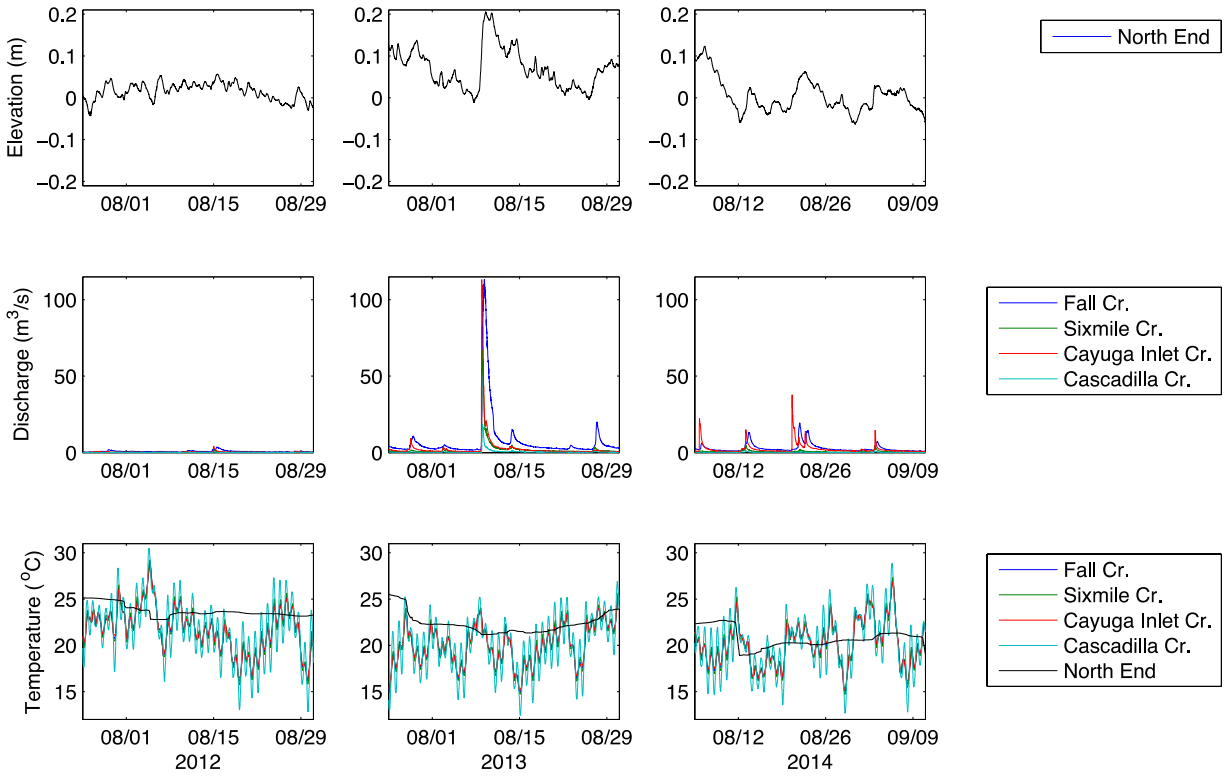

Figure A-26. Open boundary conditions for validation studies. Note the tributary discharge in 2012 was so small as to be almost invisible here.

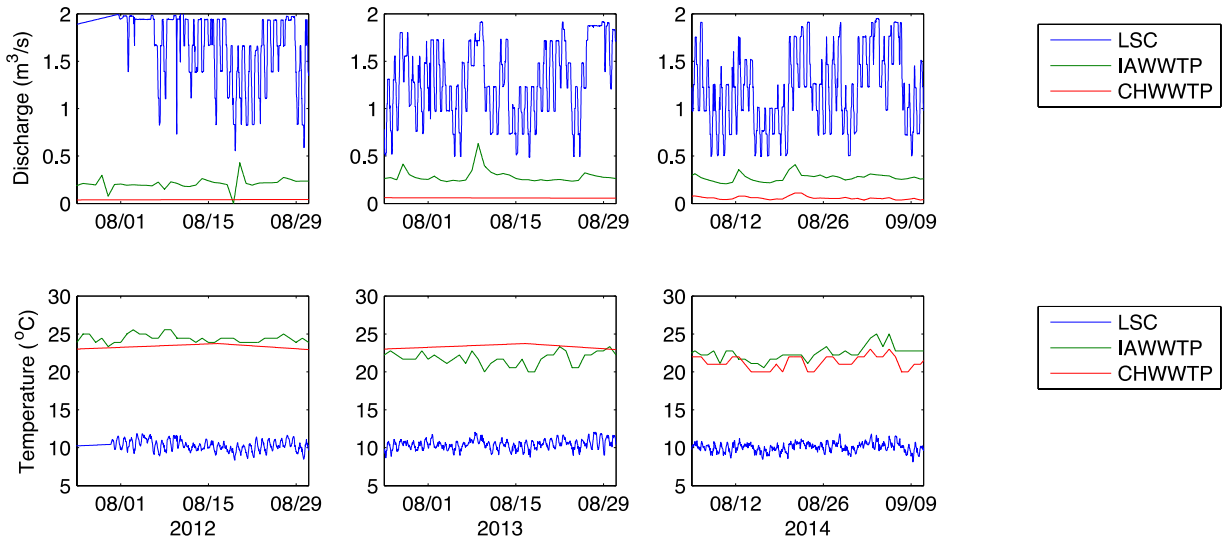

Figure A-27. Point source input for validation studies.

A.4.5.2 Results of Validation Studies

Here we present and evaluate the results of the 2012, 2013, and 2014 validation studies. Note that these results are from the LR simulations and should be considered provisional. Final HR results will be provided in a supplemental report.

In Figure A-28, Figure A-29, and Figure A-30 we compare temperatures measured by the thermistor chains near the LSC intake to temperatures predicted by Si3D at the same location in the validation simulations. We see that internal wave period is predicted very accurately, and internal wave phase and amplitude are decently predicted as well. At each thermistor depth, we compute a 2-day running quadratic average of RMSE, plotting the time history in the same figures as the temperature profiles. This RMSE remains below 2^{o}C except near the thermocline, where it may spike as high as 5^{o}C, but typically remains below 3^{o}C. RMSE at each thermistor depth, averaged quadratically over the 30-day duration of the validation period, is shown in Figure A-31. Here we see that RMSE spikes at the thermocline and remains below 3^{o}C over all elevations. These RMSE are comparable to those found by Gelda et al. (2015).

In Figure A-32, Figure A-33, and Figure A-34 we compare measured and modeled thermocline depth at the LSC intake thermistor chain. Taking a 2-day running quadratic average RMSE to compare measured and modeled thermocline depth, we find it does not exceed 3.3m except during an upwelling event early in the 2014 experiment.

In Figure A-35, Figure A-36, and Figure A-37 we show measured and modeled water temperatures at the piling cluster, and compare using a 2-day rolling quadratic average RMSE. Here we also compare depth-averaged temperature from the LSC intake thermistor chain. We see that RMSE never exceeds 3^{o}C for either.

In Table A-5 we show RMSE, averaged quadratically over the entire 30-day duration of each validation period, for piling cluster temperature, depth-averaged near-intake temperature, and near-intake thermocline depth.

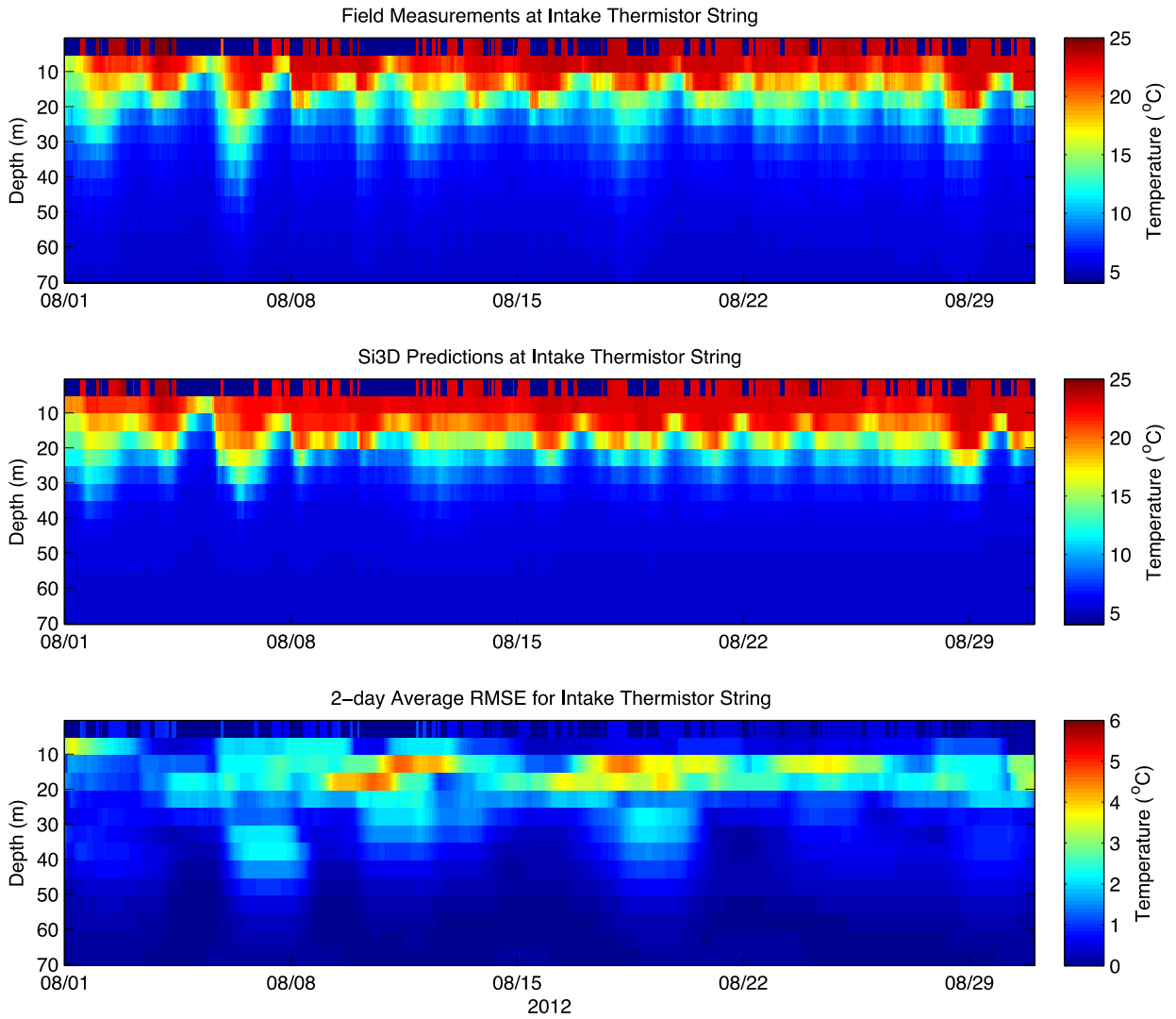

Figure A-28. Comparison of field measurements and model predictions at thermistor string near LSC intake for 2012 validation study. The top panel temperature as a function of depth and time measured by the thermistor chain near the LSC intake. The middle panel shows the model predictions of those temperatures. The bottom panel shows a 2-day running average of the root mean square error, comparing measured to modeled temperatures for each thermistor on the chain.

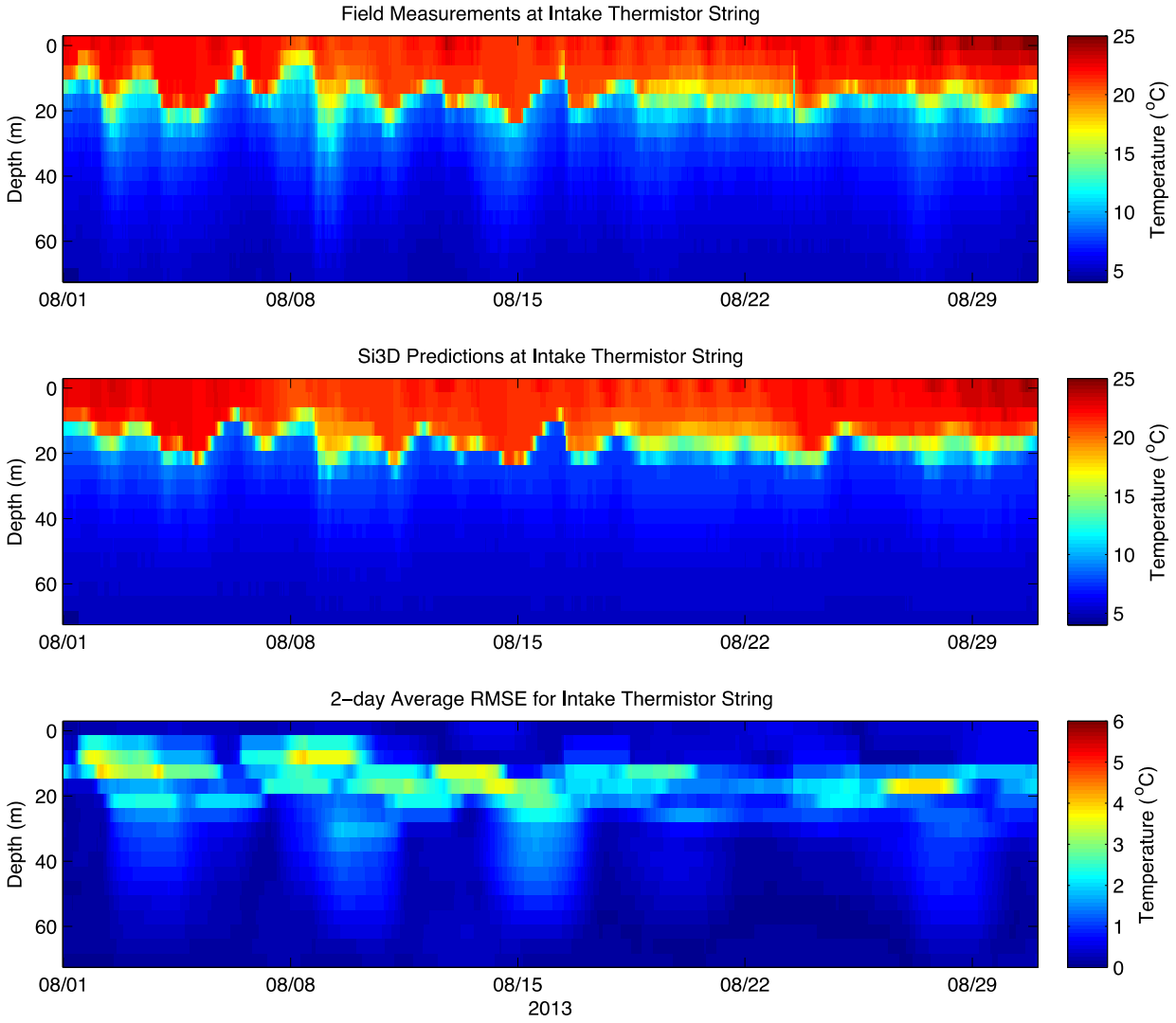

Figure A-29. Comparison of field measurements and model predictions at thermistor string near LSC intake for 2013 validation study. The top panel temperature as a function of depth and time measured by the thermistor chain near the LSC intake. The middle panel shows the model predictions of those temperatures. The bottom panel shows a 2-day running average of the root mean square error, comparing measured to modeled temperatures for each thermistor on the chain.

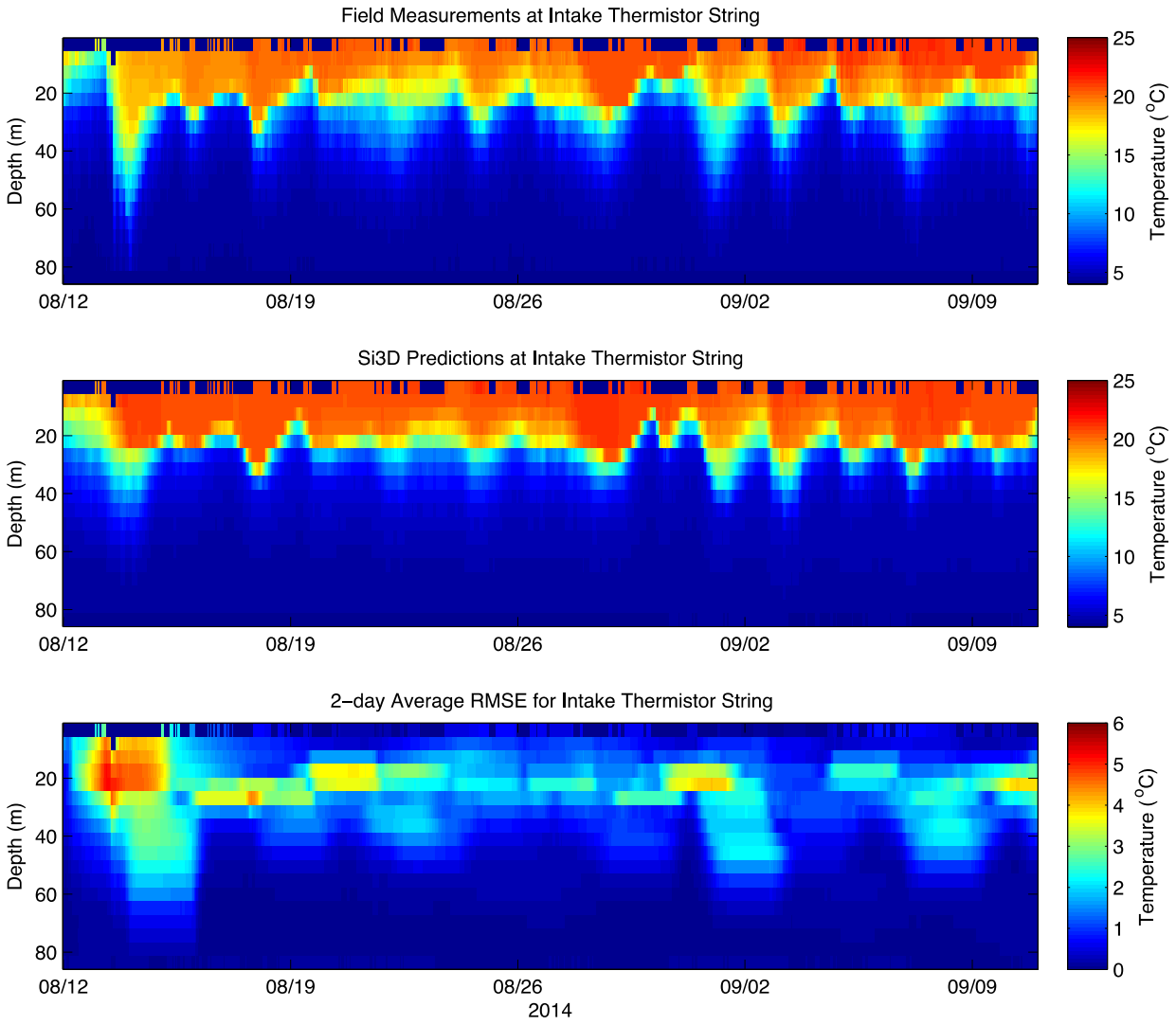

Figure A-30. Comparison of field measurements and model predictions at thermistor string near LSC intake for 2014 validation study. The top panel temperature as a function of depth and time measured by the thermistor chain near the LSC intake. The middle panel shows the model predictions of those temperatures. The bottom panel shows a 2-day running average of the root mean square error, comparing measured to modeled temperatures for each thermistor on the chain.

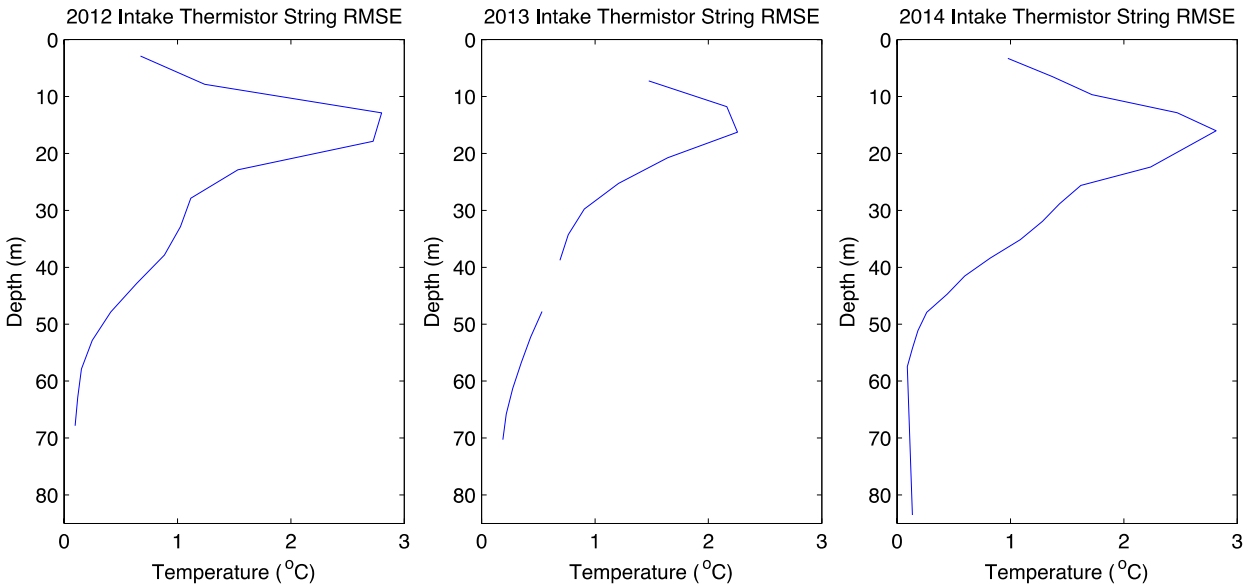

Figure A-31. Root mean square error in temperature, averaged over duration of the validation studies, comparing field measurements to model predictions at thermistor string near LSC intake.

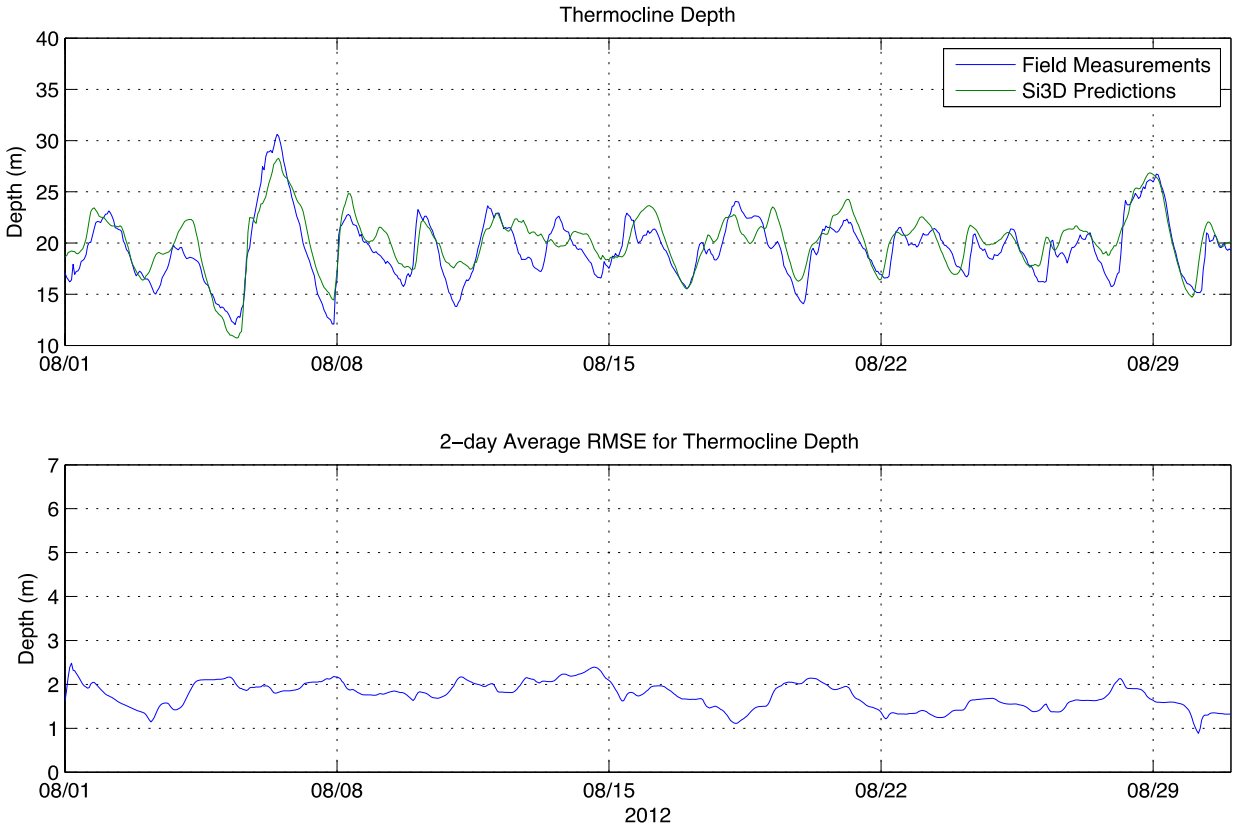

Figure A-32. Thermocline depth calculated from thermistor chain data near LSC intake. Here we compare the thermocline depth calculated from field measurements to the thermocline depth calculated from

model predictions in the 2012 validation study. In the lower panel we plot the 2-day running average of the root mean square error comparing measured and modeled thermocline depths.

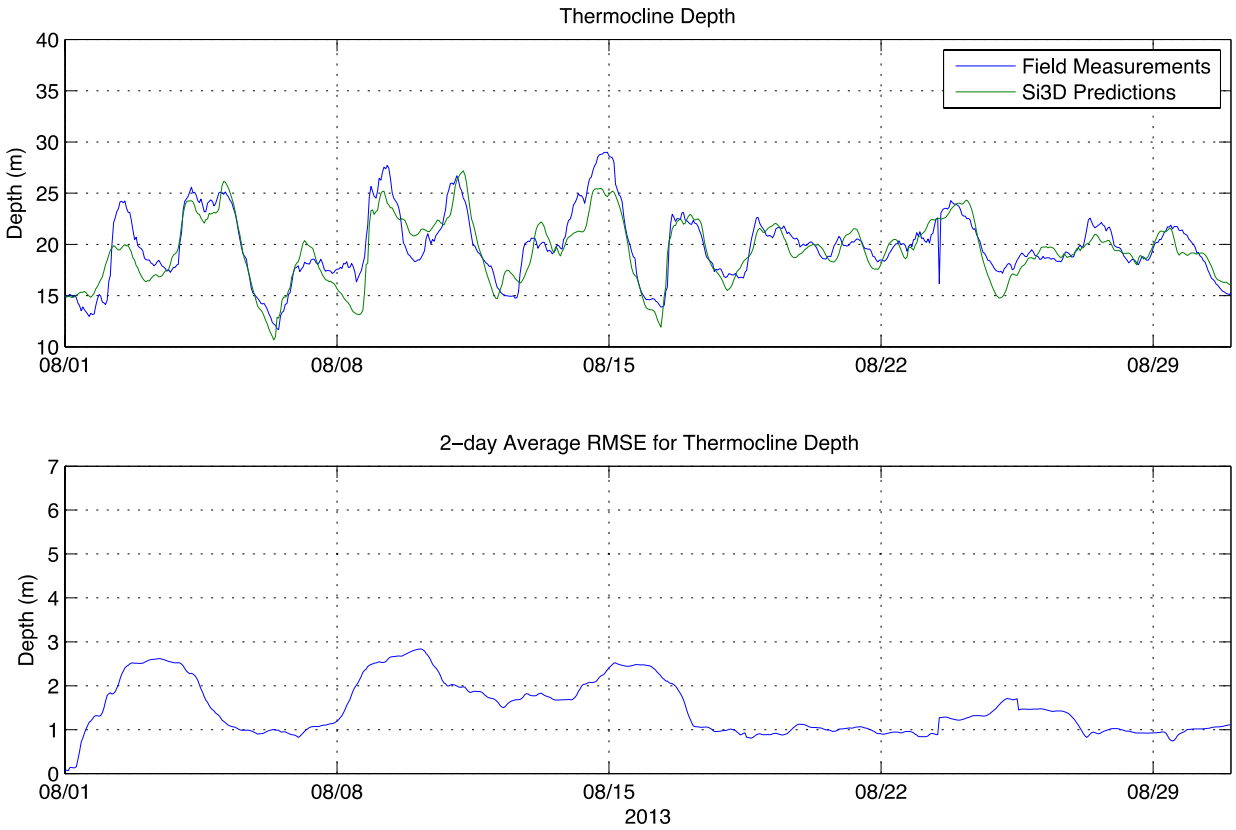

Figure A-33. Thermocline depth calculated from thermistor chain data near LSC intake. Here we compare the thermocline depth calculated from field measurements to the thermocline depth calculated from model predictions in the 2013 validation study. In the lower panel we plot the 2-day running average of the root mean square error comparing measured and modeled thermocline depths.

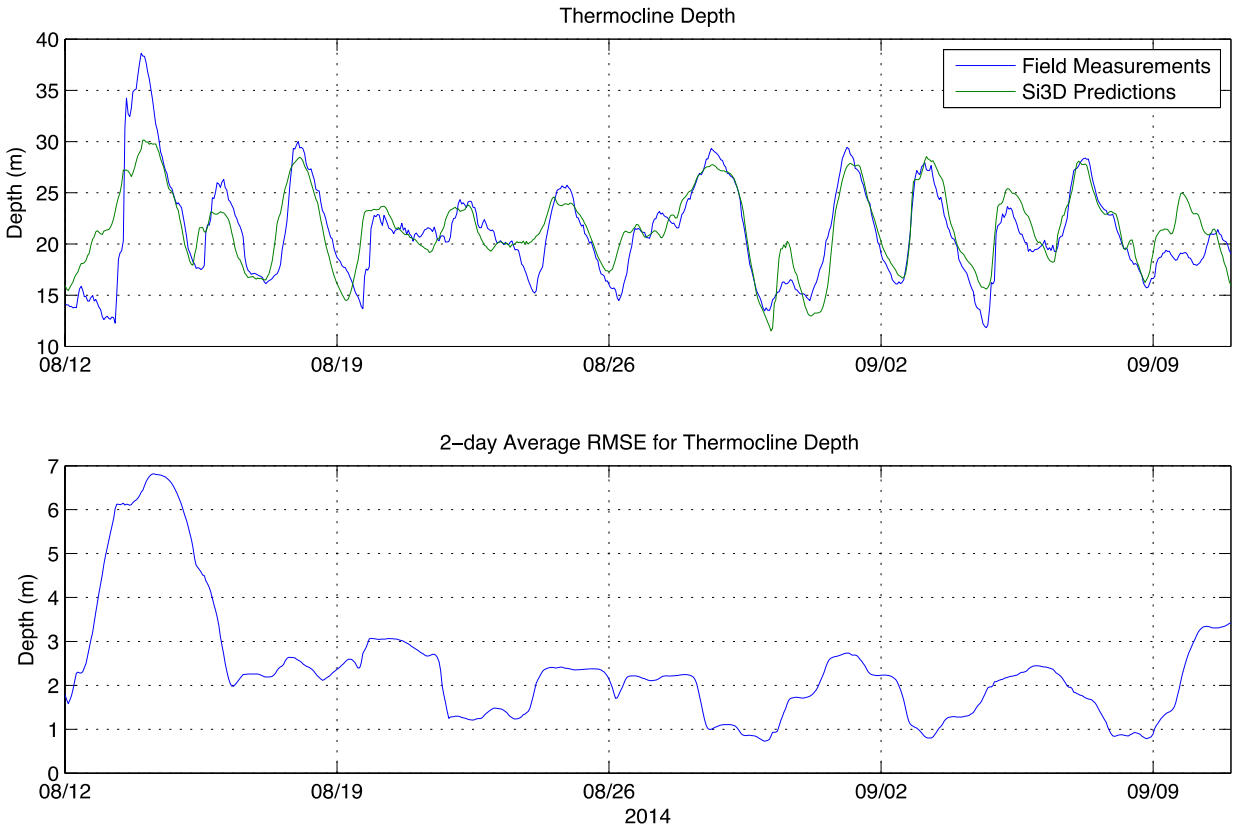

Figure A-34. Thermocline depth calculated from thermistor chain data near LSC intake. Here we compare the thermocline depth calculated from field measurements to the thermocline depth calculated from model predictions in the 2014 validation study. In the lower panel we plot the 2-day running average of the root mean square error comparing measured and modeled thermocline depths.

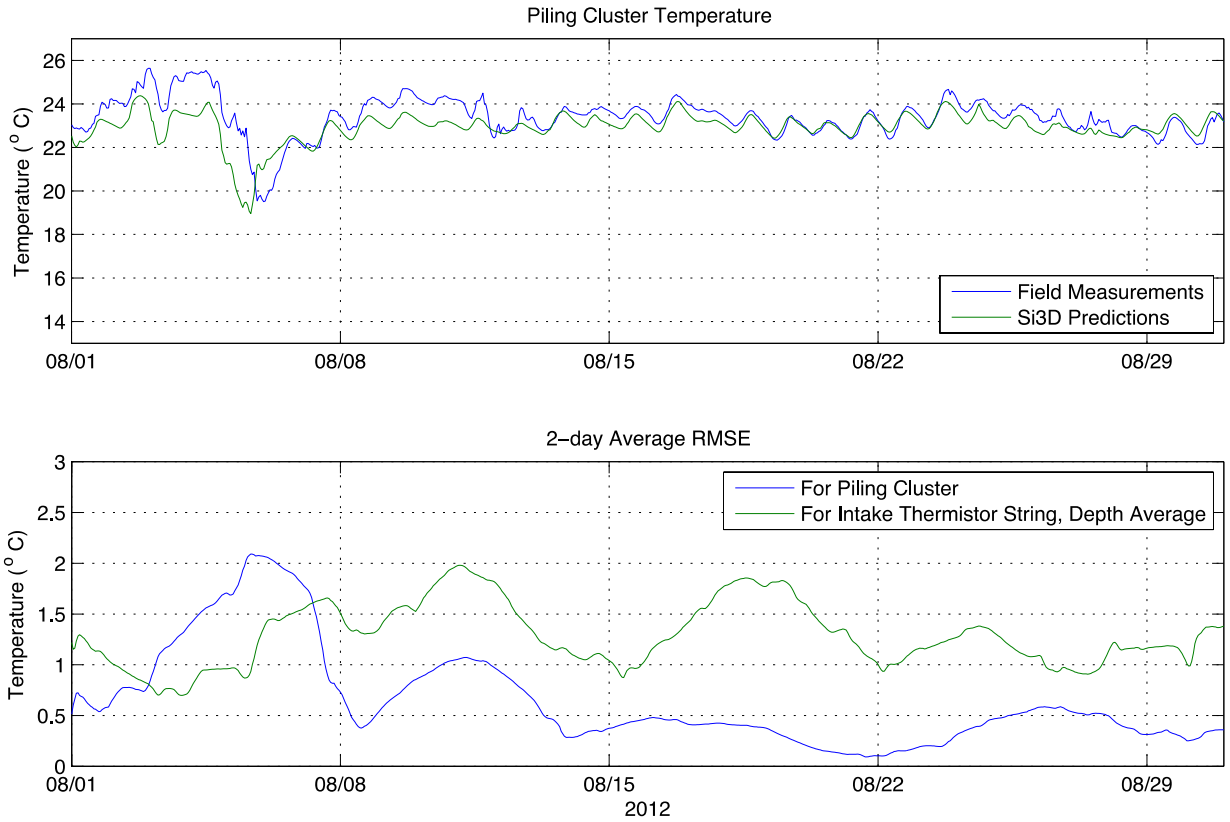

Figure A-35. The top panel compares field measurements and model predictions of water temperature at the piling cluster for the 2012 validation study. The bottom panel shows a 2-day running average of the root mean square error, comparing measured to modeled temperatures at the piling cluster, and also shows the depth average of the 2-day running average root mean square error for the intake thermistor string.

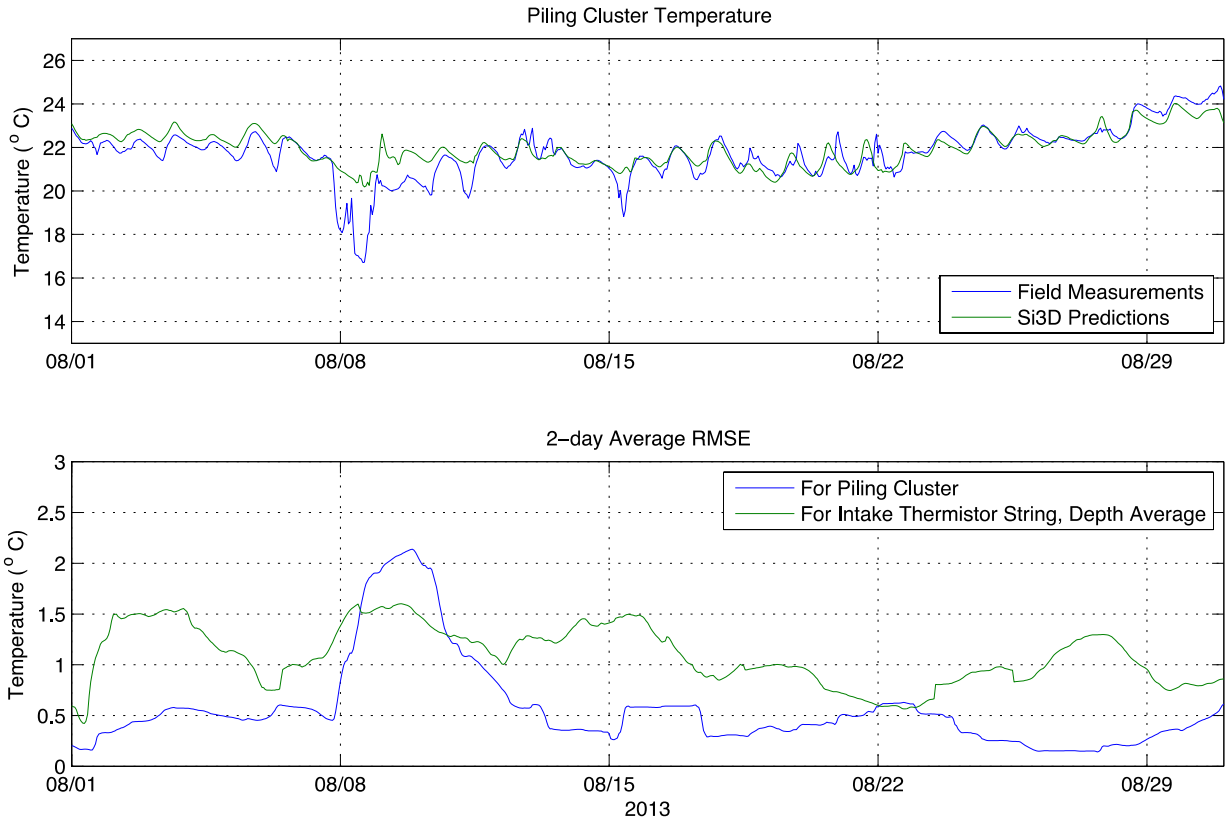

Figure A-36. The top panel compares field measurements and model predictions of water temperature at the piling cluster for the 2013 validation study. The bottom panel shows a 2-day running average of the root mean square error, comparing measured to modeled temperatures at the piling cluster, and also shows the depth average of the 2-day running average root mean square error for the intake thermistor string.

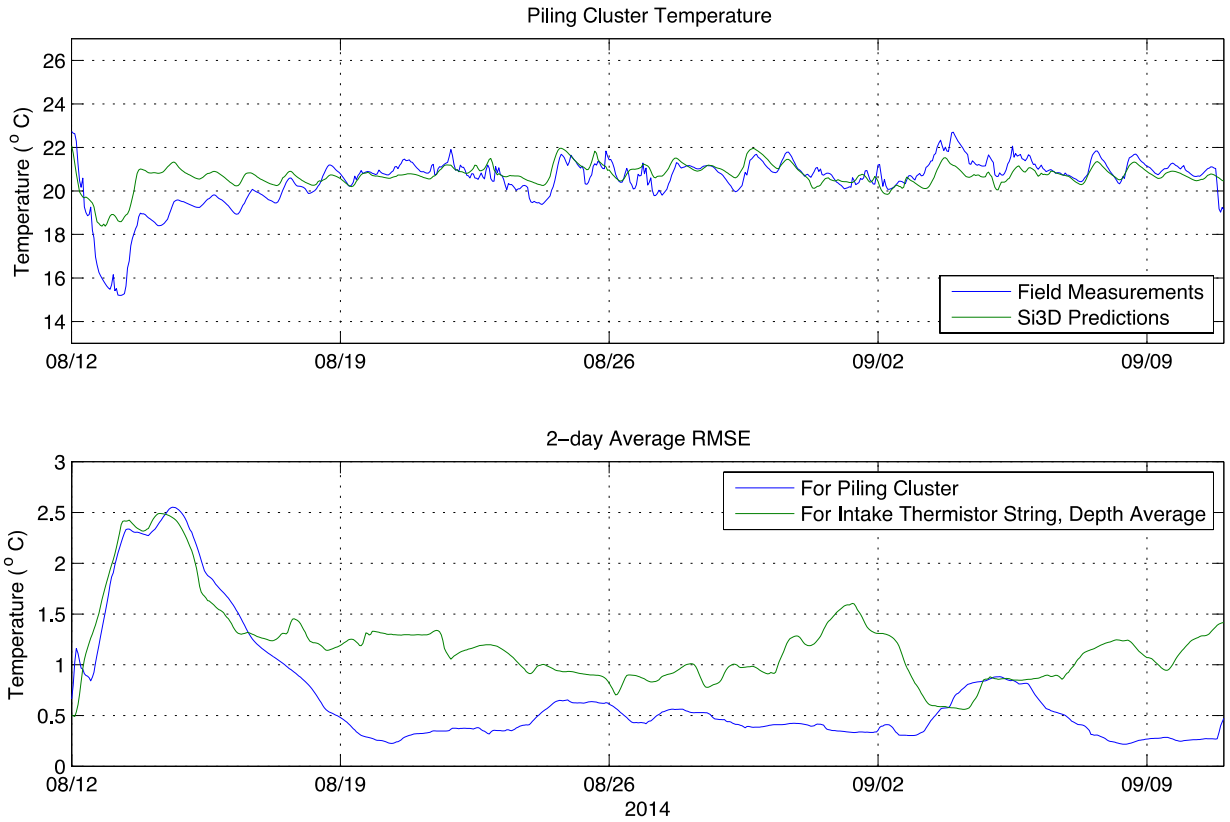

Figure A-37. The top panel compares field measurements and model predictions of water temperature at the piling cluster for the 2014 validation study. The bottom panel shows a 2-day running average of the root mean square error, comparing measured to modeled temperatures at the piling cluster, and also shows the depth average of the 2-day running average root mean square error for the intake thermistor string.

Table A-5. Root mean square error, averaged over the entire duration of each validation study, comparing field measurements to model predictions, for the piling cluster temperature, for the temperatures measured by the thermistor chain near the LSC intake, and for the thermocline depth at the location of the intake thermistor chain.

	2012	2013	2014
Piling Cluster Water Temperature RMSE	0.81 ^{o}C	0.73 ^{o}C	0.88 ^{o}C
Depth-Average RMSE for Intake Thermistor String Temperatures	1.29 ^{o}C	1.12 ^{o}C	1.37 ^{o}C
Thermocline Depth RMSE	1.8 m	1.6 m	2.7 m

A.4.6 Residence Time Studies

A.4.6.1 Method for Estimating Residence Time

Hydraulic residence time is defined as the amount of time a parcel of water remains within an aquatic system. The individual molecules within a parcel of water will leave the system at different times – thus

residence time is a stochastic quantity, having a mean, standard deviation, and higher order statistics. If a passive tracer (such as a dye) with total mass M_0 is released with the water parcel, and M(t) is mass of passive tracer remaining within the system after time t, then the mean residence time, T_R, is given by:

$$T_R = \frac{1}{M_0}\int_0^\infty M(t)\,dt. \tag{52}$$

(e.g. Hilton et al., 1998). In practice, it is not possible to track the tracer for an infinite amount of time, but we may examine the behavior of the following quantity:

$$\Theta_R(t) = \frac{1}{M_0}\int_0^t M(t)\,dt. \tag{53}$$

which has the property:

$$\lim_{t\to\infty} \Theta_R(t) = T_R \tag{54}$$

to determine whether our measurement of mean residence time is converging to a constant value. If convergence is not obtained by the end of an experiment, at $t = t_N$, examining $\Theta_R(t)$ curves and evaluating $\Theta_R(t_N)$ may still be informative.

In our numerical residence time experiments, after a seven-day model warm-up period, passive tracers are released at the LSC sampling sites. The tracer mass is evenly distributed over depth within a single column of cells. We track the mass of each tracer on the shelf, using two different definitions of the shelf:

(1) the region of the lake south of the 6m depth contour, and
(2) the region of the lake south of the 303d line.

The tracers are tracked for 30 days. The total length of the simulations is 37 days – a seven-day warmup period is included before the tracer releases. The tracers are followed at various locations in southern Cayuga Lake, corresponding to monitoring sites from the LSC program in place from 1998-2012 (Figure A-39).

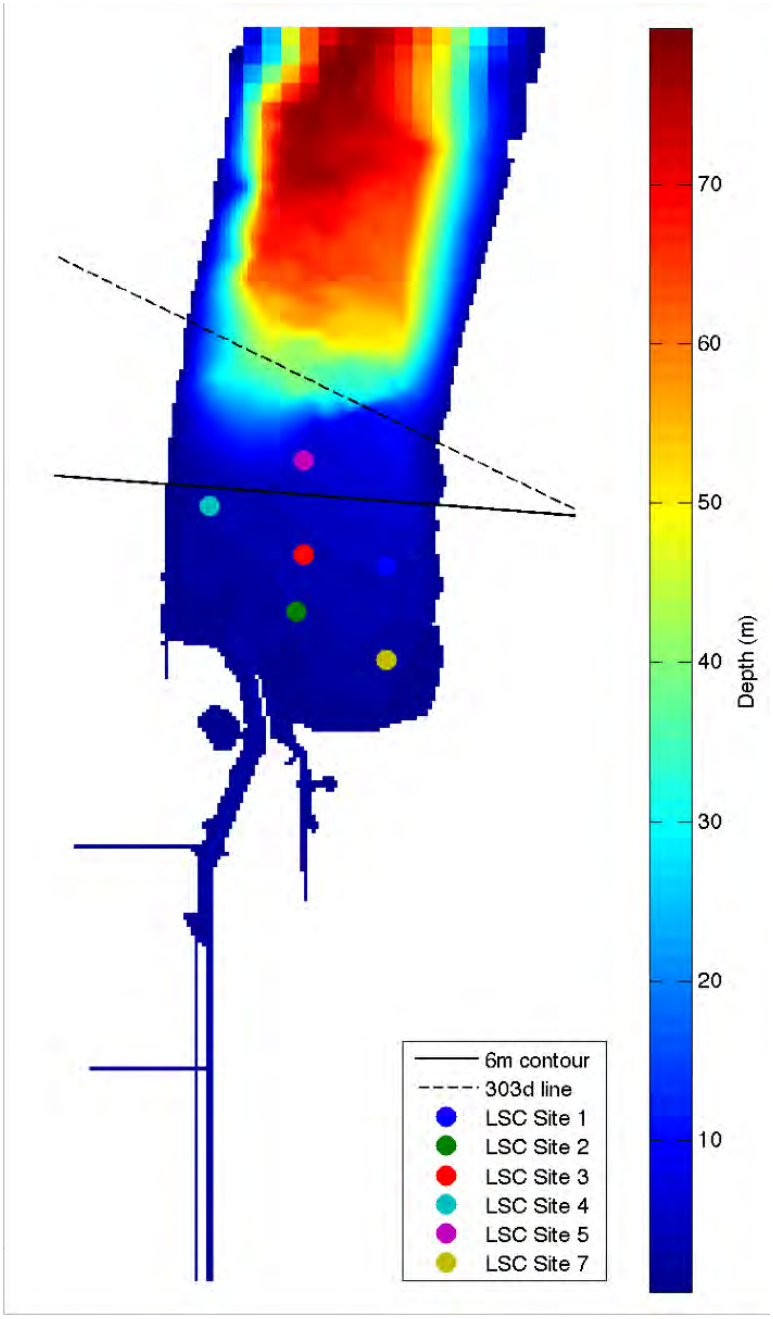

Figure A-38. Map showing LSC sampling sites, which are the tracer release sites for the residence time studies, on the high resolution grid. The 6m contour and 303d line that define the "shelf" for the purpose of computing residence time, are also shown.

A.4.6.2 Forcing Scenarios for Residence Time Studies

In the workplan we proposed to study the effect of the LSC outfall location under the following conditions:

- Summer stratification regime, high tributary flows (for summer), high summer point source flows, strong winds
- Summer stratification regime, low tributary flows (for summer), high summer point source

flows, low winds

- Summer stratification regime, low tributary flows (for summer), high summer point source flows, strong winds

Summer Stratification Regime

To ensure a summer stratification regime, we run the residence time simulations during the time period of July 25, 2013 – August 30, 2013, releasing the passive tracers at the sampling sites on August 1, 2013. The initial condition is specified by the temperature profile measured on July 25, 2013, and the simulation is given seven days to warm up before the tracer release. Boundary conditions including all meteorological forcings (except wind), water surface elevation at the north end, and temperatures at the open boundaries, are all taken from field measurements during the July 25, 2013 – August 30, 2013 period. Wind speeds and directions are altered from the 2013 values to create "high wind" and "low wind" scenarios, and tributary flow rates are altered to create "high flow" and "low flow" scenarios. Point source inputs are altered from the 2013 values to ensure "high summer point source flows". Below we describe our choice of point source input conditions, wind speeds/directions, and tributary flow rates for the residence time simulations.

High Summer Point Source Flows

Point sources include the LSC outfall, IAWWTP outfall, and CHWWTP outfall. Box and whisker plots showing monthly statistics of flow rate and effluent temperature for the three point sources are presented in Figure A-39, Figure A-40, and Figure A-41. Effluent flow rate and temperature are specified as input to the numerical model. For all three point sources, we used the median August effluent temperature. For IAWWTP and CHWWTP, we also used the median August flow rate, and for LSC we used the maximum capacity flow rate. These values are shown in Table A-6.

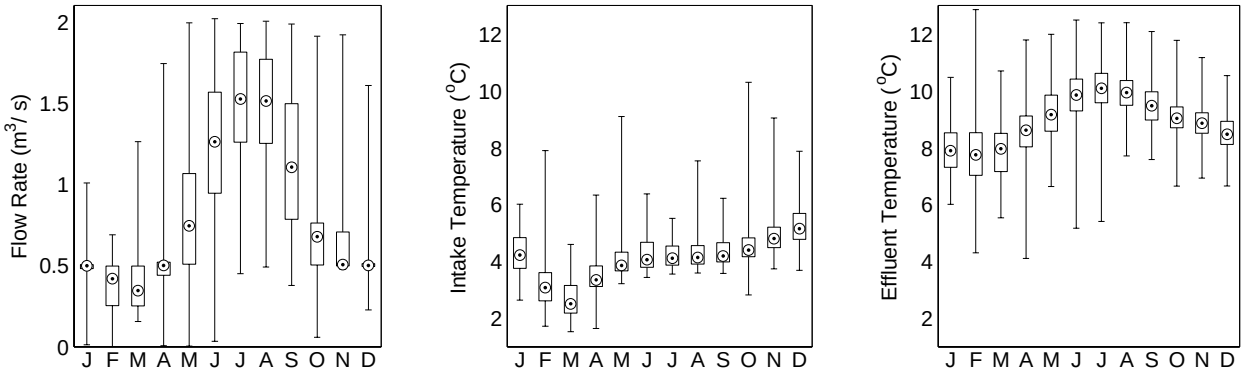

Figure A-39. Statistics of LSC intake/effluent flow rate, intake temperature, and effluent temperature, by month. Circled dots indicate medians, boxes span 25th to 75th percentiles, and whiskers extend to minima and maxima. Statistics are based on values measured hourly between 2005 (when the continuous monitoring system was installed) and August 2013.

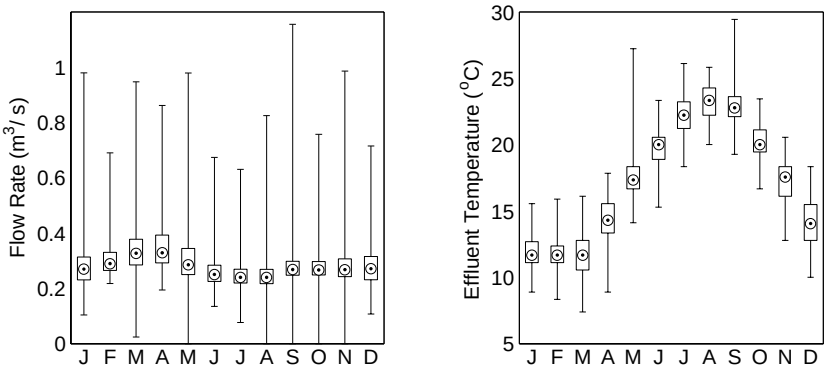

Figure A-40. Statistics of IAWWTP effluent flow rate and temperature, by month. Circled dots indicate medians, boxes span 25th to 75th percentiles, and whiskers extend to minima and maxima. Statistics are based on values measured daily between 1995 and 2014.

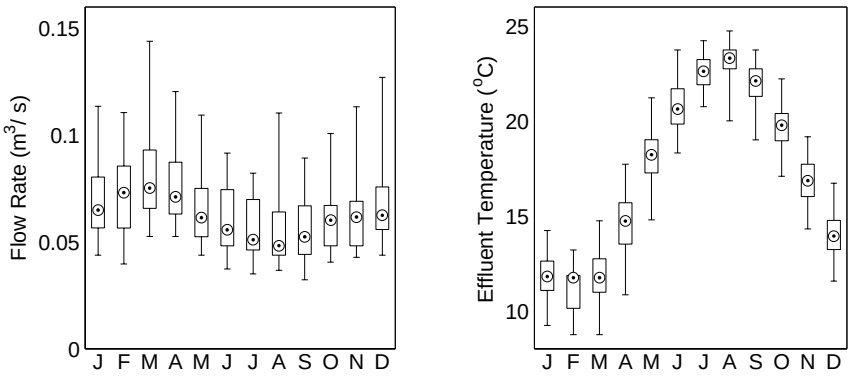

Figure A-41. Statistics of CHWWTP effluent flow rate and temperature, by month. Circled dots indicate medians, boxes span 25th to 75th percentiles, and whiskers extend to minima and maxima. Statistics are based on monthly values made publically available in the 2000-2015 SPEDES reports.

Table A-6. Point source input to the numerical model representing "high summer point source flows".

	LSC	IAWWTP	CHWWTP
Effluent Flow Rate	2.00 m^3/s	0.24 m^3/s	0.05 m^3/s
Effluent Temperature	9.9 °C	23.3 °C	23.3 °C

Strong Winds/Low Winds

To define high and low winds, we turned to the hourly wind records measured at Game Farm Road (GFR) from 1987-2013. We transformed the wind records to obtain piling cluster equivalents as discussed in Section **A.2.3**. Then we took a 30-day-long rolling root mean square (RMS) average of the entire wind speed record, computing the average at each hourly data point for the following 30 days. Using only the averages contained within summer (June 1 – September 30), we sorted from smallest to largest – the result is the cumulative density function shown in Figure A-42 and found (1) the commencement date of the minimum 30-day RMS wind speed and (2) the commencement date of the 95th percentile 30-day RMS wind speed. The minimum of 2.4 m/s was measured during the 30-day period commencing on July 17, 2003 at 9:00 EST, and the 95th percentile of 4.0 m/s was measured

during the 30-day period commencing on June 14, 1992 at 13:00 EST. To obtain 37-day long wind records corresponding to the "low" and "high" wind scenarios, we used the historical records commencing on July 10, 2013 at 9:00 EST and June 7, 1992 at 13:00 EST, respectively. The tracer releases are thus conducted at the commencement of the "low" and "high" wind records, seven days after the start of the simulations.

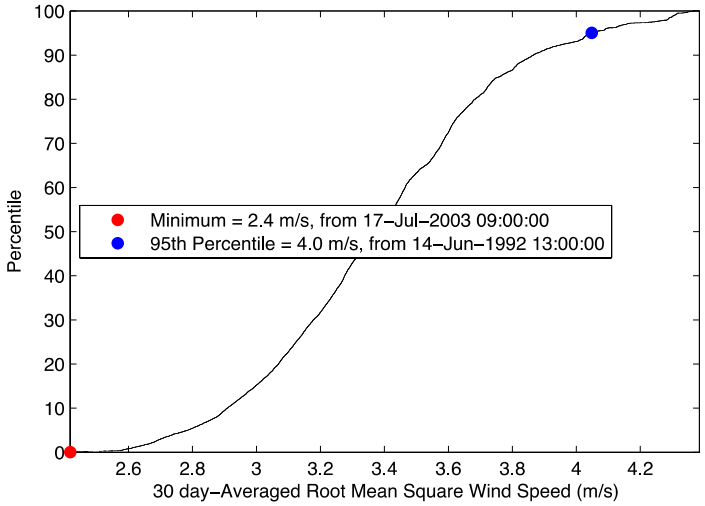

Figure A-42. Cumulative density function for 30-day root mean square wind speed, computed from hourly wind records measured 1987-2013 during the summer time windows (June 1 – September 30).

High Tributary Flows/Low Tributary Flows

To define high and low tributary flows, we turned to the 15-min records measured by the USGS in the southern tributaries, from 1990-2015. We took a month-long rolling average of the entire discharge record. The rolling average was computed every 15 minutes. Then we sorted the averages and found (1) the minimum 30-day average tributary flow rate and (2) the 95th percentile 30-day average tributary flow rate, contained within the summer periods (June 1 – September 30). The cumulative density function of 30-day average tributary flow rate is shown in Figure A-43. The minimum of 0.6 m^3/s was measured during the 30-day period commencing on August 14, 1999 23:45 EST, and the 95th percentile of 16.9 m^3/s was measured during the 30-day period commencing on June 9, 2006 3:00 EST. To obtain 37-day long tributary flow records corresponding to the "low" and "high" flow scenarios, we used the historical records commencing on August 7, 1999 23:45 EST and June 2, 2006 3:00 EST, respectively. The tracer releases are thus conducted at the commencement of the "low" and "high" tributary flow records, seven days after the start of the simulations.

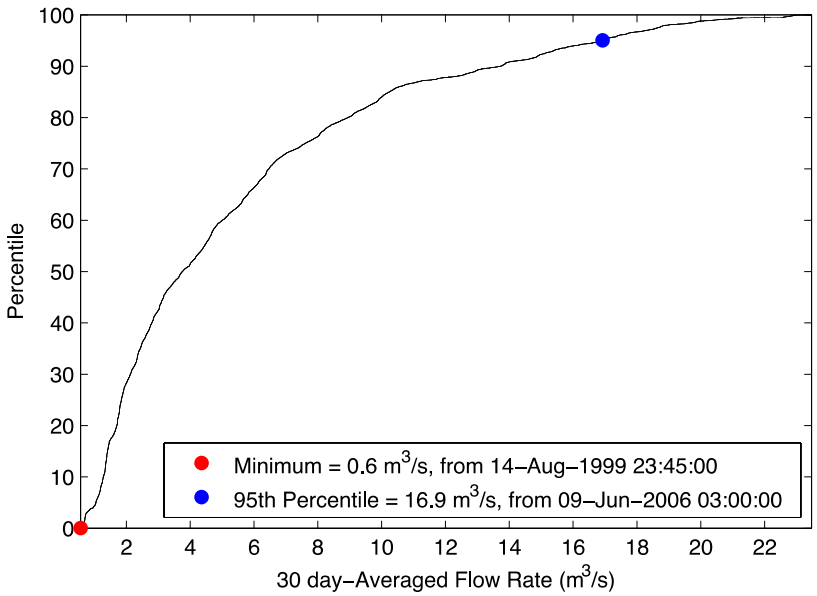

Figure A-43. Cumulative density function for 30-day average tributary flow rate, computed from 15-min records measured 1990-2015 during the summer time windows (June 1 – September 30).

A.4.6.3 Model Inputs for Residence Time Studies

The initial condition specified for the residence time study is the same temperature profile used for the 2013 validation study (refer to Figure A-24. Non-wind meteorological conditions, water surface elevation at the north end, and temperatures of the streams are also the same as for the 2013 validation studies, and are shown here in Figure A-44 and Figure A-45. Wind and tributary flow inputs depend on the forcing scenario, and are shown in Figure A-46 and Figure A-47.

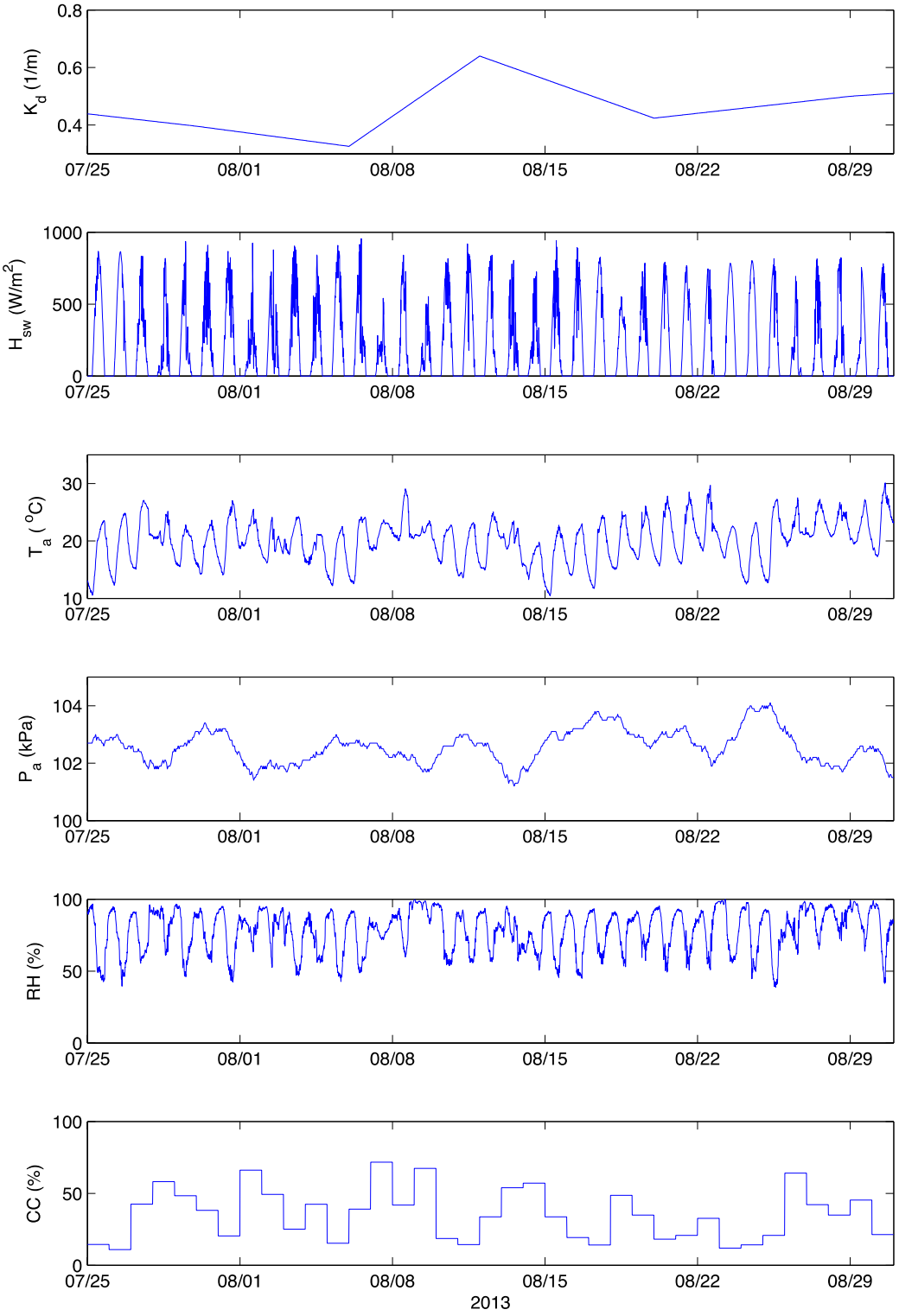

Figure A-44. Non-wind-related surface boundary conditions for residence time studies.

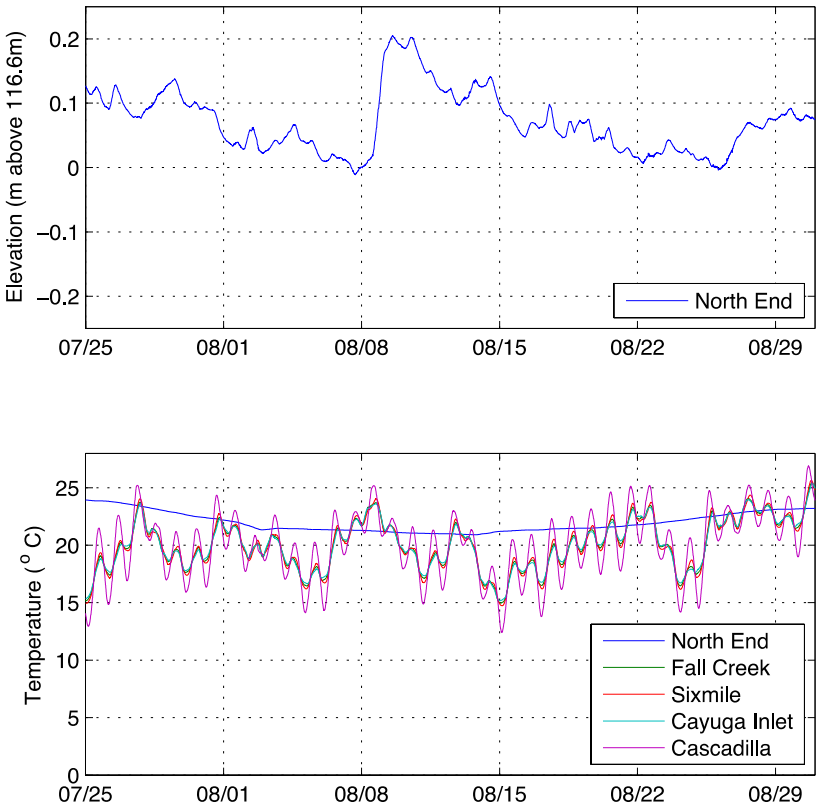

Figure A-45. Water surface elevations at the north end and temperatures in the tributaries specified at open boundaries within residence time simulations.

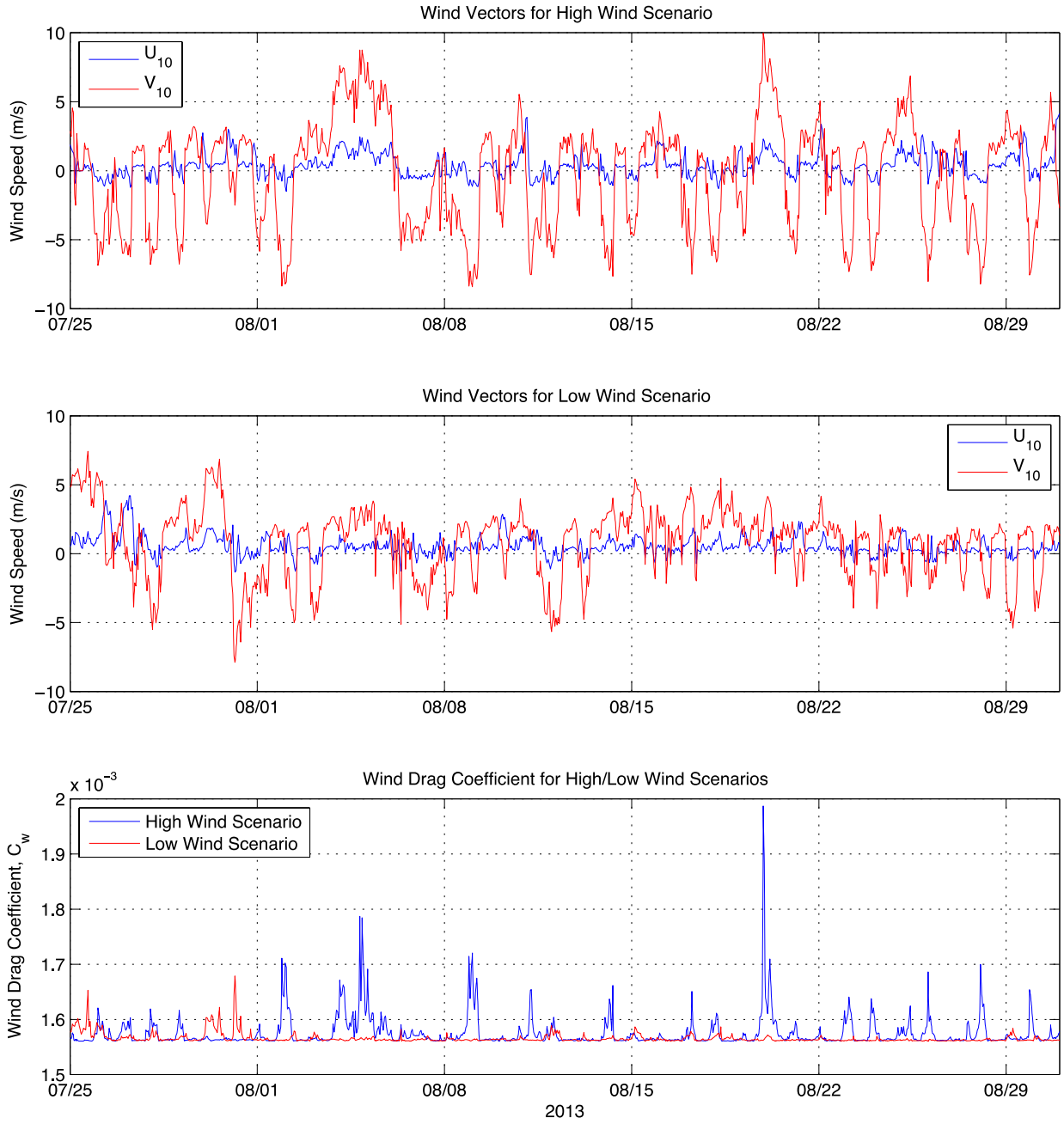

Figure A-46. Wind boundary conditions for the "high" and "low" wind speed scenarios in the residence time simulations. High wind records come from July 10, 2013 at 9:00 EST – August 17, 2013 9:00 EST, and low wind records come from June 7, 1992 13:00 EST – July 14, 1992 13:00 EST. The 2013 dates plotted in the figure correspond to the dates of the simulation.

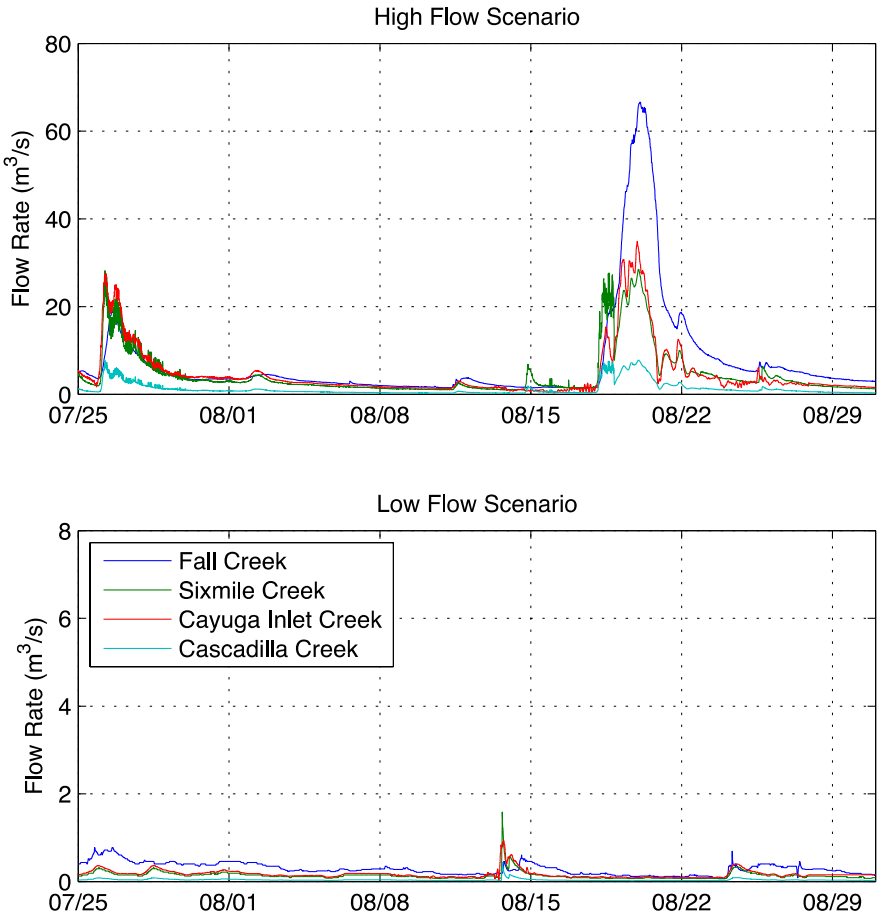

Figure A-47. Open boundary conditions specified for "high" and "low" flow scenarios in the residence time simulations. High flow records come from June 2, 2006 3:00 EST – July 9, 2006 3:00 EST, and low flow records come from August 7, 1999 23:45 EST – September 14, 1999 23:45 EST. Note that the flow rate axis scale differs by an order of magnitude between the top and bottom panels.

A.4.6.4 Results of the Residence Time Studies

Please note that all results presented here are from the LR simulations, and hence are provisional. Final results from the HR simulations will be provided at a later date, in a supplementary report. We do not expect the general result – smaller residence times on the southern shelf with the as-built LSC diffuser in place, compared to the extended outfall scenario, to change with the HR simulations, although the residence time estimates may change somewhat.

Here we present results of the residence time studies for the three cases described in the workplan:

(1) High flow, high wind
(2) Low flow, high wind
(3) Low flow, low wind

We show records of mass remaining on the shelf, M(t), and integrated mass remaining on the shelf $\Theta_R(t)$, as defined in Equation (52) and (53), respectively. As time approaches infinity, $\Theta_R(t)$ approaches

the mean residence time. $\Theta_R(t)$ does not fully converge in any of our simulations, but we use the value at the end of the simulations as an approximation of mean residence time. This is a reasonable thing to do, especially for purposes of comparison between different simulations, provided that the duration of the simulations is the same, which it is, and that $\Theta_R(t)$ is begins to approach convergence, which is appears do in all simulations. We show M(t) and $\Theta_R(t)$ curves for tracers released at each of the LSC sampling sites, using two definitions of the "shelf":

(1) the region south of the 6m depth countour, and
(2) the region south of the 303(d) line.

M(t) curves are shown in Figure A-48 through Figure A-53, and corresponding $\Theta_R(t)$ curves are shown in Figure A-54 through Figure A-59. In Table A-7 and Table A-8 we report values of $\Theta_R(t)$ at the end of each simulation, which serve as approximations of mean residence time. In these figures, t=0 corresponds to August 1, 2013 – the time of the passive tracer releases.

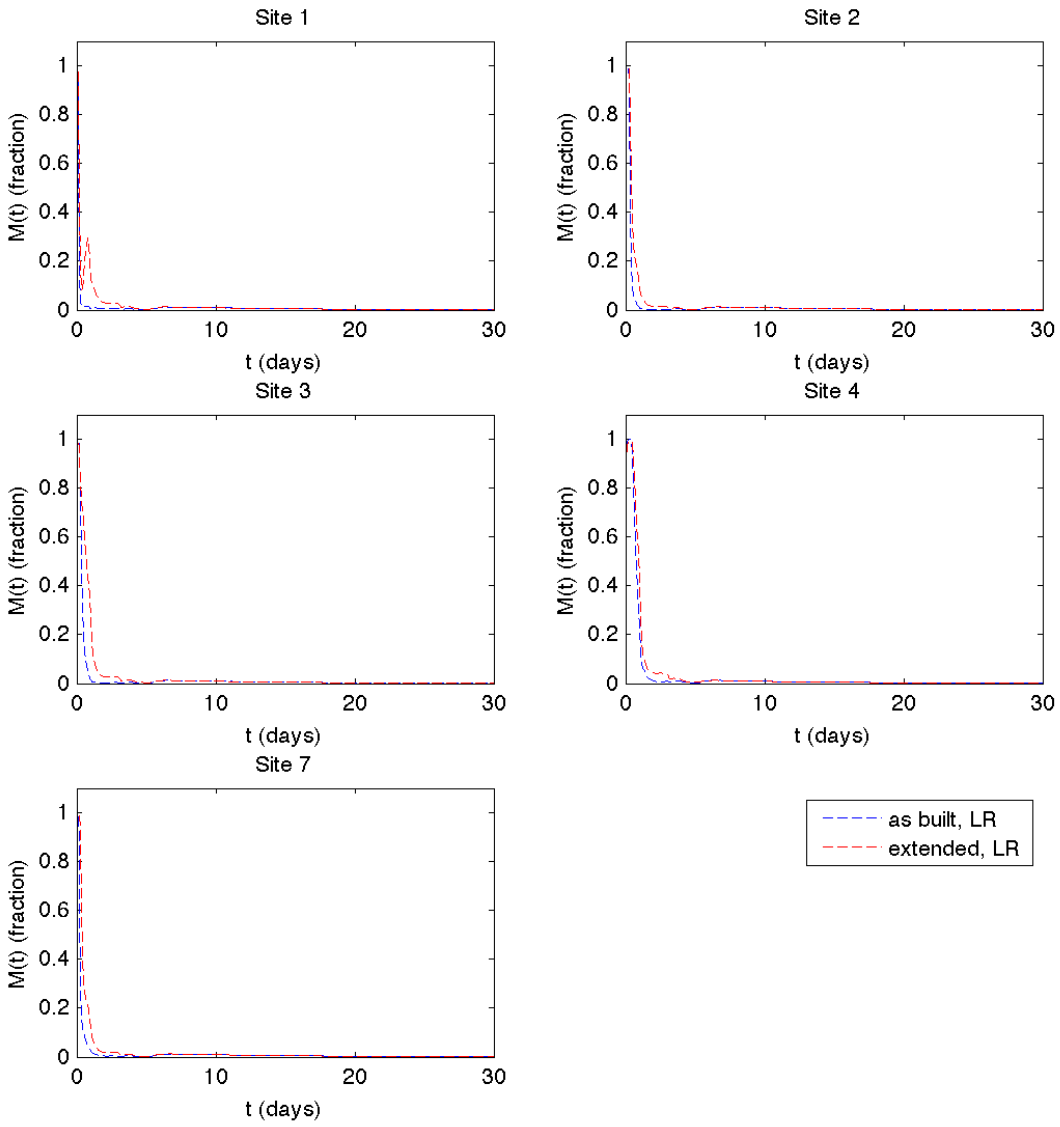

Figure A-48. M(t) for the high flow/high wind residence time simulation, using the 6m depth contour as the northern border of the "shelf" system. High resolution results are pending.

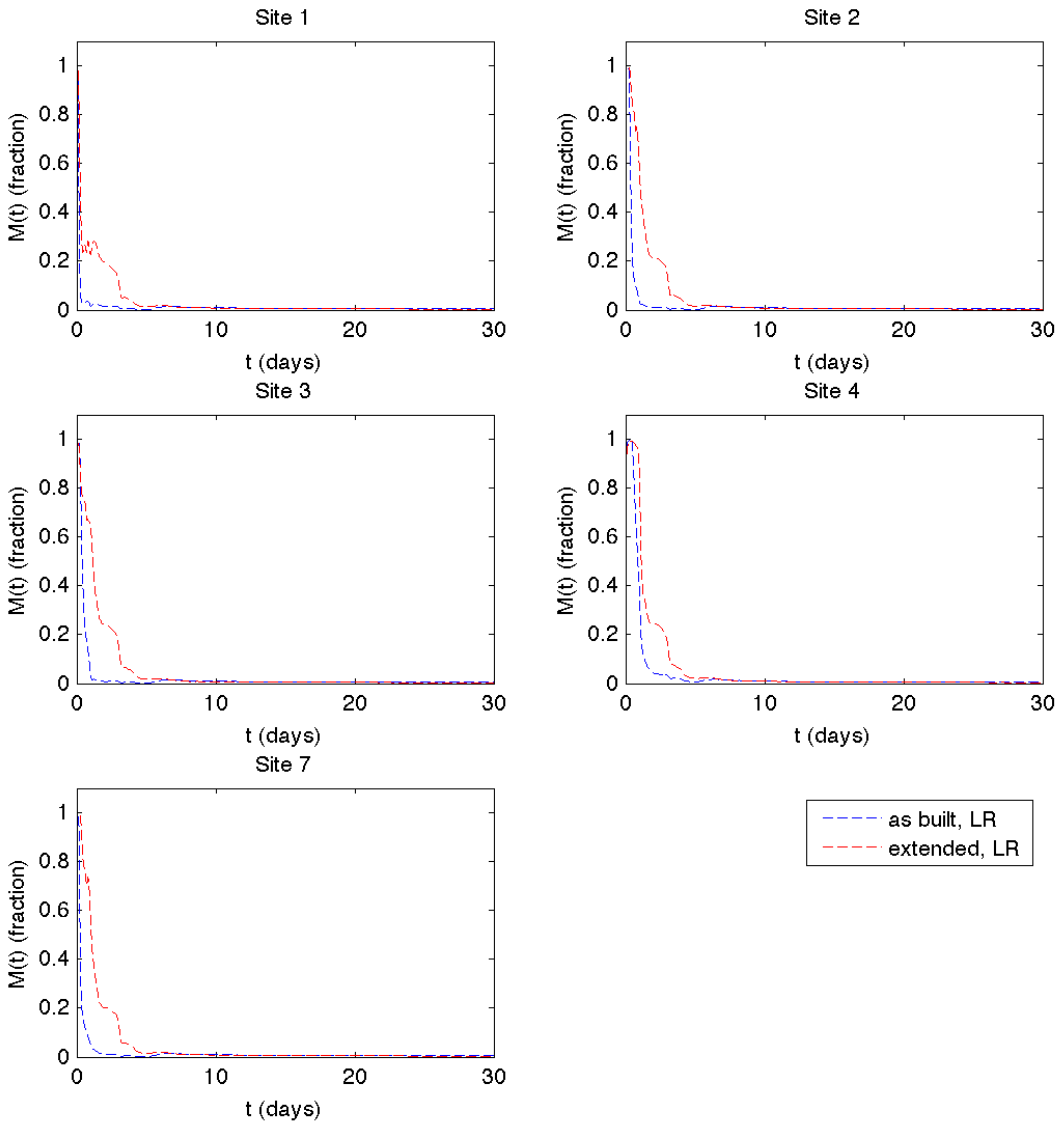

Figure A-49. M(t) for the low flow/high wind residence time simulation, using the 6m depth contour as the northern border of the "shelf" system. High resolution results are pending.

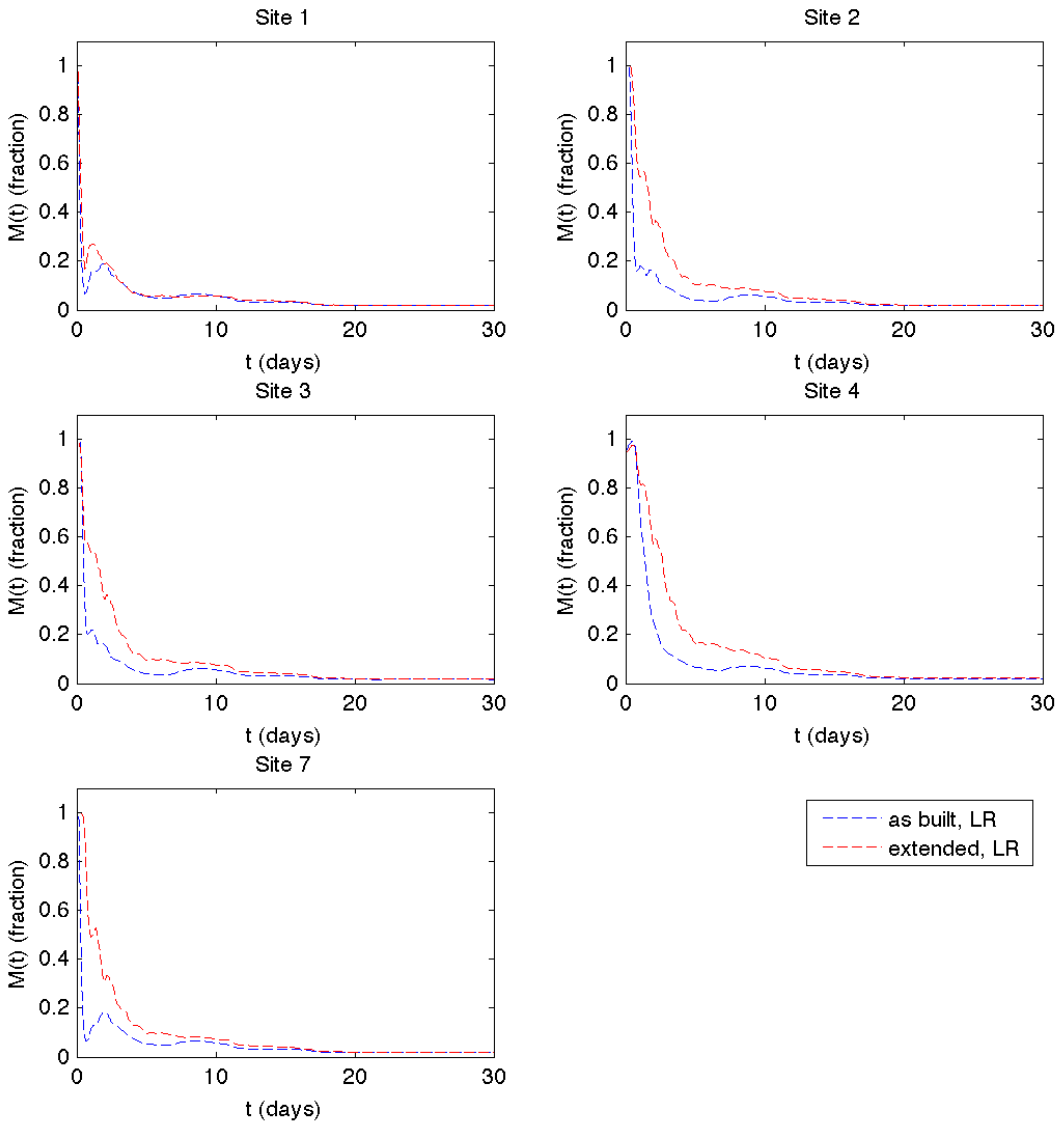

Figure A-50. M(t) for the low flow/low wind residence time simulation, using the 6m depth contour as the northern border of the "shelf" system. High resolution results are pending.

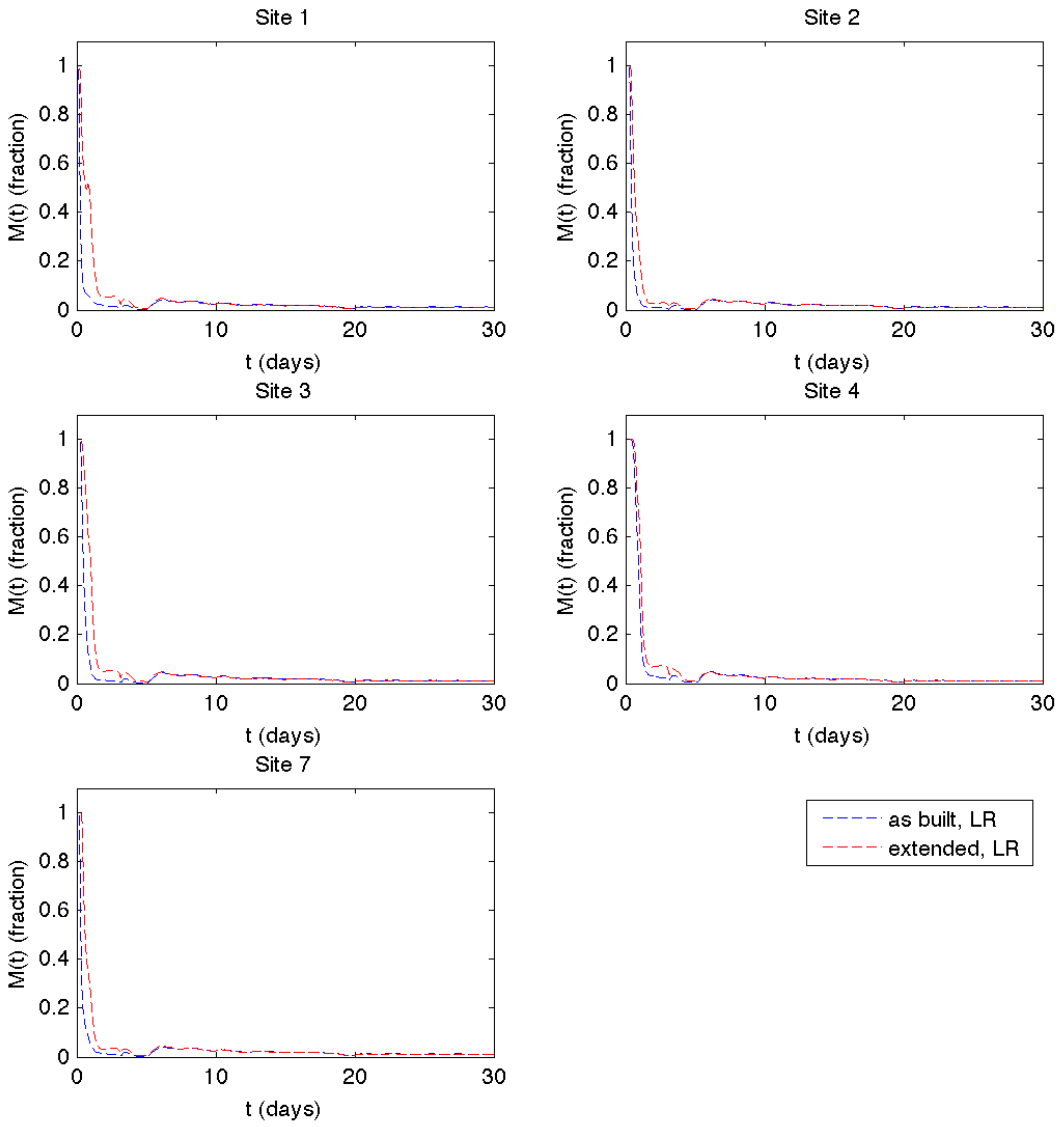

Figure A-51. M(t) for the high flow/high wind residence time simulation, using the 303(d) line as the northern border of the "shelf" system. High resolution results are pending.

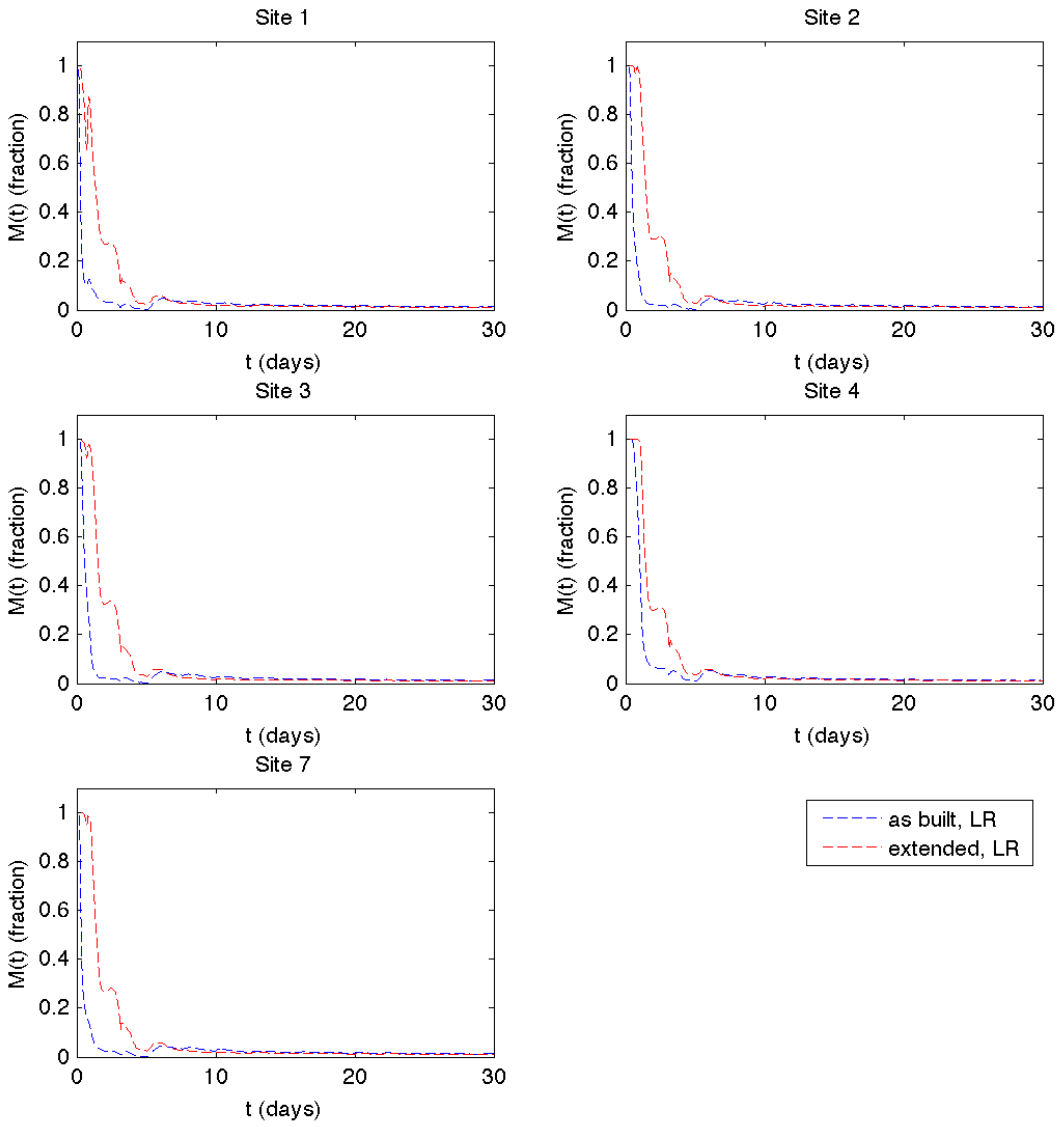

Figure A-52. M(t) for the high flow/low wind residence time simulation, using the 303(d) line as the northern border of the "shelf" system. High resolution results are pending.

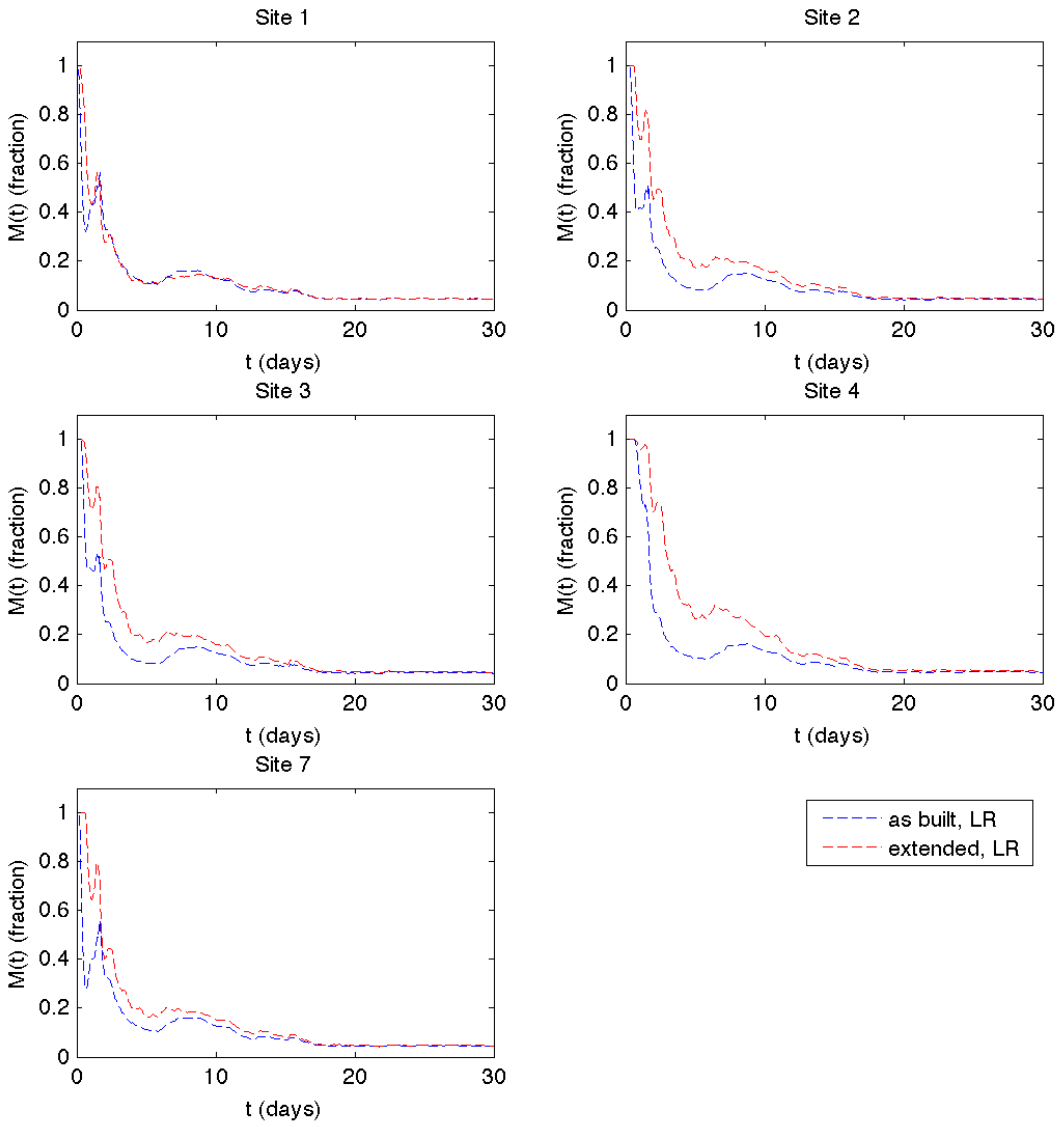

Figure A-53. M(t) for the low flow/low wind residence time simulation, using the 303(d) line as the northern border of the "shelf" system. High resolution results are pending.

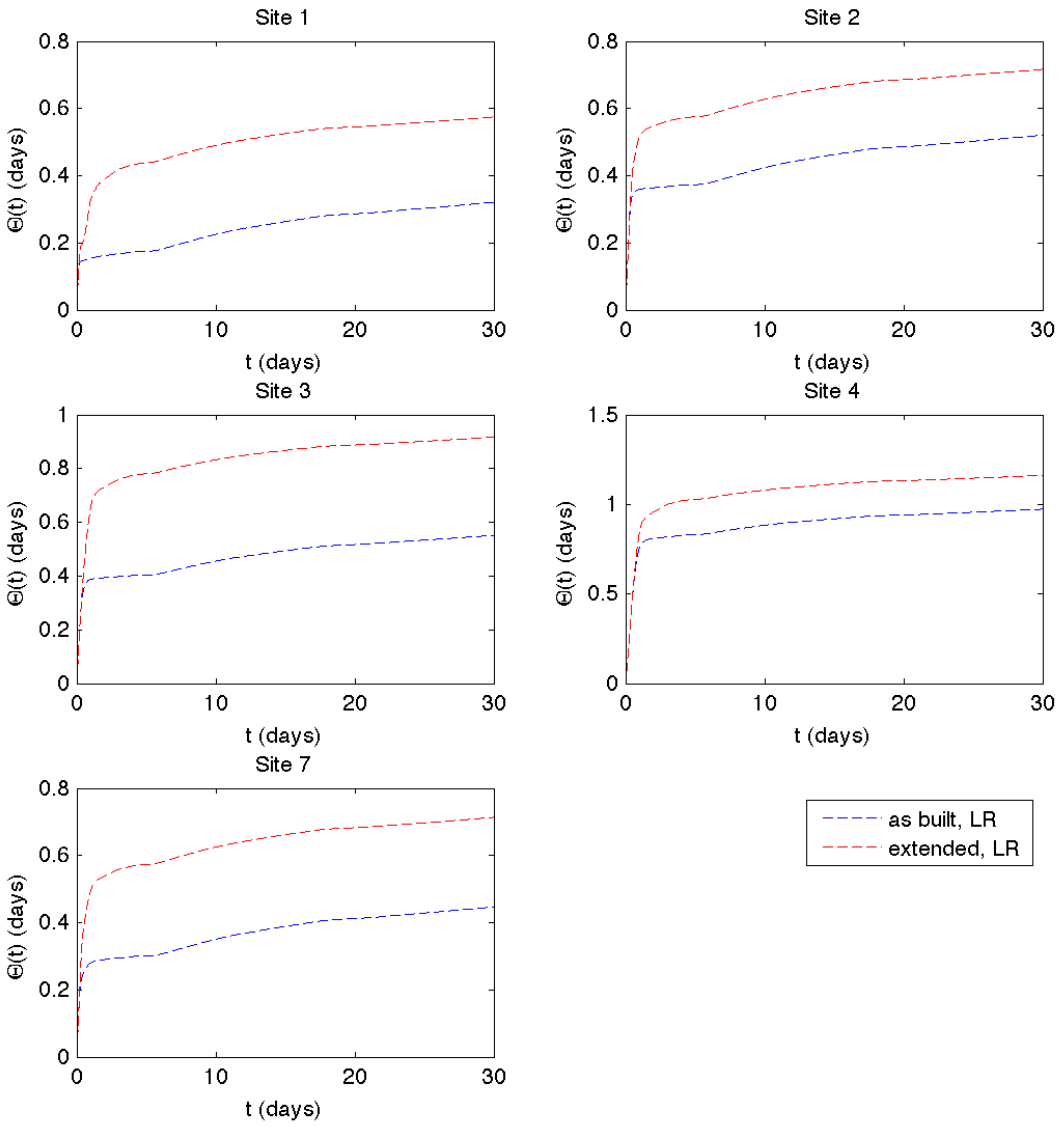

Figure A-54. $\Theta_R(t)$ for the high flow/high wind residence time simulation, using the 6m depth contour as the northern border of the "shelf" system. High resolution results are pending.

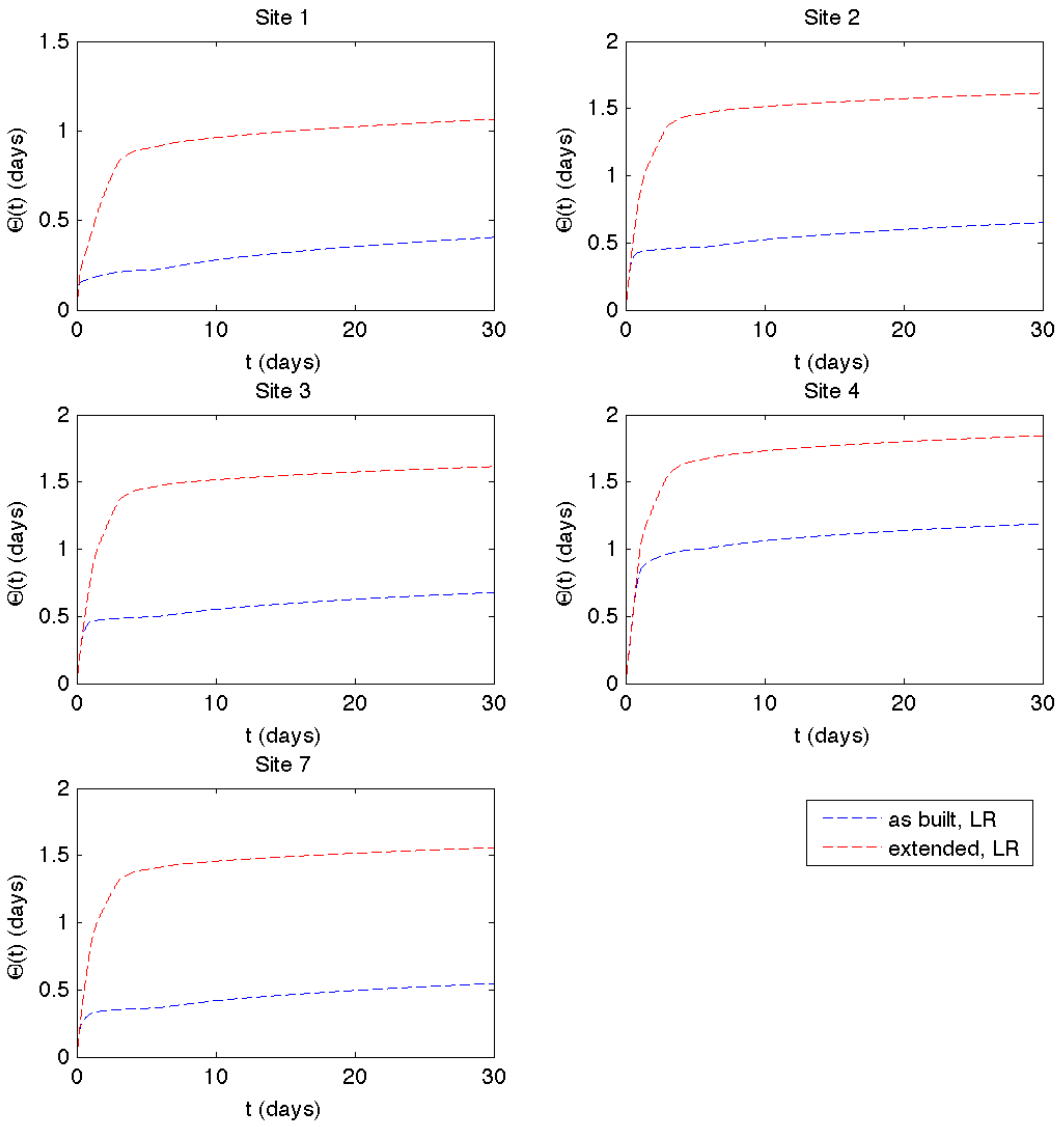

Figure A-55. $\Theta_R(t)$ for the low flow/high wind residence time simulation, using the 6m depth contour as the northern border of the "shelf" system. High resolution results are pending.

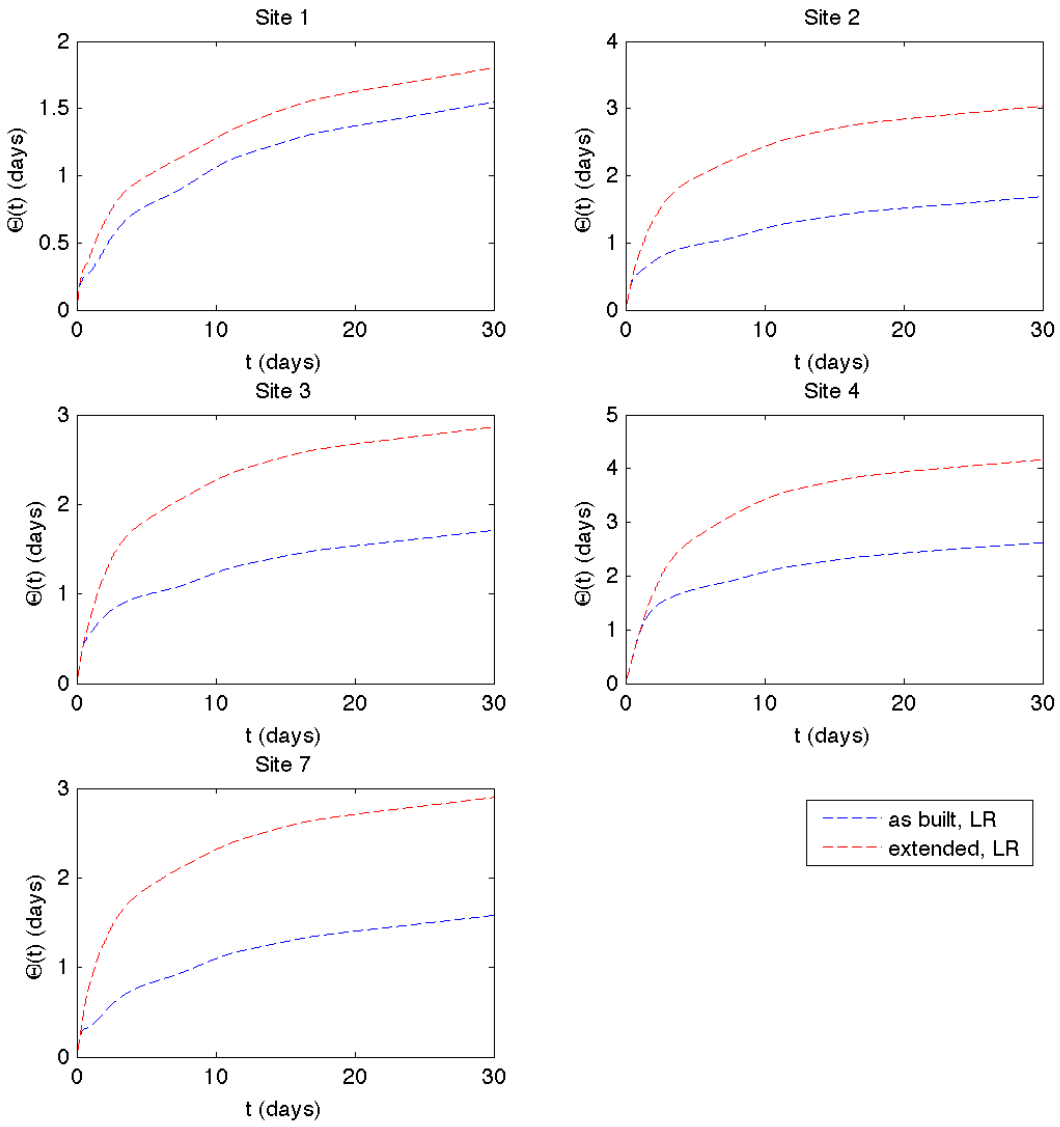

Figure A-56. $\Theta_R(t)$ for the low flow/low wind residence time simulation, using the 6m depth contour as the northern border of the "shelf" system. High resolution results are pending.

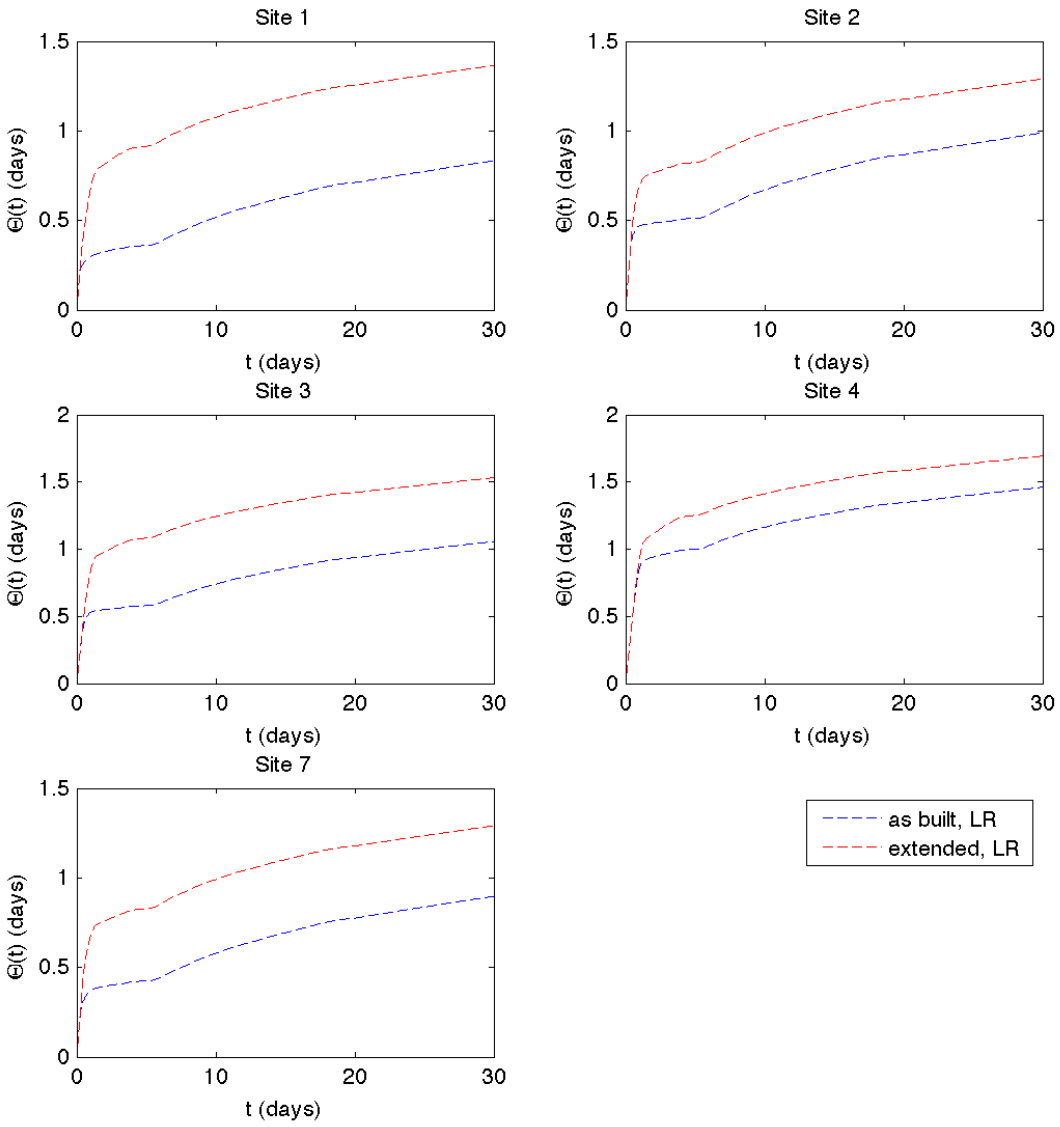

Figure A-57. $\Theta_R(t)$ for the high flow/high wind residence time simulation, using the 303(d) line as the northern border of the "shelf" system. High resolution results are pending.

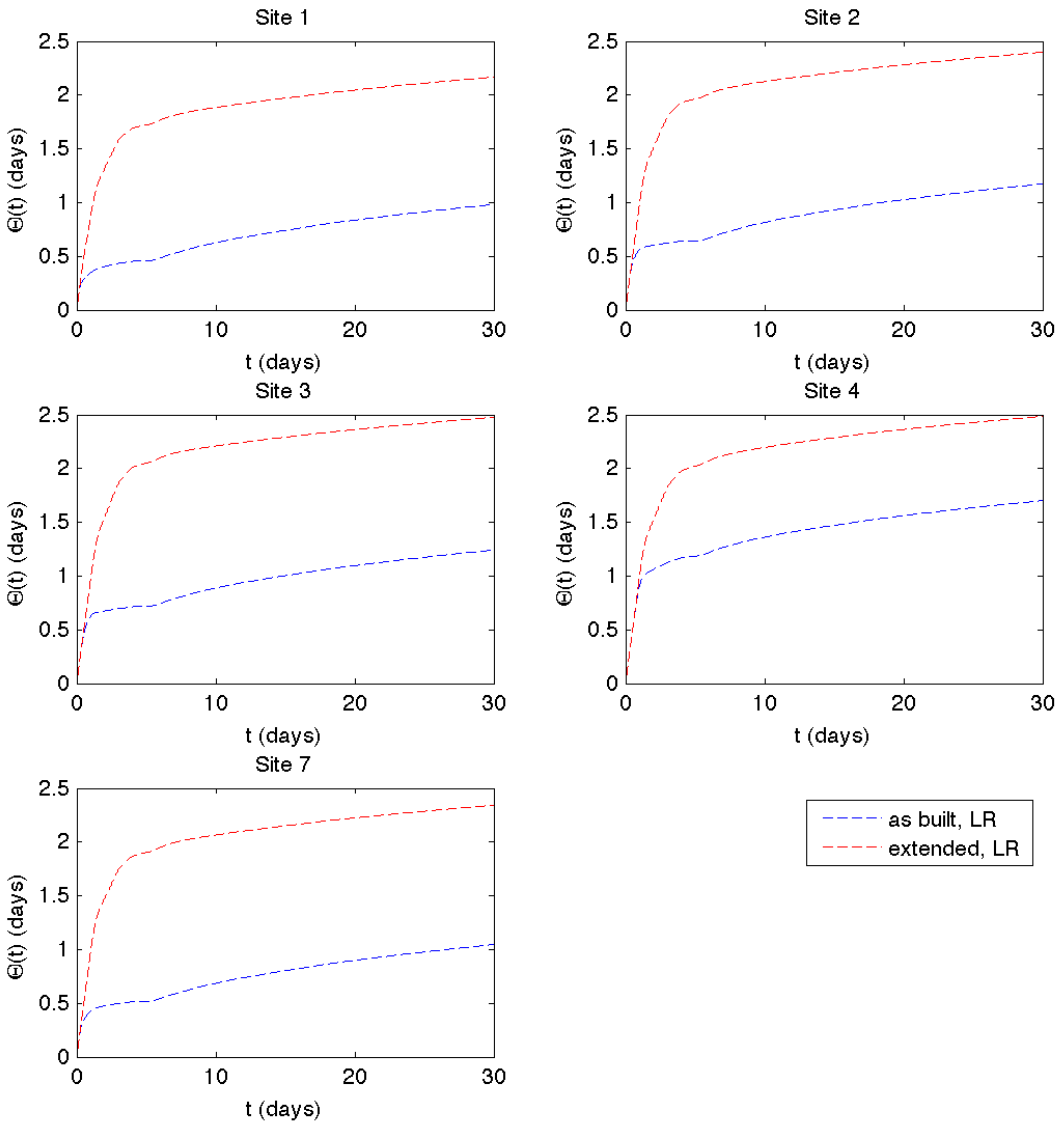

Figure A-58. $\Theta_R(t)$ for the high flow/low wind residence time simulation, using the 303(d) line as the northern border of the "shelf" system. High resolution results are pending.

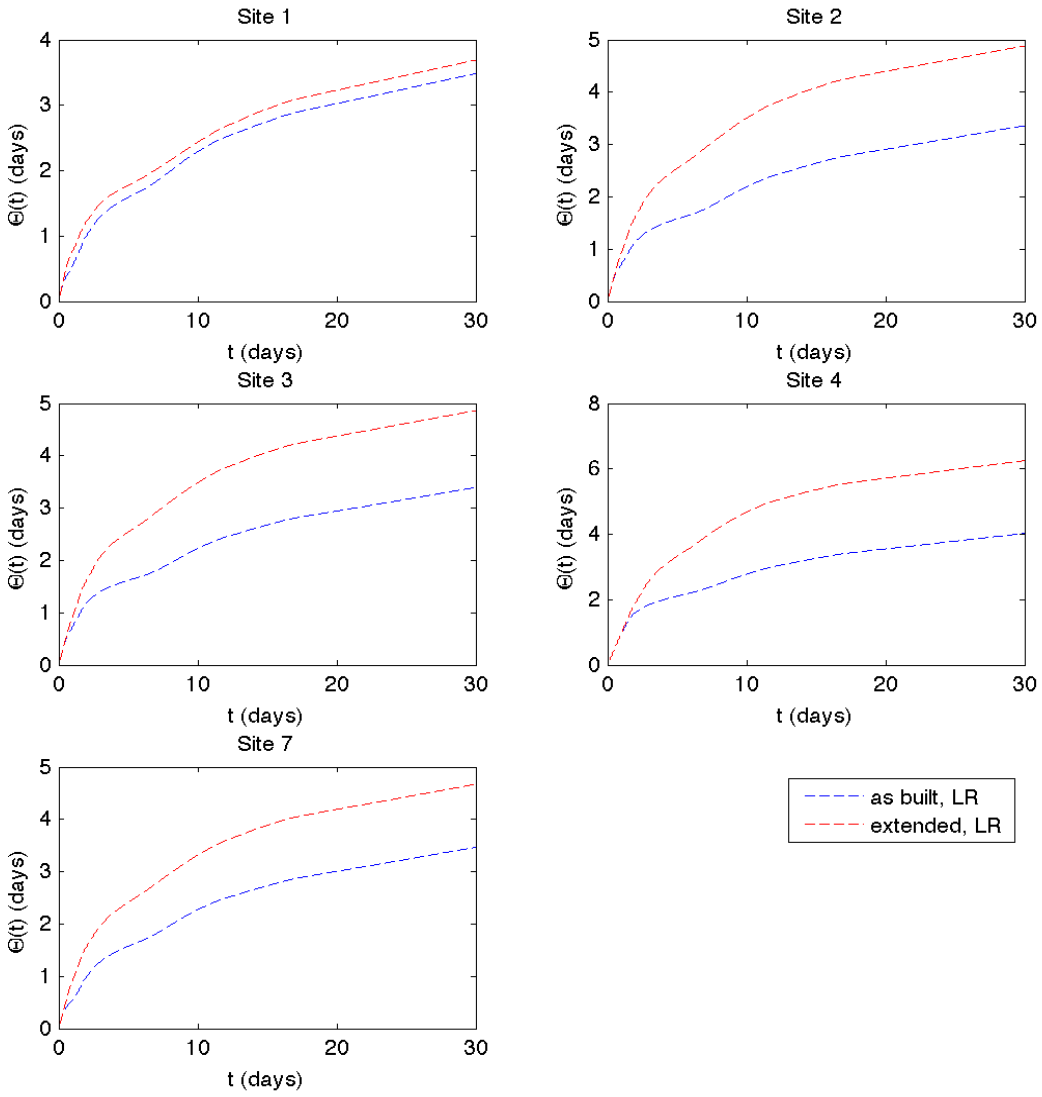

Figure A-59. $\Theta_R(t)$ for the low flow/low wind residence time simulation, using the 303(d) line as the northern border of the "shelf" system. High resolution results are pending.

Table A-7. $\Theta_R(30days)$, an approximation of mean residence time, using the 6m depth contour as the northern border of the "shelf" system, for the three meteorological scenarios, and for both as-built and extended LSC outfall scenarios.

	High Flow / High Wind		Low Flow / High Wind		Low Flow / Low Wind	
LSC Site	As built	Extended	As built	Extended	As built	Extended
1	0.32 days	0.57 days	0.40 days	1.0 days	1.5 days	1.8 days
2	0.52 days	0.71 days	0.65 days	1.6 days	1.7 days	3.0 days
3	0.55 days	0.91 days	0.67 days	1.6 days	1.7 days	2.8 days
4	0.97 days	1.2 days	1.2 days	1.8 days	2.6 days	4.2 days
7	0.45 days	0.71 days	0.55 days	1.5 days	1.6 days	2.8 days

Table A-8. $\Theta_R(30days)$, an approximation of mean residence time, using the 303d line as the northern border of the "shelf" system, for the three meteorological scenarios, and for both as-built and extended LSC outfall scenarios.

	High Flow / High Wind		Low Flow / High Wind		Low Flow / Low Wind	
LSC Site	As built	Extended	As built	Extended	As built	Extended
1	0.83 days	1.4 days	0.98 days	2.1 days	3.5 days	3.7 days
2	0.99 days	1.3 days	1.2 days	2.4 days	3.4 days	4.8 days
3	1.1 days	1.5 days	1.2 days	2.5 days	3.4 days	4.8 days
4	1.5 days	1.7 days	1.7 days	2.5 days	4.0 days	6.3 days
7	0.89 days	1.3 days	1.1 days	2.3 days	3.5 days	4.6 days

A.4.7 Mixing Zone of the As-Built Outfall

To characterize the mixing zone for the as-built outfall, we use the results of the residence time simulations described in **A.4.6**. We use the results of the HR simulations, which are preliminary, and hence these results should be considered provisional.

For the as-built cases of the HR residence time simulations, we output simulated temperature every 4 hours in planes spanning the (x,y) domain:

(1) at the bottom-most cells across the entire (x,y) domain,
(2) at the top-most cells across the entire (x,y) domain, and
(3) depth-averaged at every (x,y) location.

We take a 12-day average of these temperatures, starting 7 days into the simulation (on August 1, 2013). The mixing zone is defined as the region where temperature is 1.67^{o}C or greater below ambient temperature. To represent ambient temperature on the shelf, we use a combination of simulated temperatures from the location of the piling cluster and the location of the LSC intake. For depths above 3.0m, we use piling cluster temperatures, and for depths below 10.0m, we use intake temperatures, using linear interpolation in between 3.0m and 10.0m. We then evaluate appropriate ambient temperatures for each of the plane output data sets described above, respectively, as follows:

(1) interpolate ambient temperature onto the bottom cell depth at each (x,y) location,
(2) evaluate ambient temperature at the top-most cell elevation (the same at every x,y), and
(3) average ambient temperature over depth for each (x,y) location.

We evaluate these temperatures every 4 hours, take a 12-day average, starting on August 1, 2013, and use the resulting values as ambient for comparison to the plane output described above.

This process results in three maps of the mixing zone for each depth (bed, surface, and depth-average) times three maps for each of the test cases (high flow/high wind, low flow/high wind, and low flow/low wind). These maps are presented below. For all test cases, the mixing zone of the LSC outfall as defined

by near-bed temperatures is less than 500 m in diameter. Using depth-averaged temperature, the mixing zone is a single 25m x 25m square. Finally, the mixing zone based on surface temperatures is nonexistent.

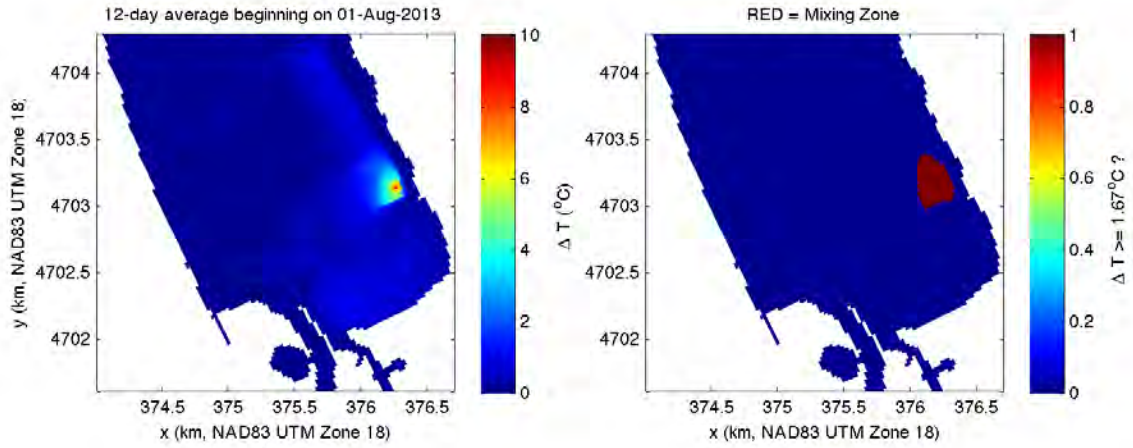

Figure A-60. Mixing zone plot based on temperature in the bottom-most cell for the high flow/high wind case.

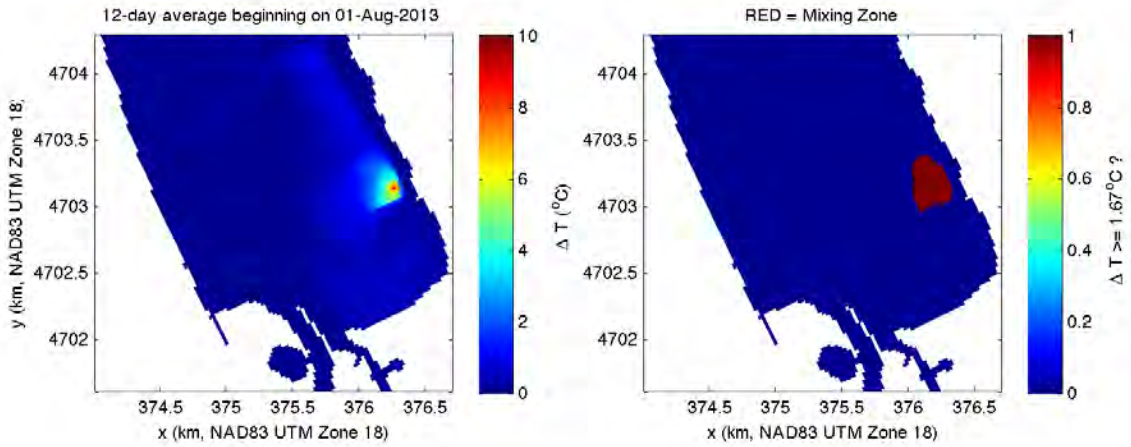

Figure A-61. Mixing zone plot based on temperature in the bottom-most cell for the low flow/high wind case.

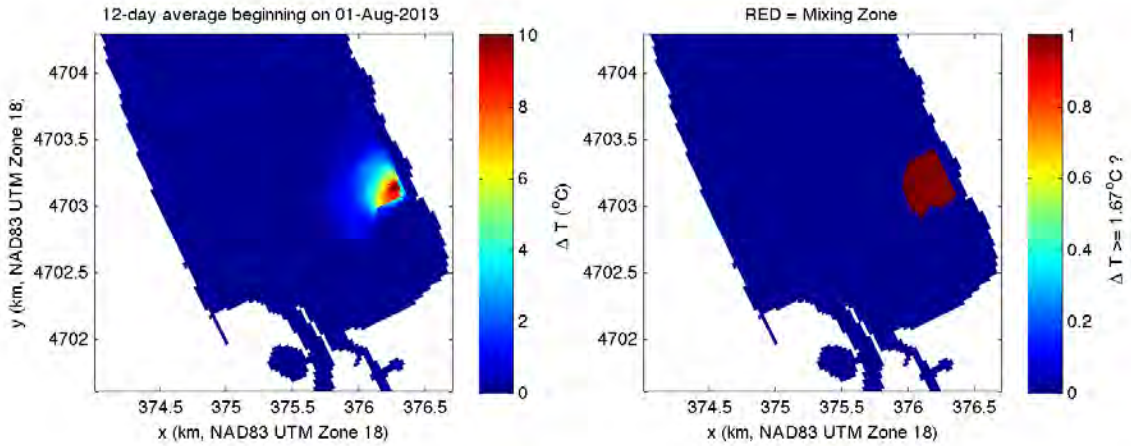

Figure A-62. Mixing zone plot based on temperature in the bottom-most cell for the low flow/low wind case.

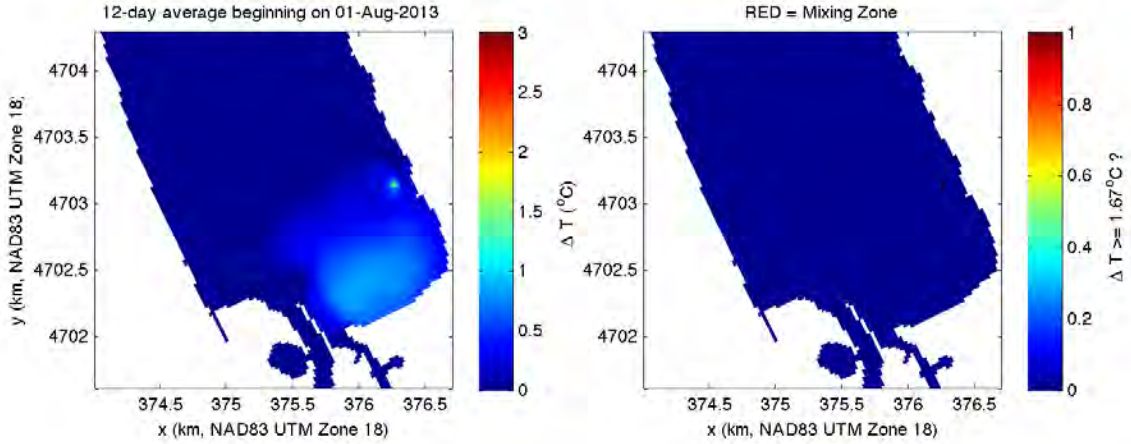

Figure A-63. Mixing zone plot based on depth-averaged temperature for the high flow/high wind case.

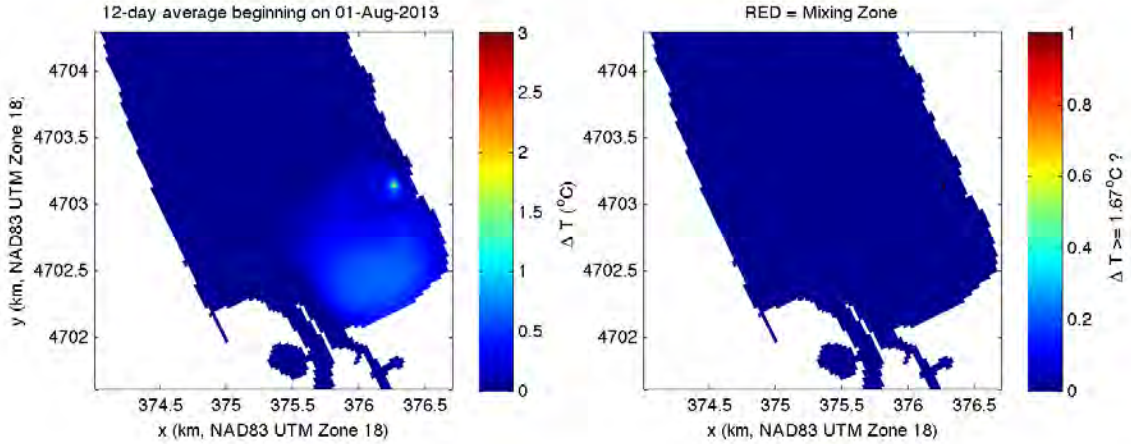

Figure A-64. Mixing zone plot based on depth-averaged temperature for the low flow/high wind case.

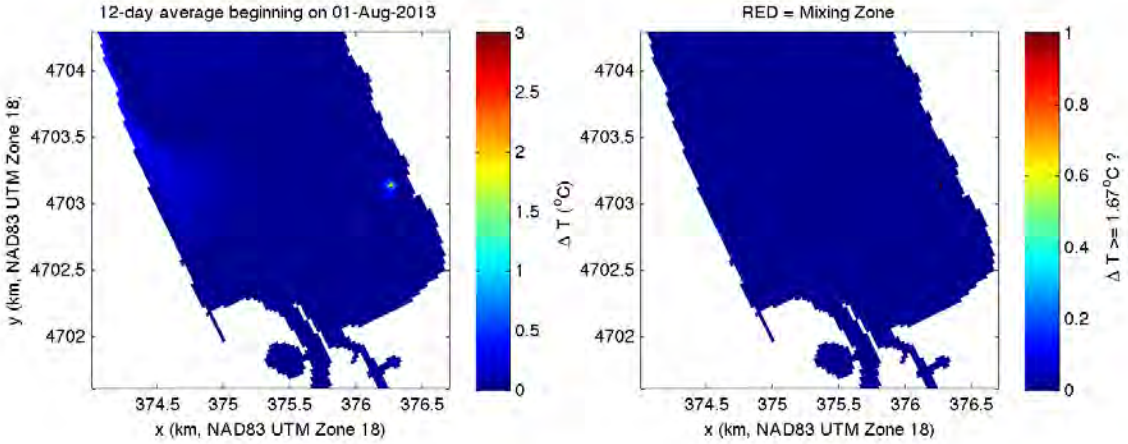

Figure A-65. Mixing zone plot based on depth-averaged temperature for the low flow/low wind case.

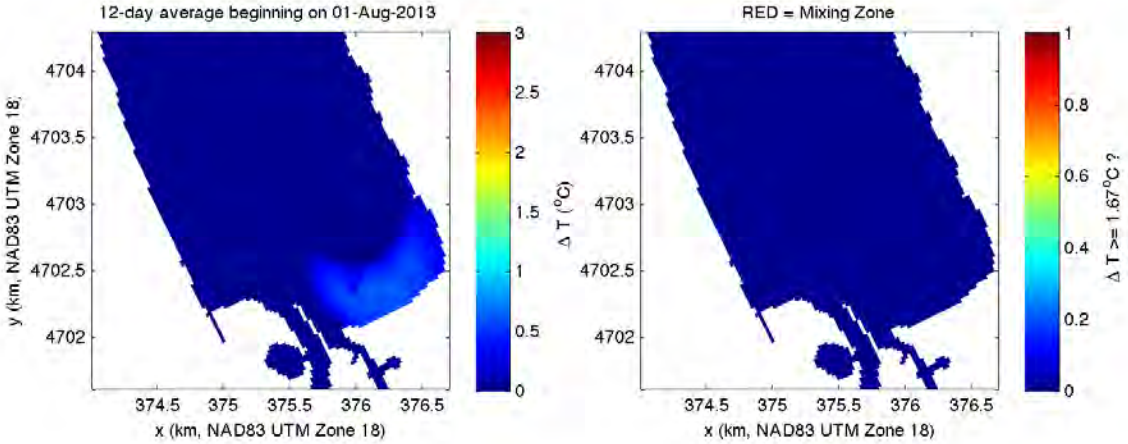

Figure A-66. Mixing zone plot based on water surface temperature for the high flow/high wind case.

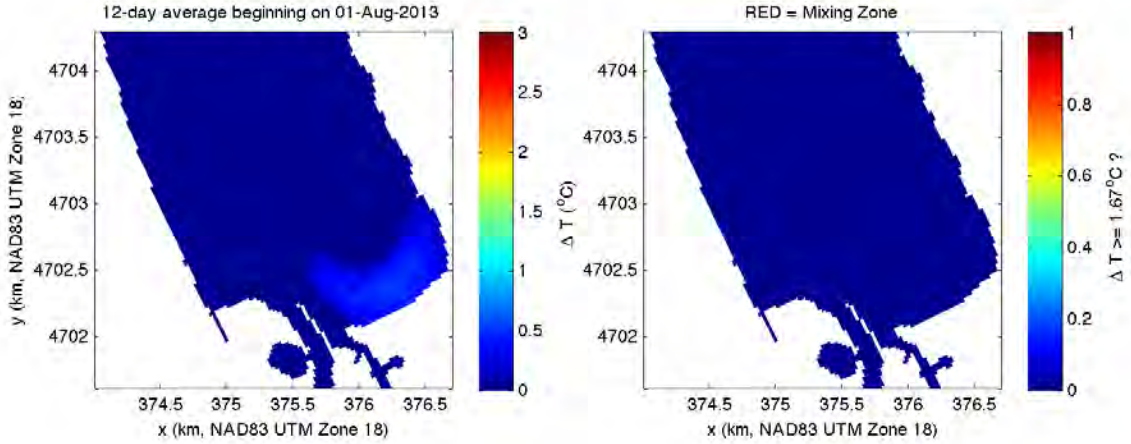

Figure A-67. Mixing zone plot based on water surface temperature for the low flow/high wind case.

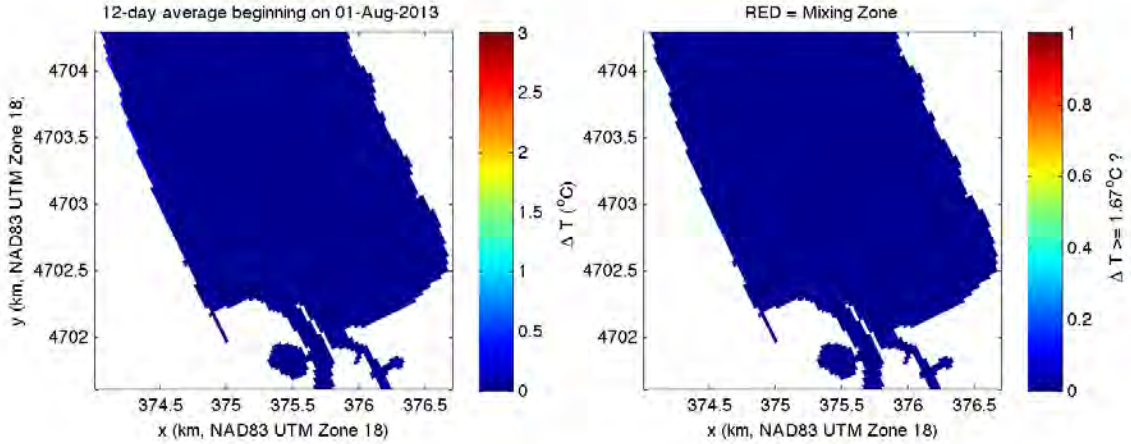

Figure A-68. Mixing zone plot based on water surface temperature for the low flow/low wind case.

A.5 References

Acosta, M.; Anguita, M.; Fernández-Baldomero, F. J.; Ramón, C. L.; Schladow, S. G.; and Rueda, F. J. (2015). Evaluation of a nested-grid implementation for 3D finite-difference semi-implicit hydrodynamic models. *Environmental Modelling & Software*, 64, 241-262.

Akar, P.J.; Jirka, G. H. (1991). *CORMIXII: An expert system for hydrodynamic mixing zone analysis of conventional and toxic multiport diffuser discharges*. Technical report, United States Environmental

Protection Agency, EPA/600/3-91/073.

Amorocho, J., and J. J. DeVries. "A new evaluation of the wind stress coefficient over water surfaces." *Journal of Geophysical Research: Oceans.* 85.C1 (1980): 433-442.

Chapra, Steven C. *Surface water-quality modeling*. Waveland press, 2008.

Doneker, R.L.; Jirka, G.H. (1990). *Expert system for hydrodynamic mixing zone analysis of conventional and toxic submerged single port discharges (CORMIX I)*. Technical report, United States Environmental Protection Agency. EPA/600/3-90/012.

Gelda, R. K., King, A. T., Effler, S. W., Schweitzer, S. A., & Cowen, E. A. (2015). "Testing and application of a two-dimensional hydrothermal/transport model for a long, deep, and narrow lake with moderate Burger number". *Inland Waters*, 5(4), 387-402.

Gill, A.E. (1982). *Atmosphere-Ocean Dynamics*. San Diego: Academic.

Haith, D.A.; Hollingshead, N.; Bell, M.L.; Kreszewski, S.W.; Morey, S.J. (2012). "Nutrient loads to Cayuga Lake, New York: Watershed modeling on a budget". *J. Water Res. Plann. and Manage.*, 138, 571-580.

Hilton, A.B.C.; McGillivary, D.L.; Adams, E.E. (1998). "Residence time of freshwater in Boston's inner harbor". *J. Water Port Coast. Ocean Eng.*, 124, 82-89.

Kantha, L.H.; Clayson, C.A. (1994). "An improved mixed layer model for geophysical applications". *J Geophys Res*, 99 (C12), 25235-25266, doi:10.1029/94JC02257.

Lee, J. H., & Jirka, G. H. (1980). Multiport diffuser as line source of momentum in shallow water. *Water Resources Research*, *16*(4), 695-708.

Martin JL, McCutcheon SC. 1999. *Hydrodynamics and transport for water quality modeling*. Boca Raton, FL: Lewis Publishers. -794 p.

Monsen, N.E.; Cloern, J.E.; Lucas, L.V.; Monismith, S.G. (2002). "A comment on the use of flushing time, residence time, and age as transport time scales". *Limnol Oceanogr,* 47, 1545-1553.

Rueda, F.J. (2001). "A three-dimensional hydrodynamic and transport model for lake environments." Ph.D. Dissertation, University of California, Davis.

Rueda, F. J., and Cowen, E. A. (2005). "Residence time of a freshwater embayment connected to a large lake." *Limnology and oceanography*, *50*(5), 1638-1653.

Rueda, F. J., Schladow, S. G., & Clark, J. F. (2008). "Mechanisms of contaminant transport in a multi-basin lake." *Ecological Applications*, *18*(sp8).

Schweitzer, S. (2015). "Physical Processes in a Long Narrow Deep Lake." Doctoral dissertation, Cornell University. Ithaca, NY.

Singleton, V.L.; Rueda, F.J.; Little, J.C. (2010). "A coupled bubble plume-reservoir model for hypolimnetic

oxygenation." *Water Resour Res*, 46(W12538), doi:10.1029/2009WR009012.

Smith, P. E. (1997). "A three-dimensional, finite-difference model for estuarine circulation." Ph.D. Dissertation, University of California, Davis.

Vandebroek, E. (2011). "Development of boundary conditions and bathymetry data for modeling transport processes in the southern end of Cayuga Lake." M.Eng. Report, Cornell University.